Multifunctional Nanocarriers for Combination Cancer Therapy

by

Jieni Xu

B.S. in Pharmacy, Shenyang Pharmaceutical University, 2013

M.S. in Pharmaceutical Sciences, University of Pittsburgh, 2015

Submitted to the Graduate Faculty of

School of Pharmacy in partial fulfillment

of the requirements for the degree of

Doctor of Philosophy

University of Pittsburgh

2019

UNIVERSITY OF PITTSBURGH

SCHOOL OF PHARMACY

This thesis/dissertation was presented

by

Jieni Xu

It was defended on

February 21, 2019

and approved by

Lisa Rohan, Ph.D., Professor,
Department of Pharmaceutical Sciences, School of Pharmacy, University of Pittsburgh

Da Yang, M.D., Ph.D., Assistant Professor,
Department of Pharmaceutical Sciences, School of Pharmacy, University of Pittsburgh

Christian Fernandez, Ph.D., Assistant Professor
Department of Pharmaceutical Sciences, School of Pharmacy, University of Pittsburgh

Binfeng Lu, Ph.D., Associate Professor
Department of Immunology, School of Medicine, University of Pittsburgh

Dissertation Director: **Song Li**, M.D., Ph.D.
Department of Pharmaceutical Sciences, School of Pharmacy, University of Pittsburgh

Multifunctional Nanocarriers for Combination Cancer Therapy

Jieni Xu, Ph.D.

University of Pittsburgh, 2019

Combination therapy of multiple drugs with different mechanisms can overcome drug resistance, improve safety and efficacy, and thus becomes a promising strategy in cancer treatment. However, the difference of physiochemical and pharmacokinetic properties of the combined drugs might lead to suboptimal uptake and biodistribution of two drugs at the tumor sites. Multifunctional nanocarriers merge as an ideal strategy to circumvent these limitations and improve the therapeutic effect of anticancer agents.

A dual-functional nanocarrier was first developed based on the PEG-conjugated S-trans, trans-farnesylthiosalicylic acid (FTS) for delivery of paclitaxel (PTX). FTS is a potent nontoxic RAS antagonist. To facilitate the release of FTS from the carrier and improve the drug loading capacity and formulation stability, both disulfide linkage and Fluorenylmethyloxycarbonyl (Fmoc) group were incorporated to PEG_{5k}-FTS_2 to form a PEG_{5k}-Fmoc-S-S-FTS_2 micellar system. PTX-loaded PEG_{5k}-Fmoc-S-S-FTS_2 micelles exhibited a superior synergistic therapeutic effect *in vitro* and *in vivo*.

Despite the potent therapeutic effect, the drug content from PEG-conjugated prodrug nanocarriers is relatively low. In order to solve this problem, drug-based monomer was polymerized to increase the number of drug units in each polymer molecule. Here a PPMP-based prodrug copolymer micelle ($POEG_{15}$-*b*-$PPPMP_7$), in which each carrier molecule contains 7 units of PPMP, was developed. PPMP is a potent inhibitor of glucosylceramide synthase (GCS), the major catabolic enzyme of ceramide. Doxorubicin (DOX)/POEG-*b*-PPPMP micellar system exhibited significantly improved antitumor response *in vitro* and *in vivo*.

The polymeric prodrug-based carrier strategy was also applied to another drug, suberoylanilide hydroxamic acid (SAHA), and developed a well-characterized $POEG_{15}$-*b*-$PSAHA_{12}$ nanocarrier. SAHA is a histone deacetylase inhibitor (HDACI) approved by FDA. *In vivo* delivery of DOX via POEG-*b*-PSAHA led to significant inhibition of 4T1.2 tumor growth.

However, not all targets have small molecule drugs. Better synergism would be achieved through the combination of small molecule drugs (for known targets) and gene therapeutics for "undruggable" targets. This inspired us to develop a creatine-based polymer (POEG-PCre) for the co-delivery of nucleic acids and chemodrugs. POEG-PCre carrier is effective in co-delivery of DOX and bioengineered miR-34a to tumor cells and specific accumulation to lung tissue for the treatment of breast cancer lung metastasis.

Table of Contents

List of Tables

List of Figures

Preface

This Ph.D. dissertation is a summary of my research work accomplished in the Center for Pharmacogenetics, Department of Pharmaceutical Sciences, University of Pittsburgh under the dedicated supervision and kind guidance of my advisor Dr. Song Li. I express my sincere appreciation to those who have contributed to this thesis and supported me during this amazing journey for without any of them, this research work would not have been possible.

First and foremost, I would like to express my sincerest thanks to my advisor Dr. Song Li, who provided me such a precious opportunity to start and complete my PhD training with him. He sets an example of excellence as a researcher, mentor, instructor, and role model. It was a real privilege and honor for me to share of his exceptional scientific knowledge but also of his extraordinary human qualities. I appreciate his contributions of time and ideas to make my work productive and interesting. His valuable suggestions, comments and guidance encourage me to explore deeper in knowledge and keep the curiosity to the new things, from which I learned how to be a real scientist. I am also indebted towards him for his generosity, selfless support and patience that he has provided to me for the last six years.

I would like to extend my gratitude to my thesis committee members Dr. Lisa Rohan, Dr. Da Yang, Dr. Christian Fernandez, Dr. Binfeng Lu for all of their suggestions and encouragement through this process. Their invaluable discussion, ideas, and feedback helped me step out from my comfortable zone and think problems from different aspects.

I would also like to thank my ‘greater Li family’: Thank Dr. Jiang Li for teaching me the first ever cell culture experiment and continuous sharing of his broad knowledge, rich experience and insightful suggestions. Thank Dr. Jingjing Sun for her help in polymer synthesis as well as

the precious collaborative opportunities she provided. Thank Dr. Weina Ma for letting me know "what you sow is more important than what you reap". Thank Yuan Wei, Zhangyi Luo and Dr. Dingwei Diao for bringing me joy and laugh during the tough journey of graduate study. Many thanks to my other dear lab members (Dr. Yifeizhang, Dr. Jianqin Lu, Dr. Peng Zhang, Dr. Mohammed Ghazwani, Dr. Xiaolan Zhang, Dr. Yichao Chen, Zhuoya Wan, Pearl Moharil, Haozhe Huang, Ziqian Zhang, Yuang Chen, Dr. Yanhua Liu, Dr. Lei Liang, Dr. Qiongfeng Liao, Dr. Min Zhao, Dr. Yan He, Dr. Yihui Deng, Dr. Yuqian Du, Dr. Yangwuyue Liu, Zuojun Li, Qianyu Zhai, Shengzhen Liu), who inspired and helped me in every step forward.

Many thanks for all of faculties and members in Center for Pharmacogenetics. Special thanks to Dr. Wen Xie, Dr. Xiaochao Ma, Dr. Da Yang and Dr. Christian Fernandez who create such a great environment for us to study and research. Many thanks go to the faculties from School of Pharmacy at the University of Pittsburgh. Special thanks to Dean. Patricia Dowley Kroboth, Dr. Randall B. Smith, Dr. Samuel M. Poloyac, Dr. Barry Gold, Dr. Robert B Gibbs, Dr. Sean Xie, Dr. Maggie Folan, Lori M. Altenbaugh for their support and help all these years.

I would especially like to thank my amazing family for the love, support, and constant encouragement I have gotten over the years. In particular, I would like to thank my parents, Yan Xu and Anyun Xie, who generated my love and mission to pharmaceutical sciences by growing me up in a family where all family members are devoted themselves to pharmaceutical research and are proud of what they are doing. They provided me the freedom and courage to chase my dream. Finally, I would like to express my deep gratitude to my dear boyfriend, Dr. Cheng Fang, for his tolerance, support and love. He rebuilt my confidence to my graduate research and future life. We grow up together, figure way out together, and conquer every difficulty together.

1.0 Introduction

1.1 Combination Therapy for Cancer Treatment

Cancer is defined as a disease involving abnormal cell growth with the potential to invade or spread to other parts of the body. Cancer is among the leading causes of death worldwide (World Cancer Report 2019 from the World Health Organization). In 2018, an estimated 1.7 million new cases will be diagnosed and 0.6 million cancer-related deaths in United States. The economic and financial burden for cancer is increasing, with the $147.3 billion national expenditures for cancer care in United States in 2017 (date reported by National Cancer Institute). Age-standard cancer mortality rates for all types of malignancies have decreased, but newer drugs only contribute to a small percentage of this improvement[1]. This is primarily because the development of new pharmaceutical anti-cancer agents is laborious and expensive, requiring initial *in vitro* and *in vivo* experimentation, and subsequent clinical trials before receiving FDA approval[2]. It is estimated that a newly designed drug takes 15 years to enter the pharmaceutical market[3]. Consequently, it is important to find more efficient methodical approaches that are also economically feasible.

Owing to the intrinsic heterogeneity and complexity of tumor cells, they have tendency to spread beyond its original site and become resistant to certain drugs, and its genetic diversity– underscores the need for a variety of approaches to attack it[4]. Monotherapy based on a single drug has some limitations in cancer treatments, such as limited efficacies, poor tolerability and drug resistance[5]. Combination therapy of two or more drugs with different mechanisms can overcome these limitations, and thus becomes a cornerstone and standard clinical practice for

cancer therapy[6]. Combination therapy targets key pathways in a synergistic or an additive manner. This approach potentially reduces drug resistance, while simultaneously providing therapeutic anti-cancer benefits, such as reducing tumor growth and metastatic potential, arresting mitotically active cells, reducing cancer stem cell populations, and inducing apoptosis[2].

It is well known that the success of combination therapy is largely dependent on the choice of drugs. Recently, the focus of drug screening has shifted from traditional chemotherapeutic agents to molecular targeted therapeutics, including monoclonal antibodies and small molecule inhibitors[7, 8]. Different from traditional chemotherapy acting on all rapidly dividing cells, targeted therapy blocks the growth and spread of cancer through interfering with specific molecular targets involved in the tumor development and metastasis. The combination of targeted therapy and traditional chemotherapy drugs might represent a promising strategy against cancers. In this thesis, chemotherapy would be combined with several targeted therapies, including RAS inhibitor (FTS), GCS inhibitor (PPMP), HDAC inhibitor (SAHA) and miRNA-34a. The rational of each combinational regimen will be discussed in the background information of each chapter.

1.2 Nanoparticles for Combination Therapy in Combating Cancer

1.2.1 Nanomedicine in Cancer Therapy

Since the last century, tremendous efforts have been made to circumvent the limitations of anticancer drugs and maximize its clinical outcomes in cancer treatment. Among them,

nanomedicine has gained popularity as an attractive strategy to improve physiochemical/pharmacokinetic properties, enhance therapeutic efficacy, and reduce the systemic toxicity of a broad variety of anticancer agents[9]. A number of nanocarriers, such as polymeric conjugates, liposomes, micelles, dendrimers, nanocrystals, and many others, have been developed, and some of them have already been successfully put into market or are under clinic trials[10, 11].

The advantages of nanomedicine over the administration of free anticancer agents include enhanced water solubility of hydrophobic agents, increased absorption and bioavailability, protection from degradation by the degrading enzymes before reaching the target area, and prolonged blood circulation allowing increased accumulation in the tumor site. It has been well-established that newly formed vasculatures at a tumor site are usually leaky and abnormal in architecture. At the same time, lymphatic drainage is usually ineffectively developed in solid tumor. Therefore, nanoparticles with a size of 20~200 nm, given adequate circulating time, preferentially extravasate into solid tumor tissues, and are retained in tumor at a higher concentration over normal tissues. This phenomenon, first discovered by Maeda and Matsumura[12], is well known as the enhanced permeability and retention effect (EPR effect) and is the physiological basis of the preferential accumulation of nanoparticles in the tumor site or "passive targeting." In addition to passive targeting, the efficiency of selective delivery can be further enhanced by attaching a targeting ligand, such as an antibody, small peptide, aptamer, or others, onto the surface of nanoparticles. Based on the high affinity between ligands and receptors highly expressed on target cells, this "active targeting" strategy further enhances recognition and uptake of drug-loaded particles by cancer cells[13, 14].

1.2.2 Nanoparticles for Combination Therapy

Nanoparticles have recently emerged as a promising class of carriers for the co-delivery of multiple drugs. Nanoparticle formulations offer several advantages for multidrug delivery compared with administration of free drugs. The low solubility and different pharmacokinetic properties of combined drugs will lead to poor uptake and suboptimal dose ratio of the two drugs at the tumor sites[15]. Besides, direct use of these drugs via systemic administration might result in poor biodistribution and severe systemic toxicities. On the contrary, packing multiple drugs into single nanocarriers will enable controlled release of multiple drugs in precisely balanced ratios, which can normalize the pharmacokinetics, biodistribution, and stability of chemically dissimilar drugs that independently have disparate pharmacological behaviors[16]. In addition, stimulus-responsive, targeted carriers in development can co-release drugs in the same organ, tissue, or cell, to increase efficacy and to reduce toxicity from off-target exposure.

1.2.3 Polymeric Micelles as an Attractive Approach for Cancer Therapy

Among a variety of nanocarriers developed in recent decades, micelles are unique and appealing due to their high capability to solubilize hydrophobic agents and ease of manipulation. More importantly, the small size of micelles, typically below 100 nm, allows for preferential accumulation in solid tumor through passive targeting. Micellar systems are usually formed by amphipathic molecules, or surfactants, composed of two distinct domains, one being hydrophilic and the other hydrophobic. Upon exposure to an aqueous environment, the hydrophobic segments are self-assembled into a hydrophobic inner core, surrounded by a corona formed by

hydrated hydrophilic domains. This unique core-shell architecture of micelles provides both a hydrophobic loading zone for the encapsulation of hydrophobic drugs as well as a hydrophilic outer layer to effectively diminish the binding of plasma proteins, nonspecific uptake by the reticuloendothelial system (RES), and unwanted self-aggregation with other micelles[17, 18]. A minimum concentration of micelle-forming surfactants is required for micelle formation in an aqueous medium, which is called the critical micelle concentration (CMC). Micelle-forming amphipathic molecules remain as monomers in solution when below the CMC; while above the CMC, they are self-assembled into micelles. The CMC is an important parameter of the stability of micelles upon dilution. Generally, larger hydrophobic segments lead to a lower CMC value.

For most of the current micellar systems, drug-loading largely relies on hydrophobic interactions between their core-forming hydrophobic segments and the poorly water-soluble drugs. Commonly used hydrophobic segments include hydrophobic copolymers, lipids, or other small hydrophobic molecules. Polyester and polyamide are two widely used copolymers in micelle formulation, such as poly(lactic acid) (PLA), poly(lactic-co-glycolic acid) (PLGA), and poly(L-lysine) (PLL)[19-21]. These materials are able to be gradually degraded *in vivo* through enzyme-assisted hydrolysis of ester or amide bond, and finally excreted out of the body without causing toxicity. Besides copolymers, lipids are also used as hydrophobic segments in micelle formation. Torchilin's group has developed a lipid-core micellar system using PEG-phosphatidylethanolamine (PE) conjugate as surfactant[22-24]. In these systems, a strong hydrophobic interaction provided by double acyl chains of PE facilitated the formation of stable micelles and encapsulation of a broad spectrum of anticancer agents including paclitaxel (PTX), tamoxifen, and camptothecin (CPT)[25, 26]. As for cases of using small molecules as hydrophobic segments of surfactants, the PEG-dendritic oligo-cholic acid system would be an

excellent example. This so-called amphiphilic telodendrimer system was first developed by Lam's group[27]. In their studies, multiple cholic acids (CA), one of the major bile acids produced in the human liver, were conjugated to the terminal of the PEG chain to construct a biocompatible copolymer with linear-dendritic architecture. Distinct from other hydrophobic molecules, CA has unique facial amphiphilicity, making it an efficient functional building block for caging other hydrophobic molecules[28, 29]. Combined with its small particle size (20~60 nm) and superior stability, this micellar system acts as a promising delivery vector for PTX with specific tumor accumulation, low toxicity profiles, and excellent therapeutic efficacy in a nude mice model with human ovarian cancer xenograft[30-32].

Poly(ethylene glycol) (PEG) is the most commonly utilized hydrophilic segment to construct micelle-forming surfactants. The advantages of PEG in pharmaceutical applications include high water solubility, neutral charge, low polydispersity index, nontoxicity, low immunogenicity, commercial availability, high solubility in most organic solvents, and ease to conjugate with other segments[33]. It has been demonstrated that PEGylation effectively stabilizes micellar systems, diminishes undesired binding with blood components, and prolongs circulation time. Besides micelles, PEG is also widely applied to other delivery systems as liposomes, polymer drug conjugates, and PEGylated proteins/peptides[34, 35].

1.3 Prodrug-based Dual-functional Nanocarriers for Combination Therapy

As discussed above, micelles are usually formed by amphipathic molecules composed of both a hydrophilic segment, usually PEG, and one or more hydrophobic segments. These hydrophobic segments can be hydrophobic copolymers, lipids, or small molecules. Despite the

high efficiency in encapsulation of hydrophobic agents, most of the segments are "inert" molecules that lack therapeutic effect and potentially impose safety issues[36]. To overcome these important obstacles, we developed prodrug-based dual-functional nanocarriers, in which the carrier itself is a prodrug exhibits favorable biological activity, at the same time, it could serve as the carrier for other hydrophobic anticancer drugs. In our case, the hydrophobic small molecule drugs were covalently linked to PEG chain to construct prodrug. This strategy improves water solubility, prolonged circulation time, improved pharmacokinetic profile, preferential accumulation based on passive targeting or active targeting and reduces adverse effects. More interestingly, besides being an effective strategy to improve the performance of hydrophobic anticancer agents, the prodrug polymer may also be developed as a potential nanocarrier for encapsulation of other chemotherapeutic agents. This dual-function nanocarrier not only acts as an efficient delivery system for anticancer agents, but also exhibits anticancer activity by itself and, more importantly, synergizes with loaded agents for improved therapeutic efficacy and/or reduced side effects.

1.3.1 PEG-conjugated Prodrug-based Carriers

One strategy to develop prodrug polymer is conjugating selected numbers of hydrophobic anticancer drugs to PEG. In our lab, several PEG-conjugated prodrug-based carriers have been developed, such as PEG-vitamin E, PEG-Embelin and PEG-FTS[37-39]. FTS is a potent and nontoxic RAS antagonist, leading to RAS dependent tumor regression[40]. Based on its hydrophobic nature and a free carboxyl group in its structure, FTS can be easily conjugated to a PEG to construct a micelle-forming amphipathic molecule. We first developed a PEG-FTS conjugate that consists of a molecule of PEG and two molecules of FTS (PEG_{5K}-FTS_2). PEG_{5K}-

FTS_2 conjugates dramatically increased the water solubility of FTS, and self-assembled to nano-sized (20~30nm) spherical micelles that effectively solubilized other hydrophobic agents as PTX[39]. Besides PTX, PEG_{5K}-FTS_2 also demonstrated synergistic action with other anticancer agents in tumor growth inhibition, such as DOX or curcumin[41]. For further optimization of PEG-FTS systems, four different PEG-FTS conjugates were developed and characterized. They differed in the molecular weight of PEG (PEG_{2K} vs PEG_{5K}) and the number of FTS molecules (FTS_2 vs FTS_4). The data demonstrated that PEG-FTS conjugates equipped with four FTS molecules formed more stable micelles with PTX compared to those with two FTS, and that PTX-loaded micelles formed by PEG_{5K} exhibited improved stability over counterparts with PEG_{2K}. It is likely that more FTS motifs formed an increased hydrophobic space for accommodation of PTX, and a longer chain of PEG more efficiently stabilized these drug-loaded nanoparticles. Consistent with these data, PTX/PEG_{5K}-FTS_4 micelles showed the slowest kinetics of PTX release and were the most potent in inhibiting the tumor cell growth *in vitro* and *in vivo*[42].

1.3.2 Polymeric Prodrug-based Carriers

Despite the potent therapeutic effect, the PEG-conjugated prodrug-based carriers showed relatively low drug content in each carrier molecule (PEG_{5K}-FTS_2 or PEG_{5K}-FTS_4), therefore the amounts of drug that can be delivered to tumor tissues are limited, which confines the contribution of carrier-associated biological activity to the over-all activity of drug-loaded micelles[43]. In addition, recent studies reported that the hydrophobic cores were essential to improve the drug loading capacity, formulation stability and slower the drug release[44-46]. These inspired us to explore new prodrug micellar systems with increased units of drug per

prodrug molecule and larger hydrophobic core. Generally, the post-modification method was the most widely applied approach, by which drugs was chemically attached to a polymer backbone to construct prodrug micelles[47, 48]. However, this method often involves additional steps which complicated the synthetic process. In addition, due to the steric hindrance, some reactive groups might remain in the polymers following conjugation, which might cause the destruction of micelle structure or side effects through reacting with bioactive molecules *in vivo*[49]. Recently, polymerization of drug-based monomer has been developed as a facile strategy to obtain well-defined prodrug amphiphilic polymers[50, 51].

We applied this strategy of the polymerization of drug-based monomer to other two targeted drugs: PPMP (a GCS inhibitor) and SAHA (a HDAC inhibitor). The drug-based monomer with olefin was easily synthesized by conjugating the drug with methacryloyl chloride or vinyl benzyl chloride to form a hydrolysable ester linkage. Meanwhile, the macro-chain transfer agent POEG was then synthesized by reversible addition-fragmentation transfer (RAFT) polymerization of hydrophilic OEGMA monomer, which was further used to initiate the polymerization of hydrophobic drug-based monomer and give a well-defined diblock co-polymers with a hydrophilic POEG block and a hydrophobic drug block. These amphiphilic polymers could self-assemble into prodrug micelles and act as the nanocarrier for other hydrophobic anticancer drugs. The $POEG_{15}$-b-$PPPMP_7$ and $POEG_{15}$-b-$PSAHA_{12}$ prodrug polymers contain 7 units of PPMP and 12 units of SAHA respectively. The increased units of hydrophobic drugs in each prodrug polymer could not only decrease the amounts of carrier materials in *in vivo* application by increase the drug loading capacity and micelle stability, but also provide better synergistic effect with loaded anticancer drugs. The physiochemical properties of two polymeric prodrug-based micelles including size, structure, drug loading and

release were evaluated. Moreover, the antitumor activity of carrier alone and drug-loaded micelles were investigated *in vitro* and *in vivo*.

1.4 Multi-functional Nanocarriers for Co-delivery of Gene/drug Combination

Tremendous progress in sequencing thousands of cancer genomes through The Cancer Genome Atlas (TCGA) and advances in cancer biology have uncovered many drivers of tumorigenesis. Many of the drivers, particularly kinases, have provided druggable targets that have yielded significant clinical benefits over the past several decades. However, not all proteins are suitable for drug interactions and even fewer are appropriate drug targets, owing to large protein–protein interaction (PPI) interfaces or their lack of deep protein pockets. In this situation, gene therapy may play more important role in drugging the "undruggable" targets.

Gene therapy involves the delivery of plasmid DNA (pDNA), small interfering RNA (siRNA), short hairpin RNA (shRNA) or micro RNA (miRNA) to modulate the expression of specific gene or proteins, which has the potential advantages to target any disease related gene. Cancer gene therapy usually works through either upregulating tumor suppressor gene and cytotoxic immune cytokines or downregulating the oncogenes and genes involved in tumor cell drug resistance. The use of combination therapy involving both gene therapy and chemotherapy has resulted in combinational effect and has become an increasingly important strategy for the future.

However, the physiochemical properties of chemotherapeutic agents and nucleic acids are totally different: most anticancer drugs are small molecule with poor water solubility, while nucleic acids are polyanionic molecules with high molecular weight, high water solubility and

low stability. It is significantly challenging to develop a dependable system to co-deliver both therapeutics to the target organs, tissues and cells. Most carriers reported so far are designed for the separate delivery of small molecule drugs or nucleic acid therapeutics, which would have different pharmacokinetics and pharmacodynamics properties and can hardly achieve combinational effects[52, 53] Some carriers such as liposomes, polymeric nanoparticles and micelles were developed for codelivery of the two different types of therapeutics but they often involved complicated preparation process[54]. Herein, we report a novel nanocarrier (POEG-PCre) for co-delivery DOX and bioengineered miR-34a prodrug, based on the built-in blocks of naturally occurring cationic molecule—creatine. Stable and nanosized micelles co-loaded with DOX and tRNA-mir-34a could be simply prepared and were highly effective in targeted delivery of payloads to lungs. Significantly improved antitumor activity was demonstrated with codelivery of DOX and miR-34a prodrug in comparison with other control groups in a 4T1.2 lung metastasis model. POEG-PCre may represent a simple and effective delivery system for an optimal chemo-gene combination therapy.

2.0 An Improved PEG-FTS Conjugate as a Dual Functional Nanocarrier for Enhanced Delivery of Paclitaxel

2.1 Abstract

We have previously improved the bioactivity of PEG_{5k}-FTS_2 system by incorporating disulfide bond (PEG_{5k}-S-S-FTS_2) to facilitate the release of Farnesyl thiosalicylic acid (FTS)[55]. Later, Fluorenylmethyloxycarbonyl (Fmoc) moiety has been introduced to PEG_{5k}-FTS_2 system (PEG_{5k}-Fmoc-FTS_2) in order to enhance drug loading capacity (DLC) and formulation stability[56]. In this study, we have brought in both disulfide linkage and Fmoc group to PEG_{5k}-FTS_2 to form a simple PEG_{5k}-Fmoc-S-S-FTS_2 micellar system. PEG_{5k}-Fmoc-S-S-FTS_2 conjugate formed filamentous micelles with a ~ ten-fold decrease in critical micellar concentration (CMC). Compared with PEG_{5k}-Fmoc-FTS_2, our novel system exhibited further strengthened DLC and colloidal stability. More FTS was freed from PEG_{5k}-Fmoc-S-S-FTS_2 in treated tumor cells compared to PEG_{5k}-Fmoc-FTS_2, which was correlated to an increased cytotoxicity of our new carrier in these cancer cells. After loading Paclitaxel (PTX) into PEG_{5k}-Fmoc-S-S-FTS_2 micelles, it showed more potent efficiency in inhibition of tumor cell proliferation than Taxol® and PTX-loaded PEG_{5k}-Fmoc-FTS_2. PTX release kinetics of PTX/PEG_{5k}-Fmoc-S-S-FTS_2 was much slower than that of Taxol® and PTX/PEG_{5k}-Fmoc-FTS_2 in normal release medium. In contrast, in glutathione (GSH)-containing medium, PTX in PEG_{5k}-Fmoc-S-S-FTS_2 micelles revealed faster and more complete release. Pharmacokinetics and tissue distribution study showed that our PEG_{5k}-Fmoc-S-S-FTS_2 system maintained PTX in circulation for a longer time and delivered more PTX to tumor sites with less accumulation in major organs.

Finally, PTX-loaded PEG_{5k}-Fmoc-S-S-FTS_2 micelles resulted in a superior therapeutic effect in vivo compared to Taxol® and PTX formulated in PEG_{5k}-Fmoc-FTS_2 micelles.

2.2 Background

Micelles are a promising delivery system for anticancer drugs due to their ability to solubilize hydrophobic drugs[57], small size[58], prolonged retention in the blood[59], enhanced tumor penetration[60] and ease in preparation[61]. Among all micellar systems, PEG-derivatized micellar systems impede the recognition and binding of plasma proteins, further preventing reticuloendothelial system (RES) surveillance and rapid elimination of nanoparticles[34, 62, 63]. Biologically active carrier, in which small molecules with therapeutic effect are conjugated with PEG, is an attractive and unique strategy since these bioactive molecules could achieve the additive or synergistic effect with co-delivered anticancer drugs[64-66]. Our group previously developed PEG_{5k}-FTS_2 to load Paclitaxel (PTX), which exhibited enhanced antitumor efficiency compared to Taxol® formulation in vitro and in vivo[39]. FTS is a farnesyl mimic and an antagonist of RAS protein[67]. Mutations of the K-Ras gene occur in over 90% of pancreatic carcinomas and 20 to 25% of all human tumors[68, 69]. FTS competes with active RAS for binding to the docking protein on the cell membrane, leading to RAS dislodgement from the cell membrane and degradation[70]. FTS has shown promising results in clinical trials for several types of cancers, including phase I studies in refractory hematologic malignancies and elapsed/refractory solid tumors as well as phase II studies in pancreatic cancer and KRAS mutant lung adenocarcinoma. The results of most clinical trials showed that FTS was well tolerated and

showed insufficient or modest activity in those patients as a single therapy, and therefore suggested FTS to be utilized in combination therapy[71-74].

To facilitate the effective release of FTS from the carrier, PEG_{5K}-S-S-FTS_2 was then developed in our group[55]. Disulfide bond could be readily reduced by the glutathione[75, 76]. It has been reported that the GSH concentration in tumor tissue was four times higher than that in normal tissue[77]. In addition, the intra-cellular concentration of GSH (2-10 mM) is a thousand-fold higher than that in blood or extra-cellular matrix (2-20 μM)[78, 79]. Hence, PEG_{5K}-S-S-FTS_2 micelles possess a unique advantage that they are stable in the circulation but rapidly release FTS and loaded PTX upon reaching the tumor tissue/cells. Our data showed that the incorporation of a disulfide bond into PEG_{5k}-FTS_2 resulted in an improved FTS release in cultured tumor cells, and enhanced inhibition of the proliferation of these tumor cells. More importantly, PTX-loaded PEG_{5K}-S-S-FTS_2 formulation revealed a significantly enhanced inhibition of tumor growth than the PEG_{5k}-FTS_2 formulation in a murine breast cancer model (4T1.2)[55].

Another independent strategy to improve the formulation stability and loading capacity of PEG_{5k}-FTS_2 micelles was to incorporate a 9-fluorenylmethoxycarbony (Fmoc) moiety at the interfacial region between hydrophilic PEG segment and hydrophobic FTS domain[56]. The Fmoc carbamate, with an aromatic ring, is often used as an amine protecting group in peptide synthesis[80]. By including Fmoc moiety in PEG_{5k}-FTS_2 conjugate, we provided an additional mechanism of drug/carrier interaction (π-π stacking interaction) besides hydrophobic interaction between hydrophobic FTS and loaded hydrophobic anticancer drugs[81, 82]. The enhancement

of drug/carrier interaction shall enable the carrier more effective in loading more drugs (higher drug loading capacity) and in stabilizing loaded drugs in circulation (excellent colloidal stability)[83]. Indeed, DOX loaded in PEG_{5k}-Fmoc-FTS_2 showed sustained release kinetics, which was slower than that of PEG_{5k}-FTS_2 formulation. In addition, pharmacokinetics and biodistribution study exhibited prolonged circulation of DOX/PEG_{5k}-Fmoc-FTS_2 in the blood and enhanced DOX accumulation at tumor sites. More importantly, PTX or DOX formulated in PEG_{5k}-Fmoc-FTS_2 led to significantly improved antitumor activities over those drugs formulated in PEG_{5k}-FTS_2 in a breast cancer or prostate cancer model[56].

In this study, we incorporated both disulfide and Fmoc into PEG_{5k}-FTS_2 system to gather the merits from both of them but overcome the demerits from each of them. Our data showed that PEG_{5k}-Fmoc-S-S-FTS_2 exhibited a further decrease of CMC and an improvement in both drug loading capacity and formulation stability compared to PEG_{5k}-Fmoc-FTS_2. PEG_{5k}-Fmoc-S-S-FTS_2 was more effective in FTS release inside tumor cells than PEG_{5k}-Fmoc-FTS_2, which likely contributed to the increased cytotoxicity of the new carrier. Pharmacokinetics and biodistribution study showed that PTX/PEG_{5k}-Fmoc-S-S-FTS_2 was stable in the blood and was more effective than PTX/PEG_{5k}-Fmoc-FTS_2 in mediating selective delivery of PTX to tumor tissues. More importantly, PTX/PEG_{5k}-Fmoc-S-S-FTS_2 was significantly more effective than PTX/PEG_{5k}-Fmoc-FTS_2 and Taxol® in antitumor activity in a murine breast cancer model.

2.3 Experiment Procedures

2.3.1 Materials

(S)-2,6-Bis-tertbutoxybonylaminohexanoic acid (Boc-lys(Boc)-OH) and N^2-(((9*H*-fluoren-9-yl)methoxy)carbonyl)-N^6-(*tert*-butoxycarbonyl)-*L*-lysine (Fmoc-lysine(Boc)-OH) were purchased from GL Biochem (Shanghai, China). Poly (ethylene glycol) methyl ether (MeO−PEG−OH, MW = 5000kDa), dimethyl sulfoxide (DMSO), 3-(4,5-dimethylthiazol-2-yl)-2,5- diphenyl tetrazolium bromide (MTT), and Dulbecco's Modified Eagle's Medium (DMEM) were all purchased from Sigma-Aldrich (St. Louis, MO). Fetal bovine serum (FBS) and penicillin−streptomycin solution were purchased from Thermo Fisher Scientific (Waltham, MA). Dicyclohexylcarbodiimide (DCC) was purchased from Alfa Aesar (Ward Hill, MA). 4-(dimethylamino) pyridine (DMAP) was purchased from Calbiochem-Novabiochem Corporation (San Diego, CA). Paclitaxel (98%) was purchased from AK Scientific Inc. (Union City, CA). All solvents used in this study were of HPLC grade.

2.3.2 Synthesis of PEG_{5k}-Fmoc-S-S-FTS_2 Conjugate

PEG_{5k}-Fmoc-S-S-FTS_2 conjugates were synthesized via solution phase condensation reaction as shown in Figure 2-1.

Compound 1: MeO-PEG_{5k}-OH (5g, 1.0 mmol, 1.0 eq), Fmoc-Lys (Boc)-OH (1.2g, 2.5 mmol, 2.5 eq), DCC (515 mg, 2.5 mmol, 2.5 eq) and DMAP (37mg, 0.3 mmol, 0.3 eq) were dissolved in DCM and stirred at room temperature for two days. The mixture was filtered

through cotton and then purified through two cycles of dissolution/precipitation with DCM/ether and DCM/ethanol respectively to afford Compound **1** (4.5 g, 0.82 mmol, 82% yield).

Compound 2: Compound **1** (MeO-PEG_{5k}-Fmoc-lysine-Boc) (4.5g, 0.8 mmol) was dissolved in 20 mL mixture of trifluoroacetic acid (TFA)/DCM (1:1, v/v). The mixture was stirred for 2 hours at room temperature and purified through two cycles of dissolution/precipitation with DCM/ether to give Compound **2** (4.0 g, 0.75 mmol, 91% yield).

Compound 3: Compound **2** (MeO-PEG_{5k}-Fmoc-lysine) (4.0 g, 0.8 mmol), Boc-Lys (Boc)-OH (692 mg, 2.0 mmol, 2.5 eq), DCC (412 mg, 2.0 mmol, 2.5 eq) and DMAP (29 mg, 0.24 mmol, 0.3 eq) were dissolved in DCM and stirred at room temperature for two days. The mixture was filtered through cotton and then purified through two cycles of dissolution/precipitation with DCM/ether and DCM/ethanol respectively to afford Compound **3** (4.5 g, 0.79 mmol, 84% yield).

Compound 4: Compound **3** (MeO-PEG_{5k}-Fmoc-lysine-lysine-diBoc) was dissolved in 20 mL mixture of trifluoroacetic acid (TFA)/DCM (1:1, v/v). The mixture was stirred for 2 hours at room temperature and purified through similar steps as described above to afford Compound **4** (3.8g, 0.69 mmol, 87% yield).

Compound 5: Compound **5** was synthesized following a published method.[39]

Compound 6: Compound **5** (FTS) (3.6 g, 10 mmol), Bis(2-hydroxyethyl) disulfide (1.5 g, 10 mmol, 1.0 eq), DCC (3.1 g, 15 mmol, 1.5 eq) and DMAP (122 mg, 1 mmol, 0.1 eq) were dissolved in DCM and stirred at room temperature until TLC showed completion of the reaction. The mixture was filtered through cotton and the filtrate was concentrated on a rotary evaporator. The residue was chromatographed (1:4 EtOAC/PE) on silica gel to afford Compound **6** (3.2 g, 6.5 mmol, 65% yield).

Compound 7: Compound **6** (FTS-S-S-OH) (3.2 g, 6.5 mmol), succinic anhydride (1.3 g, 13.0 mmol) and DMAP (1.6 g, 13.0 mmol) was dissolved in DCM and refluxed at 50 °C until TLC showed completion of the reaction. The mixture was concentrated on a rotary evaporator and the residue was chromatographed (1:1 EtOAc/PE) on silica gel to afford the Compound **7** (5.8 g, 6.5 mmol, 97% yield).

Compound 8: Compound **4**, Compound **7**, DCC and DMAP were dissolved in DCM with a molar ratio of 1:6:6:0.3 and stirred at room temperature for two days. The mixture was filtered through cotton and then purified through two cycles of dissolution/precipitation with DCM/ether and DCM/ethanol respectively to afford Compound **8** (3.90g, 0.59 mmol, 85% yield).

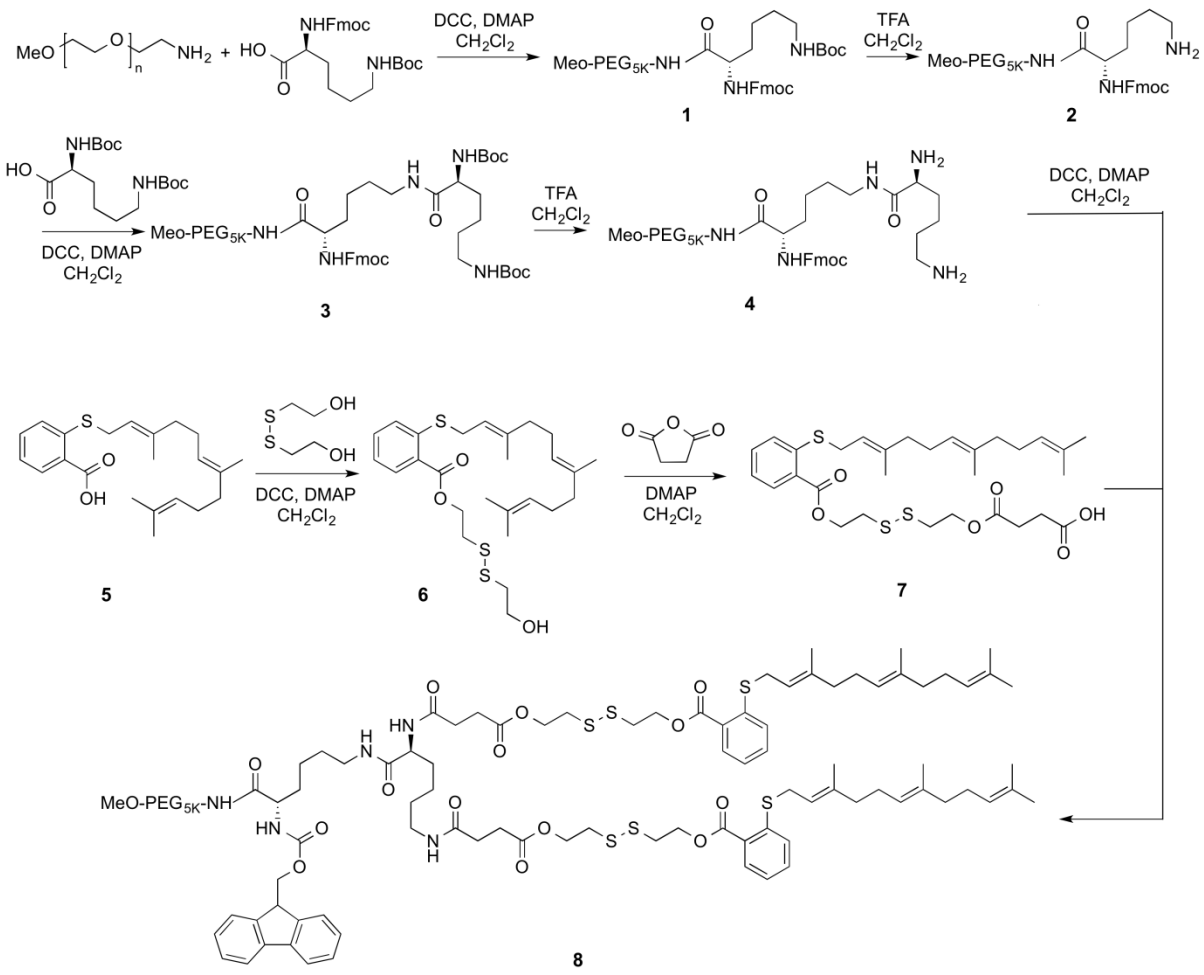

Figure 2-1. Synthesis of PEG_{5K}-Fmoc-S-S-FTS_2 conjugate

2.3.3 Preparation and Characterization of PTX-Loaded PEG_{5k}-Fmoc-S-S-FTS_2 Micelles

PTX (10 mM in chloroform) was mixed with PEG_{5k}-Fmoc-S-S-FTS_2 (10 mM in chloroform) at various carrier/drug molar ratios. The chloroform was removed by nitrogen flow to produce a thin film of drug/carrier, which was further dried under high vacuum for 2 h to remove any trace of remaining solvent. Then, the thin film was hydrated and vortexed in saline to form PTX-loaded micelles. The PTX-free micelles were prepared similarly as described above.

The particle size and the size distribution of micelles were examined via a Zetasizer (DLS). The morphology of drug-free or PTX-loaded PEG_{5k}-Fmoc-S-S-FTS_2 was observed using transmission electron microscopy (TEM). The drug loading efficiency was examined by high-performance liquid chromatography (HPLC) as described in a previous publication[65]. DLC and drug loading efficiency (DLE) were calculated according to the following equation[65]: DLC %= [weight of drug loaded/(weight of carrier used + weight of drug used)]×100%, DLE %= (weight of loaded drug/weight of input drug)×100 %. The colloidal stability of drug-loaded micelles with various carrier/drug molar ratios was evaluated by following the changes in sizes of the particles or visible precipitates every hour in the first 12 h and daily after 12 h following sample preparation at room temperature. CMC of PEG_{5k}-Fmoc-S-S-FTS_2 was determined using pyrene as a fluorescence probe as described[84].

2.3.4 *In Vitro* Cytotoxicity Assay of Drug-free and Drug-loaded PEG_{5k}-Fmoc-S-S-FTS_2 Micelles

DU-145 (2×10^3 cells/well), PC-3 (5×10^3 cells/well) or 4T1.2 (1×10^3 cells/well) cells were seeded in 96-well plates followed by 24 h of incubation in DMEM with 10% FBS and 1% streptomycin/penicillin. For drug-free micelles, after removing old medium, various concentrations of PEG_{5k}-Fmoc-S-S-FTS_2, PEG_{5k}-Fmoc-FTS_2 and free FTS were added in triplicate and cells were incubated for another 72h. The medium was then removed and 100 μL of MTT in PBS (0.5 mg/mL) was added. Four h later, the medium was removed and the MTT formazan was solubilized by DMSO. The absorbance of each well was measured by a microplate-reader, with wavelength at 550 nm and reference wavelength at 630 nm. Untreated

groups were included as controls. Cell viability was calculated as [OD_{treat}-OD_{blank})/($OD_{untreat}$-OD_{blank}) ×100%]. The cytotoxicity of PTX/PEG_{5k}-Fmoc-S-S-FTS_2, PTX/PEG_{5k}-Fmoc-FTS_2 and Taxol® was also similarly tested.

2.3.5 Release of FTS from PEG_{5k}-Fmoc-S-S-FTS_2 inside Tumor Cells

DU-145 (1.6×104 cells/well), PC-3 (4×104 cells/well) or 4T1.2 (8×103 cells/well) cells were seeded in 6-well plates followed by 24 h of incubation in DMEM with 10% FBS and 1% streptomycin/penicillin. After removing the old medium, PEG5k-Fmoc-S-S-FTS2 and PEG5k-Fmoc-FTS2 were added to tumor cells in triplicate and cells were incubated for 72h. Then, iced-cold PBS was added to wash the cells for three times and a mixture of MeOH/H2O (1:1) was added to solubilize those cells. The lysates were collected and centrifuged at 14,000 rpm for 10 min at 4 °C. Supernatant was harvested for UPLC/MS analysis as described before[55].

2.3.6 *In Vitro* PTX Release from PTX/PEG_{5k}-Fmoc-S-S-FTS_2

One mL of PTX/PEG_{5k}-Fmoc-S-S-FTS_2, PTX/PEG_{5k}-Fmoc-FTS_2 and Taxol® at a PTX concentration of 1mg/mL were placed into dialysis bags (MWCO=12 kDa) in triplicate and incubated in 200 mL release medium at 37 °C with gentle shaking. Both normal release medium (DPBS containing 0.5% (w/v) Tween 80) and GSH-containing release medium (normal release medium with 10 mM GSH) were used. Twenty μL of liquids were taken from dialysis bags at 0.5, 1, 2, 4, 6, 8, 12, 24 and 48h. After lyophilization, methanol was added to each tube to solubilize PTX and the concentration of PTX was measured by HPLC with the detection wavelength at 227 nm.

2.3.7 Plasma Pharmacokinetics and Tissue Distribution of PTX-loaded PEG_{5k}-Fmoc-S-S-FTS_2

For plasma pharmacokinetics, PTX-loaded PEG_{5k}-Fmoc-S-S-FTS_2 micelles, PTX-loaded PEG_{5k}-Fmoc-FTS_2 micelles or Taxol® were injected into tumor-free female BALB/c mice via tail-vein at a PTX dose of 10 mg/kg. Five mice were used in each group. Blood samples were collected in heparinized tubes at designated time points (3min, 10min, 30min, 1h, 2h, 4h, 8h and 12h post injection). Samples were centrifuged at 12,500 rpm for 10min at 4 °C and 20 μL of the supernatant were collected. Then 350 μL acetonitrile was added and samples were centrifuged at 12,500 rpm for 5 min at 4 °C. The supernatant was transferred to clean tubes and dried under nitrogen flow. Then the residue was dissolved in 200 μL methanol and centrifuged at 12,500 rpm for 5 min at 4 °C. Fifty μL of the clear supernatant was collected and injected into HPLC for PTX analysis. Noncompartmental pharmacokinetic analysis was executed by WinNonlin.

For tissue distribution study, PTX-loaded PEG_{5k}-Fmoc-S-S-FTS_2 micelles, PTX-loaded PEG_{5k}-Fmoc-FTS_2 micelles or Taxol® were i.v. injected into mice bearing 4T1.2 tumors of 400–600 mm^3 at a PTX dose of 10 mg/kg. Mice were sacrificed 24 h post injection. Major organs (including heart, liver, spleen, lung and kidney) and tumors were harvested, weighed, and stored at -80°C. The samples were similarly processed for PTX assays as described above.

2.3.8 *In Vivo* Therapeutic Study

An aggressive murine breast cancer model (4T1.2) was used to evaluate the antitumor efficacy of PTX-loaded PEG_{5k}-Fmoc-S-S-FTS_2 micelles. 4T1.2 cells (2×10^5 in 200 μL PBS) were inoculated s.c. at the right flank of female BALB/c mice. Once tumor volume reached ~50mm^3, treatments were initiated and this day was marked as day 1. On this day, mice were randomly divided into six groups with five mice in each group, and treated via tail vein injection with PBS, drug-free PEG_{5k}-Fmoc-S-S-FTS_2 micelles, drug-free PEG_{5k}-Fmoc-FTS_2 micelles, PTX-loaded PEG_{5k}-Fmoc-S-S-FTS_2 micelles, PTX-loaded PEG_{5k}-Fmoc-FTS_2 micelles or Taxol® at a PTX dose of 10 mg/kg respectively. The treatment was performed on days 1, 3, 5, 7, 10 and 13. Tumor size was measured with the digital caliper three times a week and calculated by the formula: $(L\times W^2)/2$, where L is the longest and W is the shortest in tumor diameters (mm). The body weights of all mice from each group were measured at the day of each treatment. Mice were sacrificed when the ulceration developed or the tumor size reached ~2000 mm^3. Tumors were weighed at the end of experiment.

2.4 Results

2.4.1 Synthesis and Biophysical Characterization of PEG_{5k}-Fmoc-S-S-FTS_2

PEG5k-Fmoc-S-S-FTS2 was synthesized by conjugating FTS-S-S-COOH with a PEG5K-Fmoc scaffold (Figure 2-1). Briefly, Fmoc-lys-(Boc) and Boc-lys-(Boc) were sequentially linked to PEG5K by the condensation reaction to afford PEG5k-Fmoc-lysine. At

the same time, FTS-S-S-COOH was synthesized via the reaction of FTS with 2,2'-disulfanediylbis(ethan-1-ol) followed by the reaction with succinic anhydride. The synthetic route is shown in Scheme 1. The structure of PEG5k-Fmoc-S-S-FTS2 was confirmed by 1H-NMR (Figure 2-2). The peaks at 3.3 ppm were assigned to the methoxy group on the end of PEG, and the intense peaks at 3.5 ppm were attributed to the methane protons of PEG chain. The peaks between 7.0 and 8.0 ppm corresponded to the aromatic rings of Fmoc group and benzyl rings of FTS. The carbon-hydrogen chains of FTS were located at 1.5-2.2 ppm.

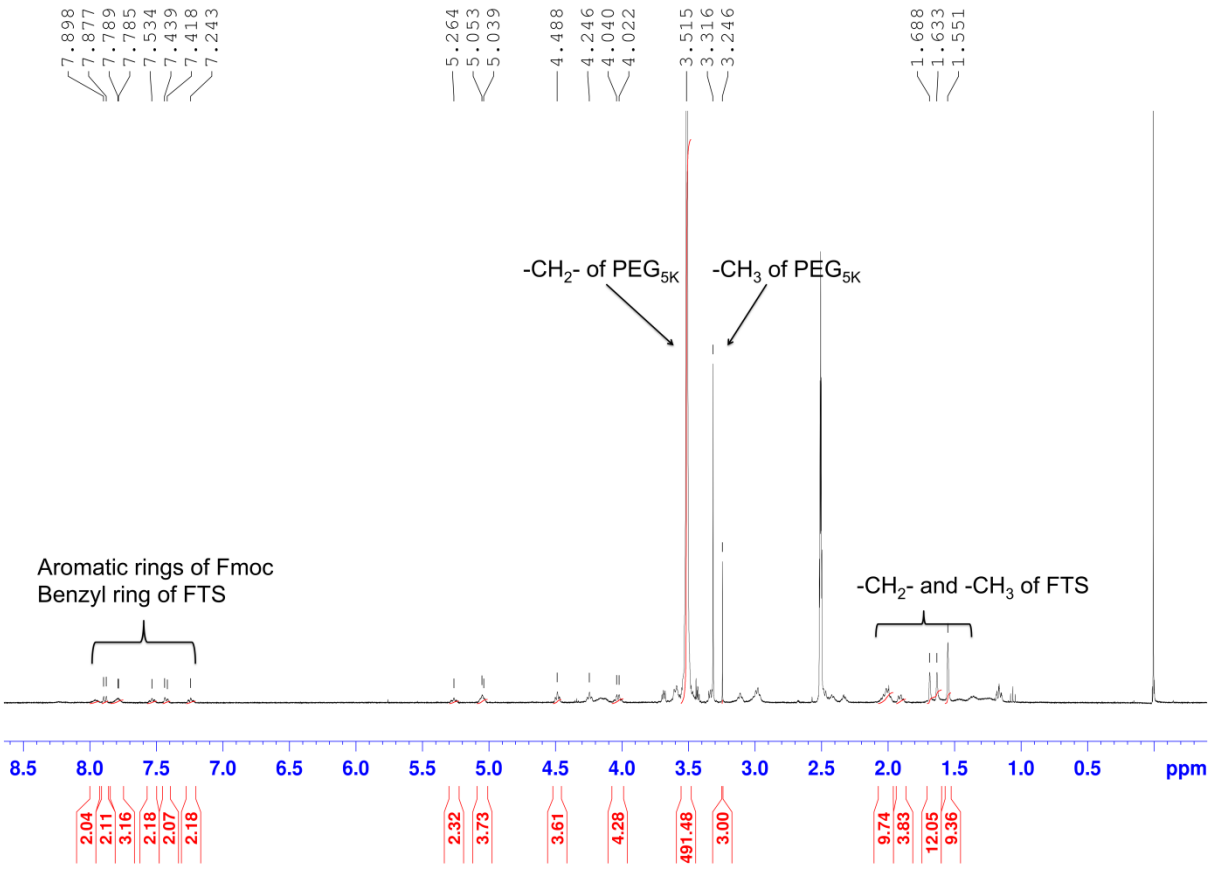

Figure 2-2. ^{1}H-NMR of PEG_{5k}-Fmoc-S-S-FTS_2 conjugate

PEG_{5k}-Fmoc-S-S-FTS_2 readily formed a transparent dispersion in water. The hydrodynamic size of drug-free (Figure 2-3A) and PTX-loaded (Figure 2-3C) PEG_{5k}-Fmoc-S-S-

FTS_2 examined by DLS was around 60 nm. TEM showed elongated, wormlike structure with a uniform size distribution, which was consistent with DLS (Figure 2-3B and C), whereas PEG_{5k}-FTS_2 micelles[39] and PEG_{5k}-Fmoc-FTS_2 micelles[56] listed in Table 1 possessed spherical structures. The size, DLC and formulation stability of PTX-loaded PEG_{5k}-Fmoc-S-S-FTS_2 micelles were then examined and compared to those of PEG_{5k}-Fmoc-FTS_2 and PEG_{5k}-FTS_2 formulations (Table 2-1). PTX could be loaded into PEG_{5k}-Fmoc-S-S-FTS_2 micelles at a carrier/drug ratio as low as 0.25:1. On the contrary, PEG_{5k}-Fmoc-FTS_2 could only load PTX at a carrier/drug ratio of 0.5:1 or higher. For PEG_{5k}-FTS_2, an even higher carrier/drug ratio (2.5:1) was needed to formulate PTX (Table 1). Incorporation of PTX into micelles only resulted in a slight increase in particle sizes for all of the three formulations (Table 2-1). The colloidal stability of PTX-loaded micelles was examined by following the changes in sizes at different times after preparation. With an increase in the carrier/drug ratio, the stability was also significantly improved for all of the three formulations. Overall, the stability of the three formulations follow the order of PTX/PEG_{5k}-Fmoc-S-S-FTS_2 > PTX/PEG_{5k}-Fmoc-FTS_2 > PTX/PEG_{5k}-FTS_2 under all carrier/drug ratios examined (Table 2-1). A carrier/drug molar ratio of 5:1 was used for all subsequent study.

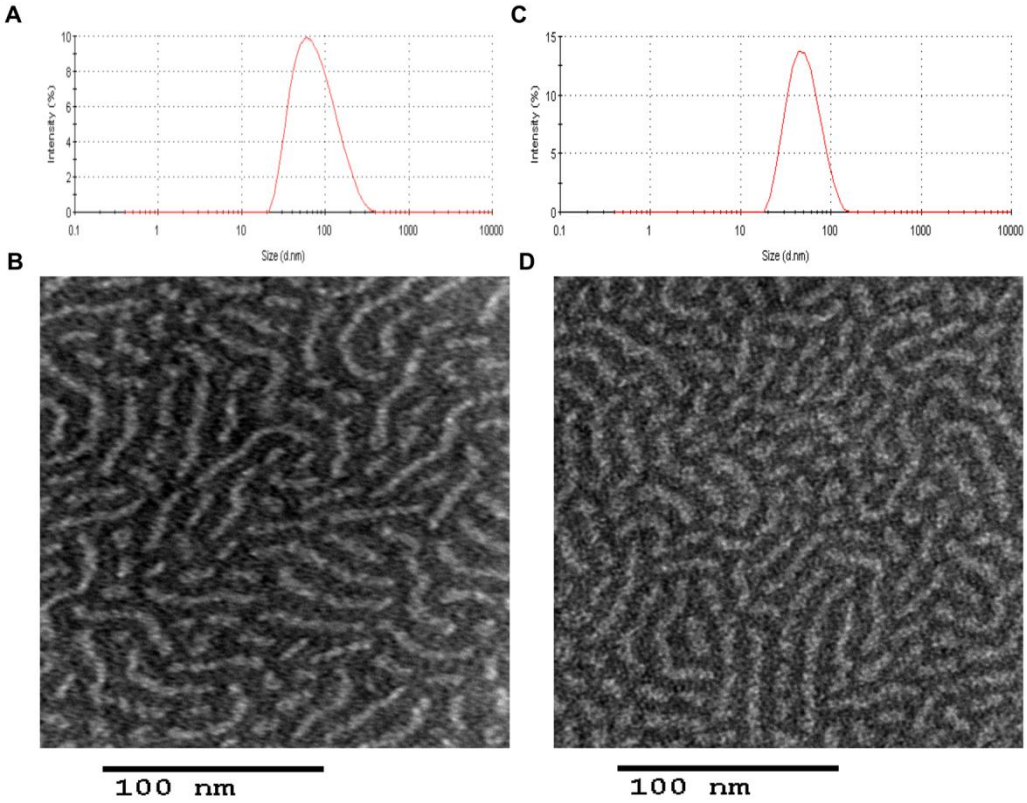

Figure 2-3. Particle size distribution of drug-free PEG_{5k}-Fmoc-S-S-FTS_2 micelles (A) and PTX-loaded PEG_{5k}-Fmoc-S-S-FTS_2 micelles (C). TEM images of drug-free PEG_{5k}-Fmoc-S-S-FTS_2 micelles (B) and PTX-loaded PEG_{5k}-Fmoc-S-S-FTS_2 micelles (D).

Table 2-1 Characterization of drug-free and PTX-loaded PEG_{5k}-Fmoc-S-S-FTS_2 micelles

Micelles	Molar ratio	Conc.of PTX[a] (mg/mL)	Size[b] (nm)	PDI[c]	DLC[d] (%)	DLE[e] (%)	Stability[f] (hours)
PEG_{5K}-FTS_2	-	-	17.6±0.2	0.20	-	-	-
PEG_{5K}-FTS_2: PTX	2.5:1	1	24.9±0.7	0.35	4.5	81.2	2
PEG_{5K}-FTS_2: PTX	5:1	1	25.6±0.4	0.23	2.8	97.6	20
PEG_{5K}-Fmoc-FTS_2	-	-	24.8±0.5	0.22			-
PEG_{5K}-Fmoc-FTS_2: PTX	0.5:1	1	36.2±0.6	0.19	12.1	55.4	12
PEG_{5K}-Fmoc-FTS_2: PTX	1:1	1	29.4±0.7	0.11	9.0	73.2	15

PEG_{5K}-Fmoc-FTS_2: PTX	2.5:1	1	29.7±0.9	0.12	4.6	87.3	17
PEG_{5K}-Fmoc-FTS_2: PTX	5:1	1	25.0±0.3	0.27	2.6	96.0	48
PEG_{5K}-Fmoc-S-S-FTS_2	-	-	94.5±2.8	0.20	-	-	
PEG_{5K}-Fmoc-S-S-FTS_2: PTX	0.25:1	1	108.1±5.4	0.26	34.0	53.5	3
PEG_{5K}-Fmoc-S-S-FTS_2: PTX	0.5:1	1	116.7±6.2	0.26	20.5	67.6	12
PEG_{5K}-Fmoc-S-S-FTS_2: PTX	1:1	1	112.3±4.7	0.24	11.4	86.3	18
PEG_{5K}-Fmoc-S-S-FTS_2: PTX	2.5:1	1	117.0±6.1	0.23	4.9	90.2	24
PEG_{5K}-Fmoc-S-S-FTS_2: PTX	5:1	1	105.6±4.3	0.23	2.5	98.8	72

[a]PTX concentration in micelle was kept at 1 mg/mL. Blank micelle concentration was 20 mg/mL. [b]The size of drug-free or PTX-loaded PEG_{5K}-FTS_2 and PEG_{5K}-Fmoc-FTS_2 was measured directly by Zetasizer. The size of drug-free or PTX-loaded PEG_{5K}-Fmoc-S-S-FTS_2 were calculated according to Stokes-Einstein equation: $L_{eff}= kT/(2\pi\eta D)$, where k is the Boltzmann constant ($1.38 *10^{-23}$ J/K), T is the temperature (298.15 K), η is the viscosity of the solution (0.8872 mPaIs from DLS), D is the diffusion coefficient examined by DLS. [c]PDI = polydispersity index. [d)]DLC = drug loading capacity. [e]DLE = drug loading efficiency. [f]Data mean there was no noticeable size change and visible precipitates during the follow-up period at room temperature.

The CMC of PEG_{5k}-Fmoc-S-S-FTS_2 micelles was determined by a rapid change of fluorescence intensity of loaded pyrene probe during serial dilution. Compared to that of PEG_{5k}-Fmoc-FTS_2 (0.001 mg/mL, 0.17 μM) and PEG_{5k}-S-S-FTS_2 (0.0007 mg/mL, 0.20 μM), PEG_{5k}-Fmoc-S-S-FTS_2 showed a 10-fold decrease in its CMC (0.0002 mg/mL, 0.02 μM) (Figure 2-4).

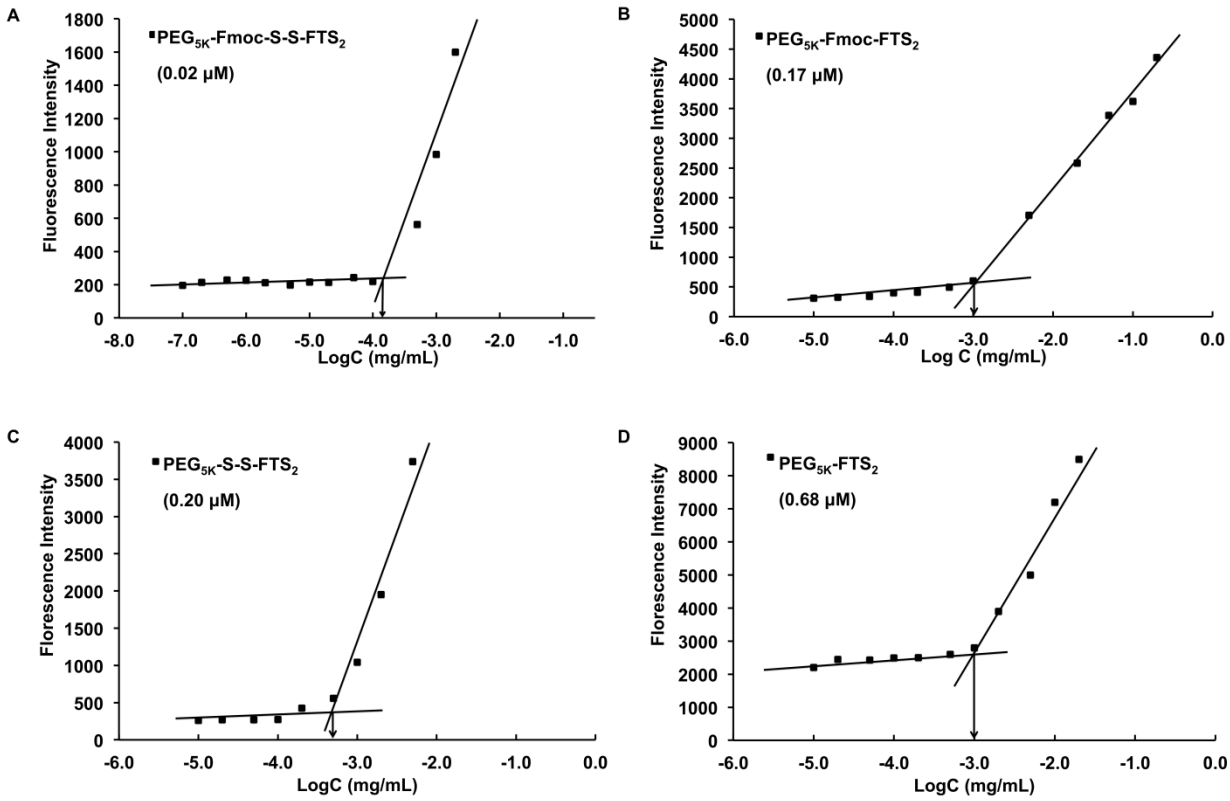

Figure 2-4. CMC of PEG_{5k}-Fmoc-S-S-FTS_2 (A), PEG_{5k}-Fmoc-FTS_2 (B), PEG_{5k}-S-S-FTS_2 (C) and PEG_{5k}-FTS_2 (D) micelles.

2.4.2 In Vitro Cytotoxicity Assay of Drug-free Micelles

The cytotoxicity of drug-free PEG_{5k}-Fmoc-S-S-FTS_2 micelles was tested in DU-145, PC-3 or 4T1.2 cancer cells and compared to that of free FTS and PEG_{5k}-Fmoc-FTS_2 (Figure 2-5A, B and C). Compared to free FTS, both PEG_{5k}-Fmoc-FTS_2 and PEG_{5k}-Fmoc-S-S-FTS_2 showed less cytotoxicity. It was also apparent that PEG_{5k}-Fmoc-S-S-FTS_2 was more active than PEG_{5k}-Fmoc-FTS_2 in cytotoxicity in all of three cell lines tested. The improvement of cytotoxicity of PEG_{5k}-Fmoc-S-S-FTS_2 may be ascribed to the more effective cleavage of disulfide bond and the release of more FTS in treated tumor cells.

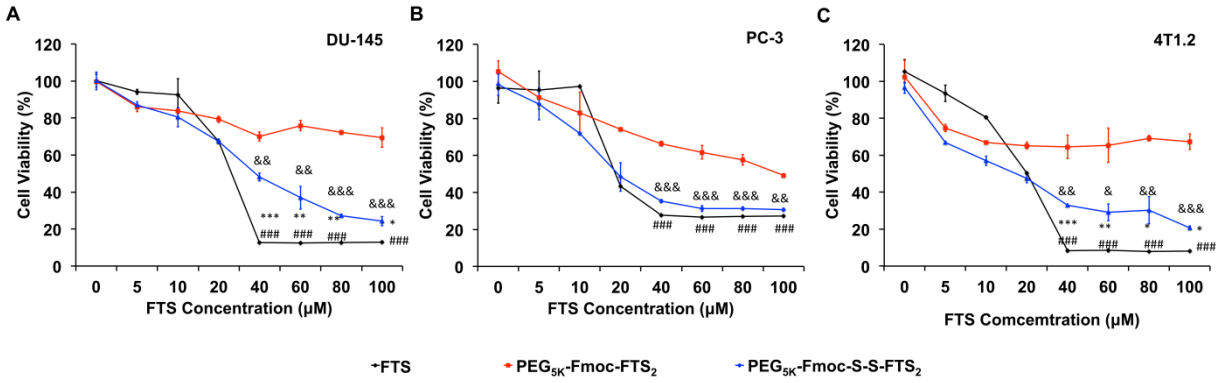

Figure 2-5. Cytotoxicity of drug-free PEG_{5k}-Fmoc-S-S-FTS_2 and PEG_{5k}−Fmoc−FTS_2 micelles compared to free FTS against human prostate cancer cell lines DU-145 (A), PC-3 (B) and mouse breast cancer cell line 4T1.2 (C).

2.4.3 Release of FTS from PEG_{5k}-Fmoc-S-S-FTS_2 Inside tumor cells

To examine if the enhanced cytotoxicity of PEG_{5k}-Fmoc-S-S-FTS_2 is attributed to a more effective FTS release, we examined the amount of free FTS in PC-3, DU145 and 4T1.2 cancer cells by UPLC-MS, 72h following treatment with PEG_{5k}-Fmoc-S-S-FTS_2. As shown in Figure 5, the FTS signals in PEG_{5k}-Fmoc-S-S-FTS_2-treated cells were 2-3 times of that in PEG_{5k}-Fmoc-FTS_2-treated DU-145 (Figure 2-6A) and PC-3 (Figure 2-6B) cells. In murine breast cancer cells 4T1.2 (Figure 2-6C), the amount of FTS released from PEG_{5k}-Fmoc-S-S-FTS_2 was about 1.6 times of that released from PEG_{5k}-Fmoc-FTS_2.

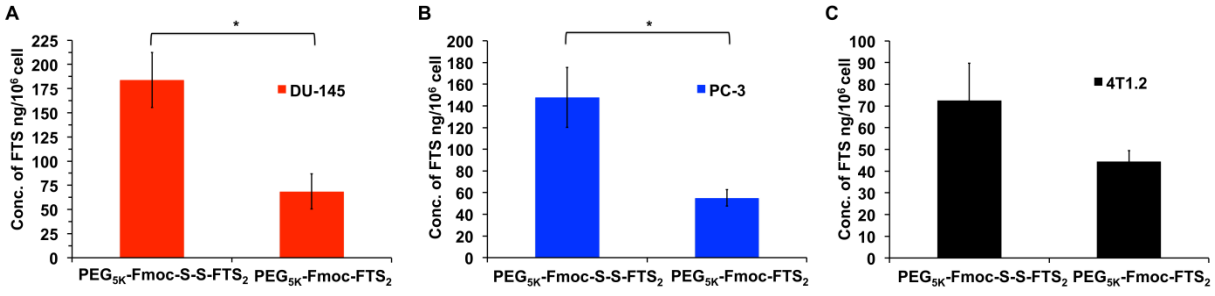

Figure 2-6. UPLC/MS analysis of the amounts of released parent FTS from tumor cells.

Human prostate cancer cell lines DU-145 (A), PC-3 (B) and mouse breast cancer cell line 4T1.2 (C) were treated with PEG_{5k}-Fmoc-S-S-FTS_2 or PEG_{5k}−Fmoc−FTS_2 micelles at a FTS concentration of 20 μM for 72 h. Values reported are the means ± SD for triplicate samples. Significance was determined by one-way ANOVA with Fisher's post hoc test; $^{*}P < 0.05$, $^{**}P < 0.01$, $^{***}P < 0.001$ (PTX/PEG_{5k}-Fmoc-S-S-FTS_2 vs. PTX/PEG_{5k}-Fmoc-FTS_2).

2.4.4 *In Vitro* Cytotoxicity of Drug-Loaded Micelles

The in vitro cytotoxicity of PTX loaded in PEG_{5k}-Fmoc-S-S-FTS_2 and PEG_{5k}-Fmoc-FTS_2 micelles was tested in comparison with Taxol® formulation in DU-145 (Figure 2-7A), PC-3 (Figure 2-7B) and 4T1.2 (Figure 2-7C) cells. Taxol® inhibited the cell proliferation in a dose-dependent manner. PTX formulated in PEG_{5k}-Fmoc-FTS_2 exhibited increased cytotoxicity over Taxol®. More importantly, PTX loaded in PEG_{5k}-Fmoc-S-S-FTS_2 was more potent in killing tumor cells than both Taxol® and PTX-loaded PEG_{5k}-Fmoc-FTS_2 micelles in PC-3, DU-145 and 4T1.2 cells, especially at low PTX doses. Both PEG_{5k}-Fmoc-FTS_2 and PEG_{5k}-Fmoc-S-S-FTS_2 blank micelles showed minimal cytotoxicity at the same carrier concentrations as those used in drug-loaded micelles.

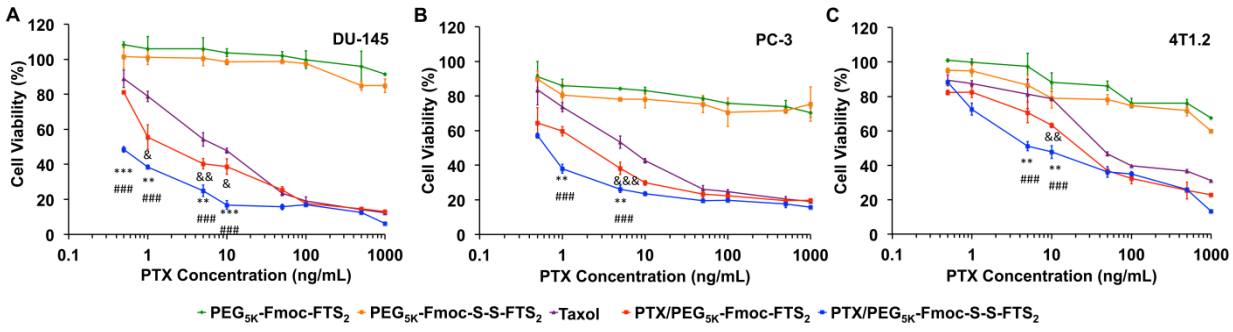

Figure 2-7. Cytotoxicity of drug-free PEG_{5k}-Fmoc-FTS_2, drug-free PEG_{5k}-Fmoc-S-S-FTS_2, PTX-loaded PEG_{5k}-Fmoc-FTS_2 and PTX-loaded PEG_{5k}-Fmoc-S-S-FTS_2 micelles compared to Taxol® formulation against human prostate cancer cell lines DU-145 (A), PC-3 (B) and mouse breast cancer cell line 4T1.2 (C).

Values reported are the means ± SD for triplicate samples. Significance was determined by one-way ANOVA with Fisher's post hoc test; *P < 0.05, **P < 0.01, ***P < 0.001 (PTX/PEG_{5k}-Fmoc-S-S-FTS_2 vs. PTX/PEG_{5k}-Fmoc-FTS_2). #P< 0.05, ##P < 0.01, ###P < 0.001 (PTX/PEG_{5k}-Fmoc-S-S-FTS_2 vs. Taxol®). &P< 0.05, &&P < 0.01, &&&P < 0.001 (PTX/PEG_{5k}-Fmoc-FTS_2 vs. Taxol®).

2.4.5 *In Vitro* PTX Release from PEG_{5k}-Fmoc-S-S-FTS_2

The in vitro PTX release from PEG_{5k}-Fmoc-S-S-FTS_2 in PBS with or without GSH was examined by a dialysis method and compared to that of PTX-loaded PEG_{5k}-Fmoc-FTS_2 and Taxol®. In the normal release medium (Figure 2-8A), PTX release from PEG_{5k}-Fmoc-S-S-FTS_2/PTX was slower than that from PEG_{5k}-Fmoc-FTS_2 /PTX and Taxol®. After 8 hours, 40.6% of PTX was released from PEG_{5k}-Fmoc-FTS_2 formulation, while only 24.0% of PTX was released from PEG_{5k}-Fmoc-S-S-FTS_2 micelles. In a separate experiment, in order to simulate the tumor microenvironment, GSH was added to the release medium to a final concentration of 10 mM. Under this condition, the release of PTX from PEG_{5k}-Fmoc-S-S-FTS_2 formulation was faster than that from PEG_{5k}-Fmoc-FTS_2 and Taxol® formulations (Figure 2-8B). For the initial 8 hours, 74.0% of PTX has already been released from PEG_{5k}-Fmoc-S-S-FTS_2, a 28% increase over PEG_{5k}-Fmoc-FTS_2 formulation. It was also noted that the release of PTX from PEG_{5k}-Fmoc-FTS_2 and Taxol® was not significantly affected by the GSH in release medium.

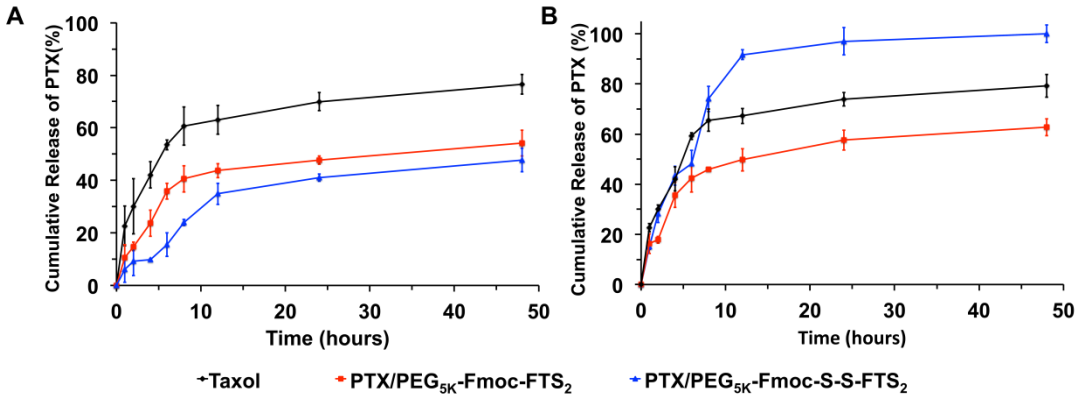

Figure 2-8. Cumulative PTX release profile from Taxol®, PTX-loaded PEG_{5k}-Fmoc-FTS_2 and PTX-loaded PEG_{5k}-Fmoc-S-S-FTS_2 micelles in the normal release medium (A) and the GSH-containing medium (B).

DPBS (pH = 7.4) containing 0.5% (w/v) Tween 80 was used as the normal release medium. Values reported are the means ± SD for triplicate samples**.**

2.4.6 Plasma Pharmacokinetics and Tissue Distribution

PTX-loaded PEG_{5k}-Fmoc-S-S-FTS_2 micelles, PTX-loaded PEG_{5k}-Fmoc-FTS_2 micelles or Taxol® were injected into tumor-free mice at a PTX dose of 10 mg/kg. The plasma concentrations of PTX were examined at different time points. The initial concentration of PEG_{5k}-Fmoc-S-S-FTS_2 at this dose was around 0.7 μM, which was 35-fold higher than its CMC (0.02 μM). The concentrations of PTX in the blood following intravenous injection are shown in Figure 2-9A. Compared to Taxol®, the plasma concentrations of PTX for both PTX-loaded PEG_{5k}-Fmoc-S-S-FTS_2 and PTX-loaded PEG_{5k}-Fmoc-FTS_2 micelles at early time points were significantly higher. Until 12 h, the plasma concentrations of both micellar groups still maintained at relatively high levels. PTX/PEG_{5k}-Fmoc-FTS_2 and PTX/PEG_{5k}-Fmoc-S-S-FTS_2 showed a similar profile with respect to the kinetics of PTX in the blood.

The biodistribution of PTX-loaded PEG_{5k}-Fmoc-S-S-FTS_2 micelles was investigated in female BALB/c mice bearing 4T1.2 breast tumor. Taxol®, PTX-loaded PEG_{5k}-Fmoc-FTS_2 and PTX-loaded PEG_{5k}-Fmoc-S-S-FTS_2 were injected at a same PTX dose of 10 mg/kg. After 24 hours, both tumors and major organs including heart, liver, spleen, lung and kidney were excised and homogenized for PTX determination. As shown in Figure 2-9B, compared to Taxol® group, PTX/PEG_{5k}-Fmoc-S-S-FTS_2 showed more PTX accumulation at tumor site over normal tissues including heart, liver, spleen, lung and kidney. In addition, the tumor uptake of PTX was higher for PTX/PEG_{5k}-Fmoc-FTS_2 and PTX/PEG_{5k}-Fmoc-S-S-FTS_2 compared to Taxol® group. The amounts of PTX accumulated at tumor tissues were also significantly higher in PTX/PEG_{5k}-Fmoc-S-S-FTS_2 treated mice than those in PTX/PEG_{5k}-Fmoc-FTS_2 treated mice. The PTX/PEG_{5k}-Fmoc-S-S-FTS_2 group also showed significant amount of PTX accumulated in the liver and heart, however, there was no significant difference compared to Taxol® or PTX/PEG_{5k}-Fmoc-FTS_2.

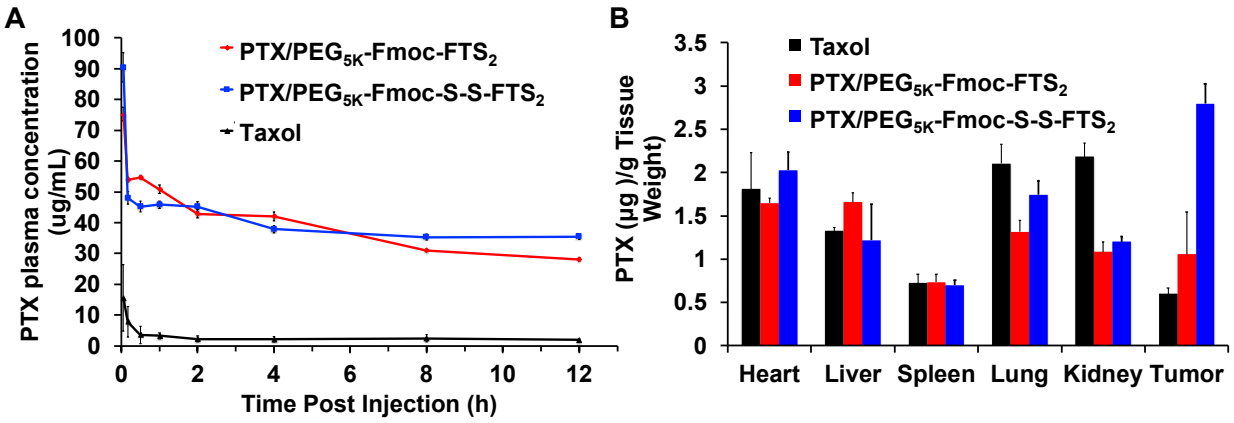

Figure 2-9. Pharmacokenetics and biodistribution of PTX-loaded PEG5k−Fmoc−S-S-FTS2 micelles compared to Taxol® and PTX-loaded PEG5k−Fmoc−FTS2 micelles.

(A) Pharmacokinetics of Taxol®, PTX-loaded PEG5k−Fmoc−FTS2 and PTX-loaded PEG5k−Fmoc−S-S-FTS2 micelles in tumor-free female BALB/c mice. (B) Tissue distribution of PTX 24 h post-injection in tumor-bearing female BALB/c mice treated with Taxol®, PTX-loaded PEG5k−Fmoc−FTS2 and PTX-loaded PEG5k−Fmoc−S-S-

FTS2 micelles. Taxol®, PTX-loaded PEG5k−Fmoc−FTS2 and PTX-loaded PEG5k−Fmoc−S-S-FTS2 micelles were given at the dose of 10 mg PTX/kg, respectively. Values reported are the means ± SEM, n=5.

2.4.7 *In Vivo* Therapeutic Study

The in vivo tumor growth inhibitory effect of PTX-loaded PEG_{5k}-Fmoc-S-S-FTS_2 micelles was investigated in a highly metastatic syngeneic murine breast cancer mode (4T1.2, s.c.). PEG_{5K}-Fmoc-FTS_2 and PEG_{5K}-Fmoc-S-S-FTS_2 alone showed a comparable but low level of antitumor activity (Figure 2-10A). Taxol® group exhibited modest antitumor activity compared to the control group (Figure 2-10A). PTX/PEG_{5k}-Fmoc-FTS_2 was more effective than Taxol® in antitumor activity (Figure 2-10A). At the same dose of PTX, PTX/PEG_{5k}-Fmoc-S-S-FTS_2 was most effective in inhibiting the tumor growth (Figure 2-10A). Figure 2-10B and 9D show the images and weights of tumor tissues that were collected at the end of the experiment, which were consistent with data of tumor growth curves (Figure 2-10A). There were slight increases in body weights in all groups over the period of study, suggesting the negligible toxicity of PTX-loaded PEG_{5k}-Fmoc-S-S-FTS_2 micelles in vivo (Figure 2-10C).

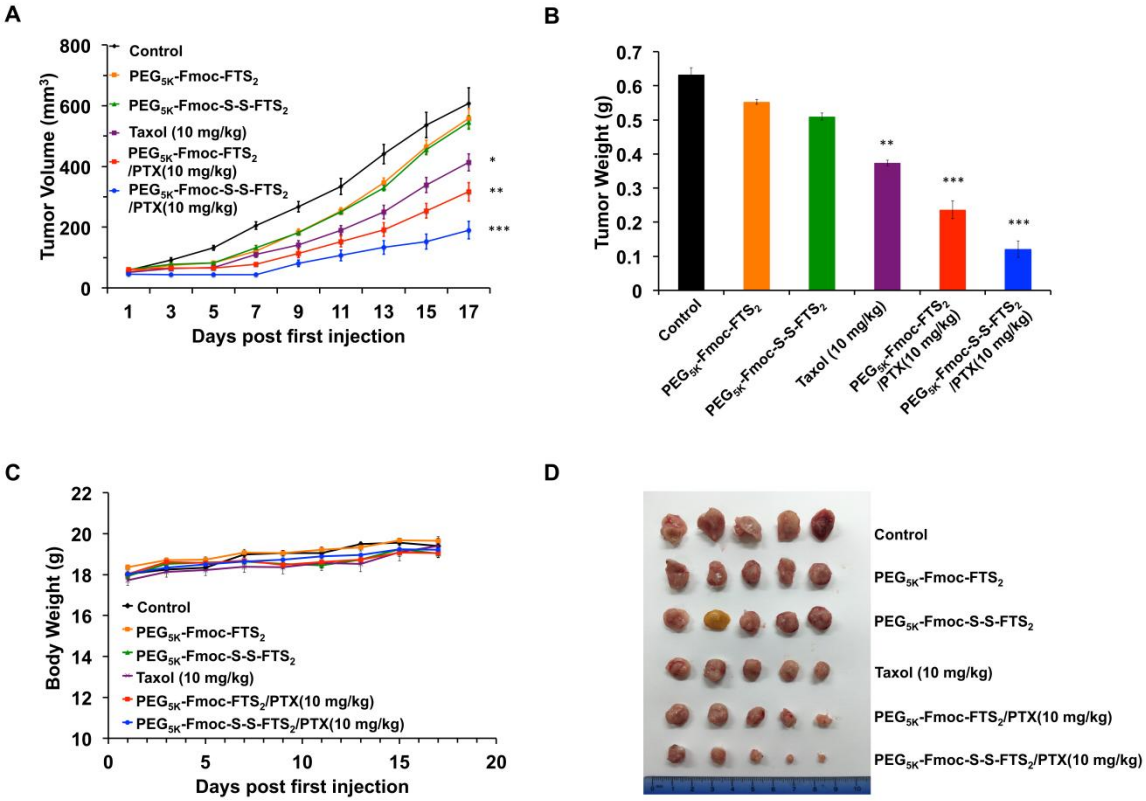

Figure 2-10. Antitumor activity of PTX-loaded PEG_{5k}-Fmoc-S-S-FTS_2 micelles in 4T1.2 breast tumor model.

(A) Antitumor activity of drug-free PEG_{5k}-Fmoc-FTS_2, drug-free PEG_{5k}-Fmoc-S-S-FTS_2 micelles, Taxol®, PTX-loaded PEG_{5k}-Fmoc-FTS_2 and PTX-loaded PEG_{5k}-Fmoc-S-S-FTS_2 micelles in female BALB/c mice bearing 4T1.2 breast tumor. (B) Weights of tumors collected from different groups at the end of experiment. (C) Changes of body weight in mice receiving different treatments. (D) Photographs of tumors collected from different treatment groups at the end of experiment. Values reported are the means ± SEM, n=5. Significance was determined by one-way ANOVA with Fisher's post hoc test; $*P < 0.05$, $**P < 0.01$, $***P < 0.001$ (vs. control).

2.5 Discussion

We previously improved PEG_{5k}-FTS_2 system either by incorporating disulfide bond (PEG_{5k}-S-S-FTS_2) to facilitate drug release at tumor sites[55], or by introducing Fmoc motif

(PEG_{5k}-Fmoc-FTS_2) to enhance the drug loading capacity and the formulation stability[56]. In this study, we combined both disulfide bond and Fmoc group in PEG_{5k}-FTS_2 system and synthesized a novel compound PEG_{5k}-Fmoc-S-S-FTS_2. We hypothesized that our novel PEG_{5k}-Fmoc-S-S-FTS_2 assimilated the advantages from the previous two carriers, while minimizing their potential drawbacks. Our data suggested that PTX loaded in PEG_{5k}-Fmoc-S-S-FTS_2 exhibited superior performance over PTX formulated in PEG_{5k}-Fmoc-FTS_2 in vitro and in vivo.

In contrast to PEG_{5k}-S-S-FTS_2[55] and PEG_{5k}-Fmoc-FTS_2[56] micelles that formed typical spherical structures, PEG_{5k}-Fmoc-S-S-FTS_2 micelles showed predominantly tubular morphology. We have previously shown that PEG_{5K}-$(Fmoc\text{-}OA)_2$ conjugates[85] also exhibited a filamentous structure. Fmoc is known to promote parallel interactions of individual short peptides carrying the same group, which often leads to the formation of elongated nanoassemblies[81]. However, the lipid chain also played a role in the formation of the filamentous structure, as PEG_{5K}-Fmoc[82] conjugate possessed a spherical structure. Moreover, it has been reported that the morphology of the crystalline-coil micelles of block copolymers strongly depended on the lengths of both blocks and composition[86]. As the length of the hydrophobic block increases, micellar morphology is inclined to turn into cylindrical and wormlike. Compared to PEG_{5k}-Fmoc-FTS_2 molecule, PEG_{5k}-Fmoc-S-S-FTS_2 possessed longer lipid chains as well as hydrophobic disulfide bond, which likely contributed to the tubular structures of PEG_{5k}-Fmoc-S-S-FTS_2 micelles. Interestingly, it has been reported that compared to the sphere counterparts, the filomicelles were more resistant to the clearance by macrophages and persisted in circulation for a longer time[87]. The filamentous morphology of PEG_{5k}-Fmoc-S-S-FTS_2 might contribute to its improved performance in vivo.

In addition to its unique structure, PEG_{5k}-Fmoc-S-S-FTS_2 had a CMC that was ~ 10 times lower than that of the counterparts without disulfide bond or Fmoc. The CMC of micellar carriers is known to be controlled by the hydrophilic/hydrophobic ratio[88]. Compared to PEG_{5K}-Fmoc-FTS_2, we introduced additional 16 -C- in addition to two highly hydrophobic disulfide bonds in our PEG_{5K}-Fmoc-S-S-FTS_2 system. The increase of hydrophobic chain could improve carrier/carrier interaction, and further reduce CMC. The reduced CMC shall ensure an improved stability of PEG_{5k}-Fmoc-S-S-FTS_2 micellar system upon the dilution after intravenous injection.

One of the potential concerns over a disulfide-containing carrier is the premature cleavage by the reducing components in the blood such as GSH before it reaches the tumor tissue[89]. However, this is unlikely to happen, as the blood concentrations of GSH are significantly lower than those in the tumor tissues/cells. This concern might be further minimized following the incorporation of a neighboring Fmoc group. Due to its bulky structure, Fmoc may provide a steric hindrance for the attack of the disulfide bond by the relatively low concentrations of GSH. Furthermore, the overall stability of the PEG-Fmoc-S-S-FTS_2 micelles in the blood can be improved by their unique filamentous structures and/or significantly reduced CMC. This is supported by the data that PEG_{5k}-Fmoc-S-S-FTS_2 micelles were even more effective than their counterpart without a disulfide (PEG_{5k}-Fmoc-FTS_2) in mediating selective delivery of PTX to tumor tissues (Figure 2-9B). However, we also observed significant amount of PTX accumulation in the heart and the liver. The mechanism was not clear, which required more studies in the future.

Despite the excellent stability in the blood, PEG_{5k}-Fmoc-S-S-FTS_2 well retained its cleavability by relatively high concentrations of GSH as those seen inside tumor tissues/cells. As shown in Figure 2-6, more free FTS were detected in the tumor cells treated with PEG_{5k}-Fmoc-S-S-FTS_2 compared to PEG_{5k}-Fmoc-FTS_2-treated cells, which was correlated with the improved cytotoxicity of carrier alone for PEG_{5k}-Fmoc-S-S-FTS_2 (Figure 2-5). In addition, PTX/PEG_{5k}-Fmoc-S-S-FTS_2 demonstrated accelerated release of PTX following the addition of GSH into the release medium (Figure 2-8B). The cleavage of the disulfide linkage and then a facilitated release of PTX following disruption of carrier in the tumor tissues/cells shall promote a synergistic action between FTS and PTX as demonstrated by the enhanced cytotoxicity of PTX/PEG_{5k}-Fmoc-S-S-FTS_2 in cultured cancer cells (Figure 2-7).

A highly metastatic murine breast cancer cell line 4T1.2 was selected to investigate the in vivo therapeutic efficacy of PTX-loaded PEG_{5k}-Fmoc-S-S-FTS_2 micelles. PTX/PEG_{5k}-Fmoc-FTS_2 was more effective than Taxol® as we reported before[56]. Importantly, PTX/PEG_{5k}-Fmoc-S-S-FTS_2 was even more effective than the PEG_{5k}-Fmoc-FTS_2 formulation in inhibiting the tumor growth. Meanwhile, no decrease of body weight and no noticeable activity change were found, demonstrating the excellent safety profile of our system. The superior antitumor efficacy along with the minimal toxicity of the PTX/PEG_{5k}-Fmoc-S-S-FTS_2 system could be ascribed to the improved stability in circulation, increased PTX delivery to tumor sites and enhanced drug release inside tumor cells. In addition, the increased delivery of FTS and thus an enhanced synergy with PTX may also contribute to the overall antitumor activity of PTX-loaded

PEG_{5k}-Fmoc-S-S-FTS_2 micelles. Lack of significant antitumor activity by carrier alone is likely due to the low concentrations of FTS at tumor site.

In summary, we have further improved PEG_{5k}-FTS_2 based system via incorporating both disulfide linkage and Fmoc group, forming a simple PEG_{5k}-Fmoc-S-S-FTS_2 micellar system. These filamentous micelles showed enhanced drug loading capacity and formulation stability, along with decreased CMC. PEG_{5k}-Fmoc-S-S-FTS_2 well retained the biological activity of FTS and effectively release FTS at tumor cells. PTX-loaded PEG_{5k}-Fmoc-S-S-FTS_2 showed more potent cytotoxicity in tested tumor cells. Pharmacokinetics and biodistribution studies showed that PTX-loaded PEG_{5k}-Fmoc-S-S-FTS_2 micelles were able to retain PTX in the bloodstream for a prolonged period of time and were highly effective in targeted delivery of PTX to tumors with less accumulation in major organs. More importantly, PTX-loaded PEG_{5k}-Fmoc-S-S-FTS_2 micelles demonstrated more potent antitumor activity over Taxol® formulation and PTX-loaded PEG_{5k}-Fmoc-FTS_2 micelles in vivo.

3.0 Novel Glucosylceramide Synthase Inhibitor Based Prodrug Copolymer Micelles for Delivery of Anticancer Agents

3.1 Abstract

In order to improve the efficacy of chemotherapy for cancers, we have developed a novel prodrug micellar formulation to co-deliver ceramide-generating anticancer agents and ceramide degradation inhibitor (PPMP). The prodrug nanocarrier is based on a well-defined POEG-*b*-PPPMP diblock copolymer. The hydrophilic block of POEG-*b*-PPPMP is POEG, and the hydrophobic block is composed of a number of PPMP units, which could work synergistically with loaded anticancer drugs. POEG-*b*-PPPMP was readily synthesized via a one-step reversible addition-fragment transfer (RAFT) polymerization from a PPMP monomer. The newly synthesized polymers were self-assembled into micelles and served as a carrier for several hydrophobic anticancer drugs including DOX, PTX and C6-ceramide. POEG-*b*-PPPMP prodrug polymer exhibited intrinsic antitumor activity *in vitro* and *in vivo*. In addition, POEG-*b*-PPPMP prodrug polymer was comparable to free PPMP in selectively enhancing the production of pro-apoptotic ceramide species as well as down-regulating the mRNA expression of GCS. DOX-loaded POEG-*b*-PPPMP micelles exhibited an excellent stability of 42 days at 4 °C. Moreover, DOX loaded in POEG-*b*-PPPMP micelles showed higher levels of cytotoxicity than DOX loaded in a pharmacologically inert polymer (POEG-*b*-POM) and Doxil formulation in several tumor cell lines. Consistently, in a 4T1.2 murine breast cancer model, the tumor inhibition followed the order of DOX/POEG-*b*-PPPMP > DOX/POEG-*b*-POM ≥ Doxil > POEG-*b*-PPPMP> POEG-*b*-

POM. Our data suggest that POEG-*b*-PPPMP micelles are a promising dual-functional carrier that warrants more studies in the future.

3.2 Background

Ceramides are not only essential structural components of cell membranes regulating fluidity and subdomain stucture of lipid bilayer, but also have crucial and specific links to various aspects of cancer initiation, progression and response to chemotherapies[90, 91]. As tumor suppressor lipids, ceramides have important messenger functions mediating cell differentiation, cell cycle arrest, senescence and apoptosis[92]. Mounting evidence shows that ceramides are intimately involved in those pathways by regulating specific protein targets such as phosphatases and kinases[93]. Ceramides activate the ceramide-activated protein phosphatases (CAPPs), which comprise the serine/threonine protein phosphatases PP1 and PP2A. PP1 gives rise to the dephosphorylation of SR proteins that mediate the alternative splicing of BCL-X, while PP2A dephosphorylates and inactivates anti-apoptotic proteins such as BCL2 and AKT[94, 95]. Moreover, cathepsin D is activated by ceramides, leading to activation of the pro-apoptotic protein BID and the subsequent activation of caspase-9 and caspase-3[96]. Ceramides also activate the kinase suppressor of RAS (KSR)[97]. Proteins modulated by these pathways include telomerase, c-MYC, caspases and cyclin-dependent kinases (CDKs)[90]. All of these downstream effects can lead to changes in growth arrest, apoptosis and/or senescence. Therefore, manipulating the generation and/or accumulation of the ceramides could disarm a key mechanism for tumour viability and growth. Several ceramide mimetics and delivery systems have been developed to increase the solubility, specificity and efficacy of ceramides[98]. For

example, analogues and mimics of ceramides such as C2- and C6-ceramides, which are similar to the natural metabolites of ceramides, are capable of direct activation of ceramide targets, inducing cell death in a myriad of cancer types[99]. B13, another ceramide analogue, inhibits acid CDase, inducing accumulation of ceramide and increasing apoptosis in an *in vivo* model of metastatic human colon cancer and in a prostate cancer xenograft model[100]. In addition, several delivery systems have been empolyed for systemic delivery of ceramides including liposomes[101], calcium phosphate nanocomposite particles (CPNPs)[102], linear dentritic nanoparticles[103], nanoemulsions[104] and others. For instance, delivery of ceramides via pegylated liposomes, which are generally more effective at crossing the cell membrane, increase accumulation of ceramides and their ability to kill cancer cells[105].

Recently it has been shown that ceramide metalolism can also be modulated by chemotherapy or radiotherapy[106]. Despite the differences in their chemical structures and the postulated major mechanisms of action, many chemotherapeutic agents are all capable of inducing ceramide generation through enhanced *de novo* synthesis, catabolism of sphingomyelin, or both, suggesting a role of ceramide metabolism in the overall antitumor activity of these agents [107]. Doxorubicin, etoposide, camptothecin, 4-HPR, fludarabine, cisplatin, gemcitabine, irinotican, vorinostat or radiation induces *de novo* ceramide genration[108, 109]. A-SMase has been implicated in mediating apoptosis-induced by paclitaxel (PTX), 5-FU, daunorubicin and radiation[106]. Cytosine arabinoside (Ara-C) triggers ceramide generation through the activation of N-SMase[98]. In each case, the result is an enhanced ceramide-governed cytotoxic response.

However, the accumulation of ceramides in tumor cells could simultaneously initiate and/or up-regulate the catabolic pathways towards themselves. Glucosylceramide synthase (GCS) is one of the most pivotal metabolic enzymes to clear ceramides. GCS catalyzes ceramide glycosylation, transferring a glucose residue from UDP-glucose to ceramide for the synthesis of glucosylceramide; this process facilitates ceramide clearance and limits ceramide-induced apoptosis[110-112]. Emerging evidence shows that ceramides increase GCS enzyme activity and GCS mRNA level[113, 114]. More importantly, chemotherapeutic agents, such as DOX, which increase endogenous ceramide levels, have been demonstrated to activate GCS promoter and induce GCS gene expression[115]. Therefore, inhibition of GCS would diminish the ablility of tumor cells to detoxify ceramide and restore the sensitivity of tumor cells to anticancer drugs. PPMP (1-phenyl-2-palmitoylamino-3-morpholino-1- propanol) is a potent inhibitor of GCS and can help sustain a high level of ceramide inside tumor cells through inhibiting its conversion to bio-inactive glycosylated ceramide[116]. PPMP also inhibits l-O-acylceramide synthase, another minor ceramide metabolizing enzyme[117]. Like other inhibitors of GCS, PPMP can both induce cell death by itself and synergize with classical chemotherapeutic agents. The combination of PPMP with anticancer drugs such as PTX[118], 4-HPR[119], irinotican[118] has been reported to cause increased ceramide levels and cytotoxicity on tumor cells, such as those derived from neuroblastoma, melanoma, prostate, lung, colon, breast and pancreatic cancers.

One of the issues for the clinical translation of the combination therapy is lack of an effective strategy for selective codelivery of PPMP and the chemotherapeutic agents. In this study, we developed a PPMP prodrug-based polymeric nanocarrier (POEG-*b*-PPPMP) to overcome this limitation. POEG-*b*-PPPMP could serve as a depot system allowing the release of

active PPMP over a prolonged period of time. More importantly, POEG-*b*-PPPMP could self-assemble to form micelles to achieve synergistic codelivery with other anticancer drugs including DOX, PTX and C6-ceramide. We systematically evaluated the sizes, structures and drug loading efficiency of POEG-*b*-PPPMP-based nanocarrier. The antitumor activity of drug-free POEG-*b*-PPPMP and DOX-loaded POEG-*b*-PPPMP was also investigated *in vitro* and *in vivo*.

3.3 Experiment Procedures

3.3.1 Materials

PPMP·HCl was synthesized and purified following a published patent (WO 2005/049827 A2). Methacryl chloride, triethylamine, 4-Cyano-4-[(dodecylsulfanylthiocarbonyl)sulfanyl]pentanoic acid, oligo(ethylene glycol) methacrylate OEGMA (average Mn = 500), 2,2-Azobis (isobutyronitrile)(AIBN), Dulbecco's Modified Eagle's Medium (DMEM), trypsin-EDTA solution, 3-(4,5-dimethylthiazol-2-yl)-2,5-diphenyl tetrazolium bromide (MTT) were purchased from Sigma-Aldrich (MO, U.S.A). DOX·HCl was purchased from LC Laboratories (MA, U.S.A). PTX was purchased from AK Scientific Inc. (CA, U.S.A.). Fetal bovine serum (FBS), penicillin-streptomycin solution and TRIzol lysis reagent were purchased from Invitrogen (NY, U.S.A.). QuantiTect Reverse Transcription Kit was purchased from Qiagen (MD, U.S.A).

3.3.2 Synthesis of PPMP-monomer

Methacryloyl chloride (209 uL, 2 mmol) was added to the solution of PPMP·HCl salt (511 mg, 1 mmol) in 5 mL DCM, followed by triethylamine (689 uL, 5mmol) at 0 °C. The reaction mixture was stirred at 0 °C for 1 h and then kept at room temperature overnight. The completion of reaction was monitored by TLC (Petroleum ether/EtOAc = 9:1). The reaction mixture was quenched by the addition of saturated $NaHCO_3$, and the product was extracted with DCM (3×15 mL). The organic phase was collected and washed by water and brine, dried over Na_2SO_4, filtered, and the solvent was then evaporated. The crude product was purified by column chromatography on silica gel eluted with petroleum ether/EtOAc (12: 1) to give the oil product PPMP monomer (450 mg, 90%).

3.3.3 Synthesis of POEG macroCTA

POEG macroCTA was synthesized and purified following a published protocol [43].

3.3.4 Synthesis of POEG-*b*-PPPMP

POEG macroCTA (390 mg, 0.052 mmol), PPMP-monomer (225 mg, 0.415 mmol), AIBN (4.5 mg, 0.027 mmol), and 2 mL dried 1, 4-Dioxane and THF (V/V=1/1) were added in a Schlenk tube and deoxygenated by free-pump-thawing for three times. Under N_2 protection, the mixture was kept in an oil bath thermostated at 90°C for 24 h, and then quenched by cooling the tube in liquid nitrogen. The mixture was precipitated in hexane for 3 times and dried in vacuum.

3.3.5 Preparation and Characterization of Blank or Drug-loaded POEG-*b*-PPPMP micelles

DOX solution was first prepared by dissolving DOX·HCl in a mixture of chloroform/methanol (1:1, v/v) containing triethylamine (5 equiv) to remove HCl. Then DOX (5mg/mL in chloroform/methanol) was mixed with POEG-*b*-PPPMP polymers (50 mg/mL in chloroform) at different carrier/drug ratios. The solvent was removed by nitrogen flow to produce a thin film of carrier/drug mixture, which was further dried in vacuum for 2 h to remove any remaining solvent. Then the thin film was hydrated and gently vortexed in Dulbecco's phosphate-buffered saline (DPBS) to form DOX-loaded micelles. PTX-loaded, C6-ceramide-loaded POEG-*b*-PPPMP micelles and drug-free micelles were prepared similarly as described above.

The average diameter and the size distribution of POEG-*b*-PPPMP micelles were assessed via a Zetasizer (DLS). The morphology of POEG-*b*-PPPMP blank micelles and drug-loaded micelles was observed by transmission electron microscopy (TEM). The drug loading efficiency of DOX and PTX was examined by Waters Alliance 2695 Separations Module combined with Waters 2475 Fluorescence Detector (excitation, 490 nm; emission, 590 nm; gain, 3; sensitivity (FUFS), 10,000) and high performance liquid chromatography (HPLC) respectively as described previously [120]. Drug loading capacity (DLC) and drug loading efficiency (DLE) were calculated according to the following equation: DLC %= [weight of drug loaded/(weight of polymer used + weight of drug used)]×100%, DLE %= (weight of loaded drug/weight of input drug)×100 %. The colloidal stability of drug-loaded micelles with various carrier/drug molar ratios at room temperature and 4°C was evaluated by following the changes in sizes of the

particles or visible precipitates every hour in the first 12 h and daily after 12 h following sample preparation.

The CMC of POEG-*b*-PPPMP micelles was determined by using nile red as a fluorescence probe as described previously[121].

The kinetics of DOX release from DOX/ POEG-*b*-PPPMP was performed according to a previous report[122].

3.3.6 *In Vitro* Cytotoxicity Assay

Cytotoxicity assay was performed on 4T1.2 mouse breast cancer cells, MCF-7 human breast cancer cells and PC-3 human prostate cancer cells. 4T1.2 (1×10^3 cells/well), MCF-7 (5×10^3 cells/well) or PC-3 (3×10^3 cells/well) cells were seeded in 96-well plates followed by 24 h of incubation in DMEM with 10% FBS and 1% streptomycin/penicillin.

To evaluate the combinational effect of PPMP with other anticancer drugs, cells were treated with various concentrations of free PPMP, free DOX·HCl, and the combination of both respectively for 48 h. The combination of PPMP and PTX or C6-ceramide was evaluated similarly. To measure the cytotoxicity of blank POEG-*b*-PPPMP micelles, cells were challenged with various concentrations of blank POEG-*b*-PPPMP micelles or free PPMP at equivalent

PPMP concentrations for 48 h. To explore the cytotoxicity of drug-loaded POEG-*b*-PPPMP micelles, a pharmacologically inert polymer, POEG-*b*-POM, was served as a control carrier for anticancer drugs. Six groups were tested in this experiment, including free anticancer drug, commercial formulation of anticancer drug, drug-loaded POEG-*b*-PPPMP micelles, drug-loaded POEG-*b*-POM micelles, drug-free POEG-*b*-PPPMP micelles and drug-free POEG-*b*-POM micelles. The former four drug-containing groups were compared at the same concentration of anticancer drugs. The concentrations of last two drug-free micelles were same as those of the carrier in drug-loaded groups respectively. Specifically, for testing of DOX-loaded micelles, tumor cells were challenged with various concentrations of free DOX·HCl, Doxil, POEG-*b*-PPPMP/DOX micelles, POEG-*b*-POM/DOX micelles, POEG-*b*-PPPMP micelles and POEG-*b*-POM micelles. For testing of PTX-loaded micelles, cells were incubated with PTX, Taxol®, POEG-*b*-PPPMP/PTX micelles, POEG-*b*-POM/PTX micelles, POEG-*b*-PPPMP micelles and POEG-*b*-POM micelles for 48 h.

MTT assay and the calculation of cell viability were performed as described before[122]. The anti-proliferation data for single drug and combination treatment was fitted to an inhibitory, normalized dose-response model with variable slope (Y = 100/(1 + 10^((LogEC50-X) *HillSlope); (GraphPad Prism, San Diego, CA)

3.3.7 Real-time PCR

Real-time PCR studies were performed on 4T1.2 mouse breast cancer cells and MCF-7 human breast cancer cells. 4T1.2 (2×10^4 cells/well) or MCF-7 (6×10^4 cells/well) cells were seeded in 6-well plates followed by 24 h of incubation in DMEM containing 10% FBS and 1%

streptomycin/penicillin. After 24 hours, medium was replaced with 2% FBS medium containing free PPMP, blank POEG-*b*-PPPMP, DOX•HCl, free PPMP + free DOX or POEG-*b*-PPPMP/DOX. Free PPMP, blank POEG-*b*-PPPMP and POEG-*b*-PPPMP/DOX were examined at the same concentration of PPMP (1.7 μM), while free DOX and POEG-*b*-PPPMP/DOX were compared at the same concentration of DOX (100 nM). After 48 hours, total cellular RNA was extracted using the TRIzol lysis reagent. cDNA was generated from the purified RNA using QuantiTect Reverse Transcription Kit according to the manufacturer's instructions. The cDNAs corresponding to GCS were amplified by PCR using the specific primers (mouse GCS forward 5'-CCAGGAGGGAATGGCCTTGT-3', mouse GCS reverse 5'-AGAGACACCAGGGAGCTTGC-3'; human GCS forward 5'- CCACCCTGTCCTCCTCCTG-3', human GCS reverse 5'- GAAGACGGCCATTCCCTCCA-3'). Quantitative real-time PCR was performed using SYBR Green Mix on a 7900HT Fast Real-time PCR System. Relative target mRNA levels were analyzed using delta-delta-Ct calculations and normalized to GAPDH.

3.3.8 Analysis of lipids

Ceramides measurements were also carried out on 4T1.2 cells or MCF-7 cells. All cells were similarly treated as described above. After 48 h treatment, cells were washed twice with ice-cold DPBS and lysed in 60 μL 0.2% sodium dodecyl sulfate (SDS). An aliquot (30 μL) of the cell lysates was taken for protein determination. For another aliquot (30 μL) of the cell lysates, 0.5 μg of C6-ceramide was added as the internal standard. Lipids were extracted using 400 μL of chloroform/methanol (3:1, v/v). After gentle vortex and centrifugation at 3,000 rpm at RT for 10 min, the resulting organic lower phase was collected and evaporated under a stream of

nitrogen. Lipids were resuspended in 200 μL ACN/IPA/H_2O (1:1:1, v/v/v) and centrifuged at 12,500 rpm for 10 min at 4 °C and 150 μL of the clear supernatant was collected in UPLC injection vials. Sphingolipids were separated on an Agilent 1200 high performance liquid chromatography system (Agilent Technologies, CA, U.S.A) and analyzed by electrospray ionization-tandem mass spectrometry on a 400 QTRAP (AB Sciex, MA, U.S.A). The peak areas for different sphingolipid subspecies (C16-ceramide, C18-ceramide, C20-ceramide, C22-ceramide and C24-ceramide) were quantified by internal standards (C6-ceramide) and then normalized to protein concentrations.

3.3.9 Plasma Pharmacokinetics and Tissue Distribution

For plasma pharmacokinetics, POEG-*b*-PPPMP/DOX micelles, POEG-*b*-POM/DOX and DOX·HCl were injected intravenously into groups of 5 tumor-free female CD1 mice at a DOX dose of 5 mg/kg, respectively. Blood samples were collected in heparinized tubes at designated time points (3min, 10 min, 30 min, 1 h, 2 h, 4 h, 8 h and 12 h) post injection. The samples were centrifuged at 12,500 rpm for 10 min at 4 °C and 20 μL of the supernatant was collected. Then 200 μL acetonitrile was added and the samples were vortexed for 1 min. The samples were centrifuged at 12,500 rpm for 10 min at 4 °C and 150 μL of the clear supernatant was collected and injected into HPLC for DOX analysis. Noncompartmental pharmacokinetic analysis was executed by WinNonlin.

For tissue distribution study, POEG-*b*-PPPMP/DOX micelles, POEG-b-POM/DOX and DOX·HCl were i.v. injected into female BALB/c mice bearing 4T1.2 tumors of 400–600 mm^3 (n = 5) at a DOX dose of 5 mg/kg, respectively. Mice were sacrificed 24 h post injection. Major

organs (including heart, liver, spleen, lung and kidney) and tumors were harvested, weighed, and stored at -80°C. One hundred mg of each organ was weighed and homogenized in 500 μL PBS on ice. Five hundred μL methanol/acetonitrile (1/1, v/v) was then added and vortexed for 3 min. The samples were centrifuged at 12,500 rpm for 10 min at 4 °C and the supernatant was transferred to clean tubes and dried under nitrogen flow. Two-hundred μL acetonitrile was added and vortexed to dissolve samples, which were then centrifuged at 12,500 rpm for 10 min at 4 °C. One hundred and fifty μL of the clear supernatant was collected and injected into HPLC for DOX analysis.

3.3.10 *In Vivo* Therapeutic Study

The in vivo antitumor efficacy of the DOX-loaded POEG-b-PPPMP micelles was tested in a syngeneic 4T1.2 mouse breast cancer model. 4T1.2 cells (2×105 in 20 μL DPBS) were inoculated s.c. at the right mammary fat pad of female BALB/c mice. When the tumor volume reached ~ 50 mm3, mice were randomly divided into six groups (n=5), and treated via tail vein injection with DPBS, blank POEG-b-PPPMP micelles, blank POEG-b-POM micelles, DOX-loaded POEG-b-PPPMP micelles, DOX-loaded POEG-b-POM or Doxil, respectively, at a DOX dose of 5 mg/kg. The treatments were conducted every three days for a total of 3 times. Tumor sizes were measured with the digital caliper every three days following the initiation of the treatment and calculated by the formula: (L×W2)/2, where L is the longest and W is the shortest in tumor diameters (mm). Body weights were also monitored for the indication of toxicity. On 23 days post injection, all mice were sacrificed and tumor tissues were collected for weight, photography and H&E staining.

3.3.11 Histochemical Staining

The H&E staining was similarly conducted as described before[123].

3.3.12 Statistical Analysis

In vitro or in vivo data are presented as mean ± standard deviation (SD) or mean± standard error of mean (SEM), respectively. Two-tailed Student's T test or analysis of variance (ANOVA) was used to compare two groups or multiple groups, respectively. Significance was determined with Tukey simultaneous post hoc test. In all statistical analyses, $P < 0.05$ is considered statistically significant.

3.4 Results

3.4.1 Effect of Anticancer Drugs on GCS mRNA Expression

To evaluate the effect of DOX, PTX, or C6-ceramide on GCS expression, we treated MCF-7 cells with various concentrations of DOX, PTX and C6-ceramide, respectively. The expression of GCS mRNA was examined by RT-qPCR 48 h following the drug treatment. As shown in Figure 3-1A, treatment of MCF-7 cells with either DOX or C6-ceramide led to significant increases in the mRNA expression levels of GCS in a dose-dependent manner. At a DOX concentration of 200 nM and a C6-ceramide concentration of 2 μM, the GCS mRNA expression levels in MCF-7 cells were increased by 4.2 and 6.5-fold respectively. Induction of

GCS mRNA expression by DOX or C6-ceramide was similarly observed in 4T1.2 cells (Figure 3-1B). However, induction of GCS expression by DOX or C6-ceramide was less dramatic in 4T1.2 cells compared to that in MCF-7 cells. Treatment with PTX also led to significant induction of GCS expression in MCF-7 cells but not in 4T1.2 cells. These results suggest that ceramides generated in tumor cells in response to chemotherapeutic stress upregulate GCS expression to detoxify ceramides and prevent cell death.

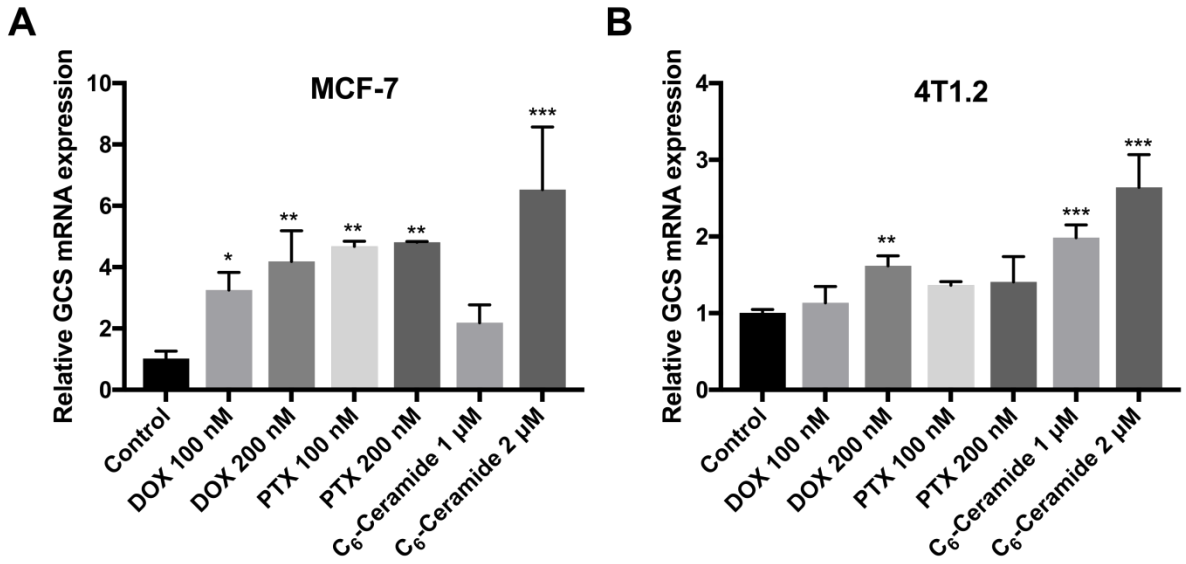

Figure 3-1. Effects of chemotherapies on GCS mRNA expression in MCF-7 (A) and 4T1.2 (B) cell after 48 h treatment.

Data are presented as the means ± SD for triplicate samples. P values were generated by one-way ANOVA using the Dunnett test for multiple comparisons to one control (*P < 0.05, **P < 0.01, *** P < 0.001).

3.4.2 Effect of Combination of PPMP and Other Chemotherapeutic Drugs on Tumor Cell Proliferation

To assess whether GCS inhibitor PPMP could further enhance the cytotoxicity and/or restore sensitivity of tumor cells to the action of anticancer drugs, we evaluated the growth inhibitory activity of combination treament of PPMP with other anticancer drugs in MCF-7, 4T1.2 and PC-3 cell lines. As shown in Figure 3-2A, PPMP or DOX alone caused a concentration-dependent inhibition of MCF-7 cell proliferation. It is also apparent that combination of the two led to a significant improvement in the level of cytotoxicity. Similar synergistic effects between PPMP and DOX were found in 4T1.2 (Figure 3-2B) and PC-3 (Figure 3-2C) cells. PPMP also synergized with PTX or C6-ceramide in inhibiting the tumor cell proliferation in all tumor cell lines tested (Figure 3-2D~J). Combination index (CI) was then calculated to assess a potential synergy between PPMP and other anticancer drugs, by the equation $CI=(d1/IC_{50}1)+ (d2/IC_{50}2)$, with d1 or d2 being the concentration of PPMP or other anticancer agent (DOX, PTX or C6-ceramide) required to achieve 50% killing effect in co-treatment, while $IC_{50}1$ or $IC_{50}2$ being IC_{50} of PPMP or other anticancer agents in single treatment, respectively. All of CI values listed in Table 3-1 were less than 1, indicating the synergy between PPMP and DOX, PTX or C6-ceramide in all of the examined cancer cell lines.

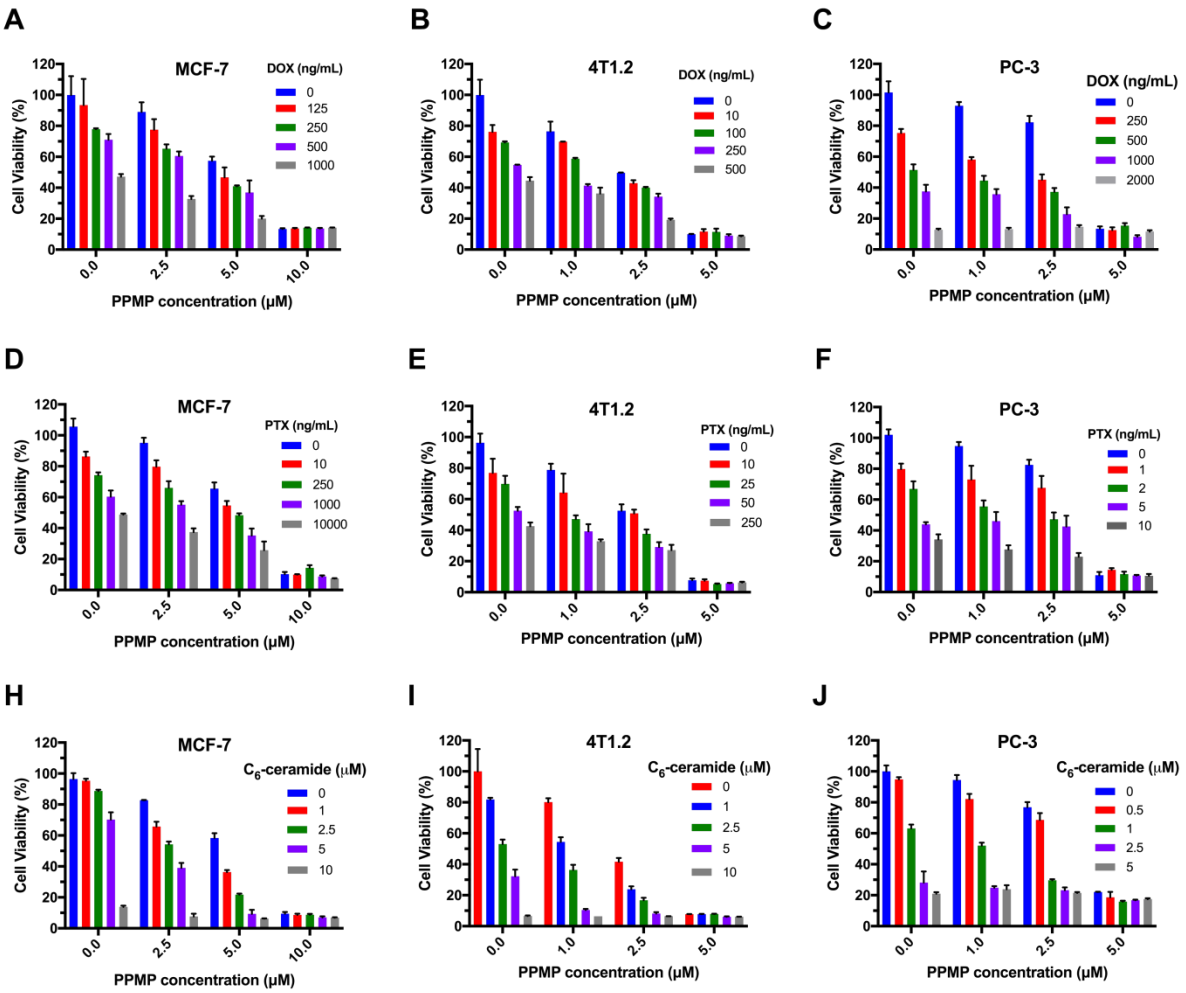

Figure 3-2. Synergistic effect between PPMP and other anticancer drugs in inhibiting the proliferation of tumor cells.

(A-C) MCF-7, 4T1.2 or PC-3 cells were treated with various concentrations of free PPMP, free DOX or the combination of PPMP and DOX. (D-F) MCF-7, 4T1.2 or PC-3 cells were treated with various concentrations of free PPMP, free PTX or the combination of PPMP and PTX. (G-I) MCF-7, 4T1.2 or PC-3 cells were treated with various concentrations of free PPMP, free C6-ceramide or the combination of PPMP and C6-ceramide. After 48 h, the cytotoxicity was determined by MTT assay. The experiments was performed in triplicate and repeated three times. Data are presented as means ± SD.

Table 3-1. Synergistic Antiproliferative Activity of PPMP and Other Anticancer Drugs in Cancer Cells

Drug1	Drug2	Cell Lines	d1 (μM)	$D_{50}1$ (μM)	d2 (ng/mL)[a] (μM)[b]	$D_{50}2$ (ng/mL)[a] (μM)[b]	CI
PPMP	DOX	MCF-7	3.8±0.6	5.7±0.4	250	964.3±106.6	0.93
PPMP	DOX	4T1.2	1.8±0.3	2.2±0.1	10	272.0±62.1	0.85
PPMP	DOX	PC-3	1.5±0.3	3.4±0.1	250	629.4±33.6	0.84
PPMP	PTX	MCF-7	4.1±0.5	5.7±0.4	250	7143.0±1866.0	0.75
PPMP	PTX	4T1.2	1.0±0.3	2.2±0.1	25	108.1±18.1	0.69
PPMP	PTX	PC-3	1.5±0.4	3.4±0.1	2	4.3±0.2	0.91
PPMP	Ceramide	MCF-7	3.6±0.1	5.7±0.4	1	6.2±0.2	0.79
PPMP	Ceramide	4T1.2	1.1±0.2	2.2±0.1	1	2.8±0.2	0.86
PPMP	Ceramide	PC-3	1.1±0.4	3.4±0.1	1	1.6±0.1	0.95

a) Unit of DOX and PTX. b) Unit of C_6-ceramide. Combination Index (CI) of co-treatment of PPMP with DOX, PTX and C6-ceramide in MCF-7, 4T1.2 and PC-3 cells. The cell viability was determined by MTT assay. The anti-proliferation data for single drug and combination treatment was fitted to an inhibitory, normalized dose-response model with variable slope (Y = 100/(1 + 10^((LogEC50-X) *HillSlope); (GraphPad Prism, San Diego, CA). The CI was calculated by the formula: $CI=(d1/D_{50}1)+(d2/D_{50}2)$, where $D_{50}1$ is the IC_{50} of PPMP in single treatment, and d1 is the concentration of PPMP required to achieve 50% inhibition effect with d2 in co-treatment. Similarly, $D_{50}2$ is IC_{50} of DOX, PTX or C6-ceramide in single treatment, and d2 is the concentration of DOX, PTX or C6-ceramide required to obtain the same 50% cell-killing effect in combination with d1. The CI values are interpreted as follows: <1.0, synergism; 1.0, additive; and >1.0, antagonism. The experiments was performed in triplicate and repeated three times.

3.4.3 Synthesis and Characterization of the POEG-*b*-PPPMP Polymers

First, PPMP·HCl was synthesized following a published patent (WO 2005/049827 A2) and its chemical identity was confirmed by ^{1}H-NMR (Figure 3-3). Then PPMP was conjugated with methacryloyl chloride through a hydrolyzable ester linkage as shown in Figure 3-4. The structure of PPMP monomer was confirmed by ^{1}H-NMR (Figure 3-5). Meanwhile, the macro-chain transfer agent POEG was synthesized by RAFT polymerization of hydrophilic OEGMA

monomer according to a published method [43]. POEG (MW=7500) was then used to initiate the polymerization of hydrophobic PPMP monomer, yielding the amphiphilic POEG-*b*-PPPMP block copolymer. The structure of POEG-*b*-PPPMP was confirmed by ^{1}H-NMR (Figure 3-6), and the average degree of polymerization of the PPMP monomers was calculated by comparing the intensity of I_b and I_a. The calculated molecular weight by ^{1}H-NMR was M_n=11700. The molecular weight detected by gel permeation chromatography (GPC) was M_n=12100 with narrow polydispersity (PDI) of 1.3, which was consistent with molecular weight calculated by ^{1}H-NMR. Therefore, each POEG-*b*-PPPMP molecule contained 15 units of OEGMA and 7 units of PPMP, denoted by $POEG_{15}$-*b*-$PPPMP_7$.

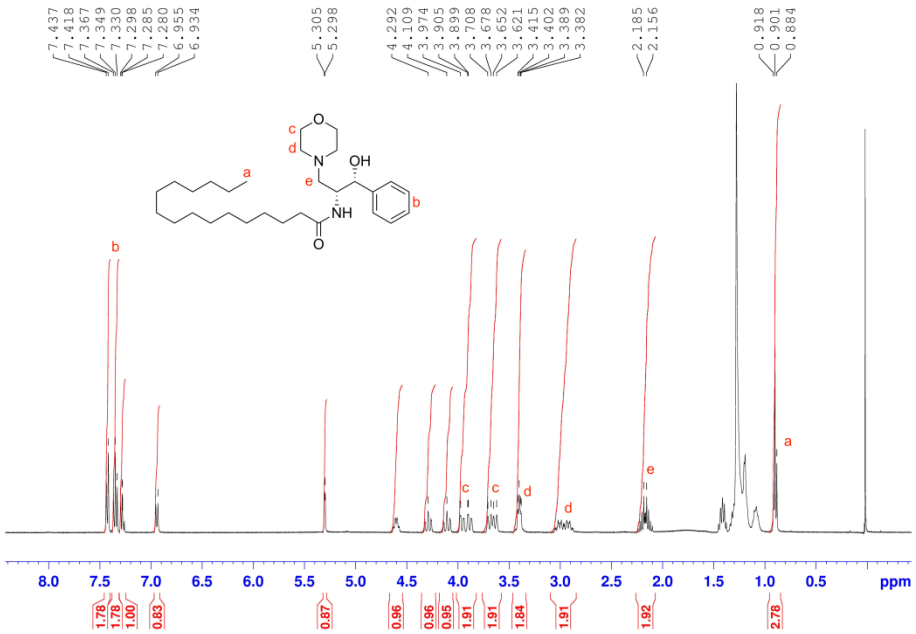

Figure 3-3. ^{1}H-NMR of PPMP in $CDCl_3$.

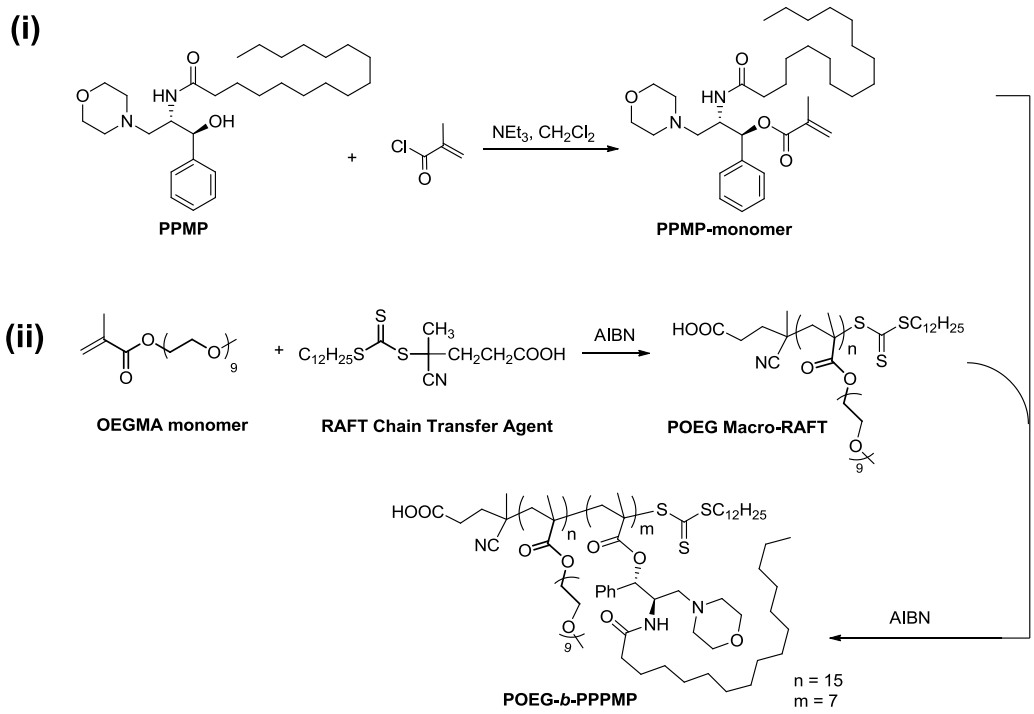

Figure 3-4. Synthesis Scheme of POEG-*b*-PPPMP Conjugate.

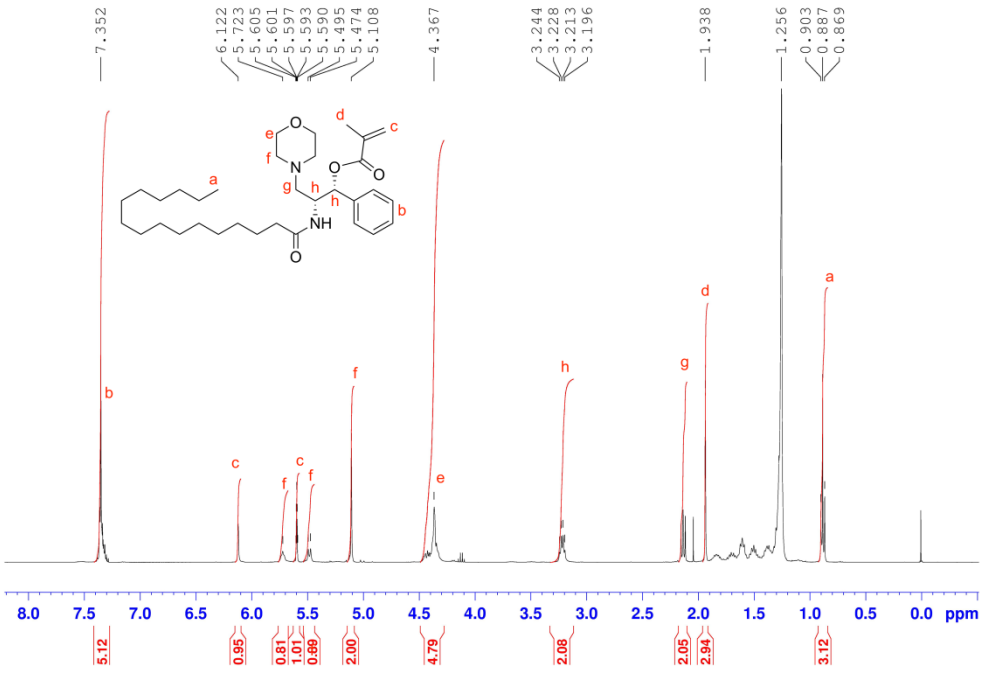

Figure 3-5. ^{1}H-NMR of PPMP monomer in $CDCl_3$.

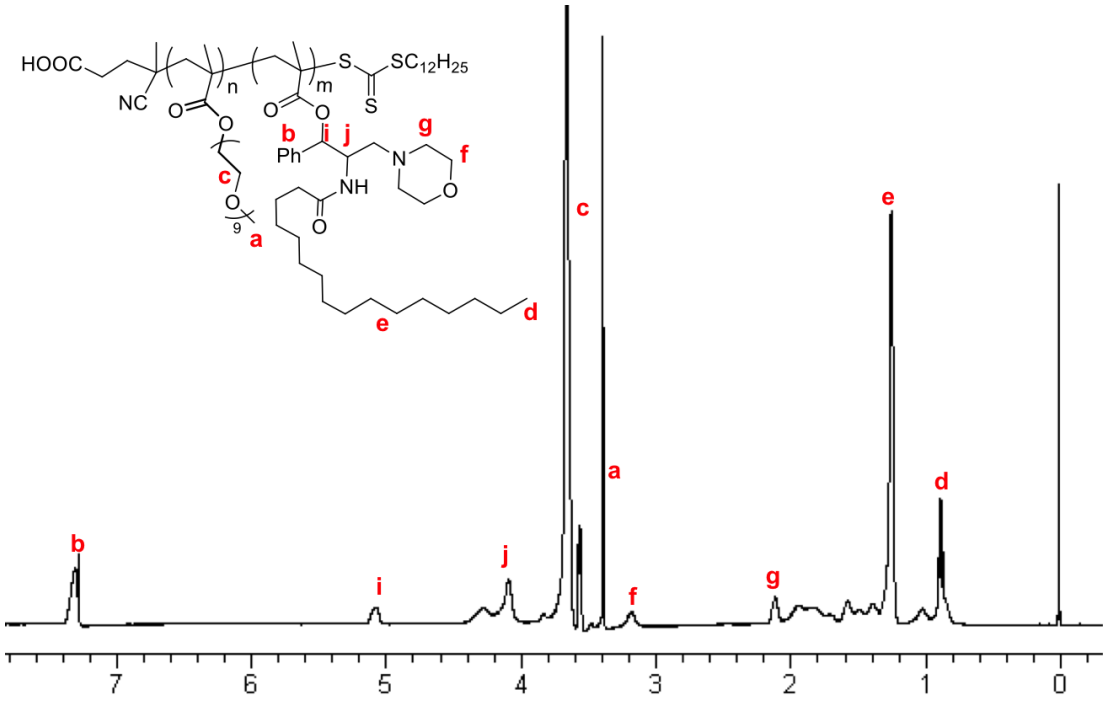

Figure 3-6. ^{1}H-NMR of POEG-*b*-PPPMP polymers in $CDCl_3$.

3.4.4 Biophysical Characterization of Blank and Drug-loaded POEG-*b*-PPPMP micelles

POEG-*b*-PPPMP alone or POEG-*b*-PPPMP/drug mixture readily formed transparent micellar solution in DPBS by a simple film hydration method. Figure 3-7 showed that the CMC of POEG-*b*-PPPMP micelles was around 0.03 mg/mL (2.4 μM). The low CMC of POEG-*b*-PPPMP shall provide a good stability for micelles upon dilution in blood stream after intravenous administration. The hydrodynamic sizes of blank and drug-loaded POEG-*b*-PPPMP micelles were examined by DLS and the data are shown in Figure 3-8. POEG-*b*-PPPMP formed micelles with a diameter of 105 nm (Figure 3-8A). Interestingly, incorporation of a drug into micelles at a carrier/drug ratio of 20:1 (mg/mg) resulted in a slight decrease in particle sizes (80~100 nm) (Figure 3-8B-D). This is likely due to an enhanced interaction between the carrier and loaded drugs, leading to the formation of a more compact structure. TEM images further

confirmed the spherical morphology of blank and drug-loaded POEG-*b*-PPPMP micelles with a uniform size distribution (Figure 3-8). The size, DLC, and formulation stability of drug-loaded POEG-*b*-PPPMP micelles were then examined (Table 3-2). DOX could be loaded into POEG-*b*-PPPMP micelles at a carrier/drug ratio as low as 10/1 (mg/mg), at which ratio DOX was incorporated into the carrier at a DLC of 6.5 % and DOX-loaded micelles were stable with no obvious changes in size or precipitation for 6 days at 4 °C. In addition, with an increase in the carrier/drug ratio, the drug encapsulation efficiency and colloidal stability were further improved. As shown in Table 2, at a carrier/drug ratio of 50:1, DOX-loaded micelles were stable for 42 days in solution at 4 °C. In order to deliver more PPMP as well as provide good stability, a carrier/drug mass ratio of 50:1 was used for all subsequent studies. In addition to DOX, other chemotherapeutic agents such as PTX and C6-ceramide, could be effectively loaded into POEG-*b*-PPPMP nanocarrier. Therefore, POEG-*b*-PPPMP might serve as a carrier for the delivery of different types of anticancer drugs.

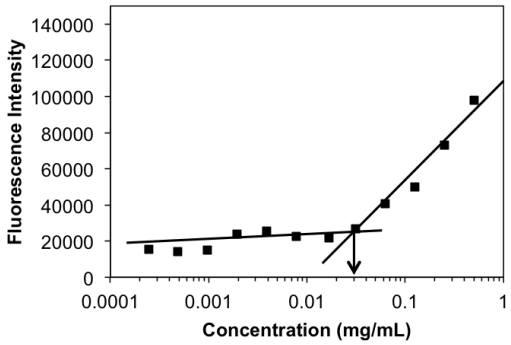

Figure 3-7. Plot of fluorescence intensity at 641 nm versus concentrations of POEG-*b*-PPPMP copolymers.

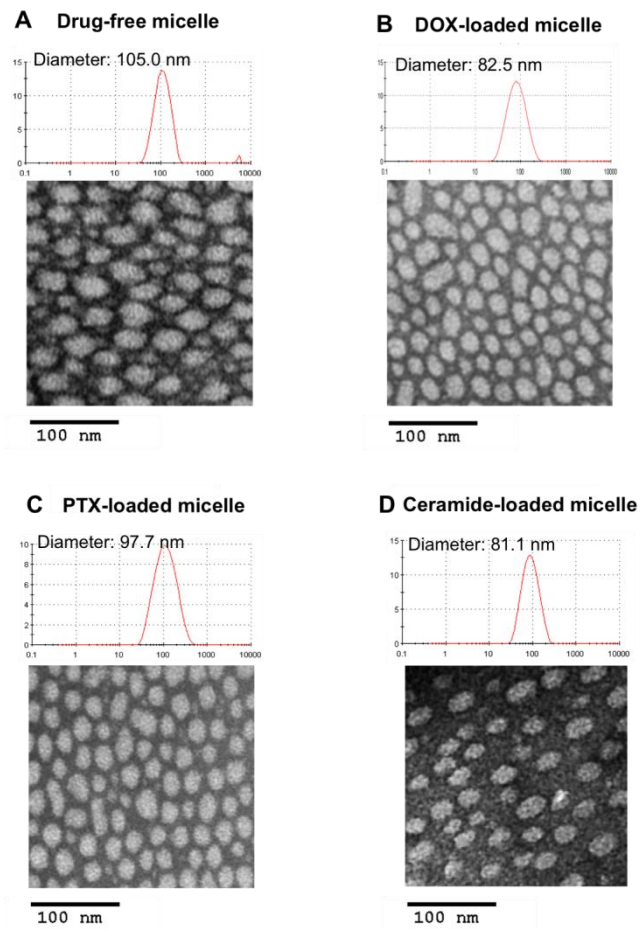

Figure 3-8. TEM images of drug-free POEG-*b*-PPPMP micelles (A), DOX-loaded POEG-*b*-PPPMP micelles (B), PTX-loaded POEG-*b*-PPPMP micelles (C) and ceramide-loaded POEG-*b*-PPPMP micelles (D) using negative staining.

DOX, PTX or ceramide were loaded in to POEG-*b*-PPPMP micelles at carrier/drug ratio of 20/1 (mg/mg). Scale bar is 100 nm.

Table 3-2. Physicochemical Characterizations of DOX-loaded and PTX-loaded POEG-b-PPPMP Micelles.

Micelles	Mass ratio (mg: mg) [a]	Size (nm) [b]	PDI [c]	DLC (%) [d]	DLE (%) [e]	Stability [f] (RT)	Stability [f] (4°C)
$POEG_{15}$-*b*-$PPPMP_7$		105.0	0.179				
$POEG_{15}$-*b*-$PPPMP_7$: DOX	10:1	87.58	0.221	6.5	68.9	48 h	6 d
$POEG_{15}$-*b*-$PPPMP_7$:	20:1	82.46	0.214	3.8	79.7	4 d	25 d

DOX POEG$_{15}$-*b*-PPPMP$_7$:	30:1	79.77	0.196	2.8	86.7	7 d	37 d
DOX POEG$_{15}$-*b*-PPPMP$_7$:	50:1	89.34	0.193	1.9	96.0	12 d	42 d
DOX POEG$_{15}$-*b*-PPPMP$_7$:	10: 1	107.1	0.205	8.2	90.4	24 h	51 h
PTX POEG$_{15}$-*b*-PPPMP$_7$:	20: 1	97.7	0.212	4.4	92.5	45 h	6 d
PTX POEG$_{15}$-*b*-PPPMP$_7$:	30: 1	95.8	0.217	3.1	95.2	53 h	17 d
PTX POEG$_{15}$-*b*-PPPMP$_7$:	50:1	93.2	0.205	1.9	95.6	7 d	21 d
PTX							

a) DOX or PTX concentration in micelles was kept at 0.5 or 1 mg/mL respectively. b) Measured by dynamic light scattering particle sizer. c) PDI = polydispersity index. d) DLC = drug loading capacity. e) DLE = drug loading efficiency. f) Data mean there was no noticeable size change and visible precipitates during the follow-up period.

3.4.5 *In Vitro* Drug Release

The release profile of DOX from DOX-loaded POEG-*b*-PPPMP micelles was investigated by a dialysis method in DPBS and compared to that of free DOX and DOX-loaded POEG-*b*-POM micelles. As shown in Figure 3-9, DOX release from two micellar formulations was significantly slower than that from free DOX. Forty eight percent of DOX was rapidly released from free DOX in 2 h and around 83% of total drug was released within 12 h. In contrast, less than 10% DOX was released from POEG-*b*-PPPMP formulation in 2 h and the slow release kinetics extended for 72 h. The performance of DOX cumulative release followed the order of DOX/POEG-*b*-PPPMP > DOX/POEG-*b*-POM > free DOX.

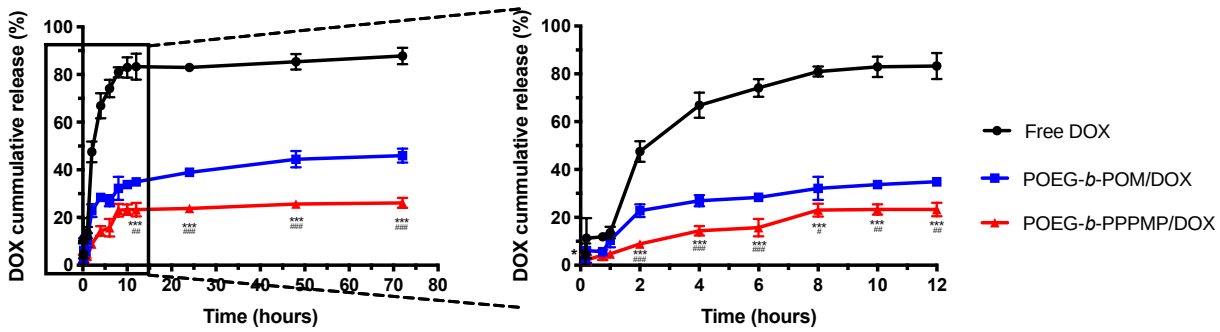

Figure 3-9. Cumulative DOX release profile from POEG-*b*-PPPMP micelles with free DOX and POEG-*b*-POM micelles as control.

DOX concentration was fixed at 0.5 mg/mL. DPBS was used as the release medium. Values reported are the means ± SD for triplicate samples. Statistical significance was determined by two-way ANOVA using the Tukey test for multiple comparisons. *P < 0.05, **P < 0.01, *** P < 0.001 (POEG-*b*-PPPMP/DOX vs free DOX); $^{\#}$P < 0.05, $^{\#\#}$P < 0.01, $^{\#\#\#}$P < 0.001 (POEG-*b*-PPPMP/DOX vs POEG-*b*-POM/DOX).

3.4.6 *In vitro* Cytotoxicity of Prodrug Micelles and PTX/DOX/Ceramide-loaded Micelles

The *in vitro* cytotoxicity of POEG-*b*-PPPMP blank micelles was tested in 4T1.2, PC-3 and MCF-7 cancer cells and compared to that of free PPMP. As shown in Figure 3-10A, free PPMP inhibited the proliferation of 4T1.2 tumor cells in a dose-dependent manner. Compared to free PPMP, POEG-*b*-PPPMP prodrug micelles showed less cytotoxicity at equivalent amounts of PPMP in 4T1.2 cells. Similar results were shown in PC-3 and MCF-7 tumor cells (Figure 3-10B & C). The cytotoxicity of POEG-*b*-PPPMP shall likely come from the PPMP cleaved from the prodrug polymer following the intracellular uptake. The less effectiveness of POEG-*b*-PPPMP was likely due to the limited PPMP cleavage and release in a relatively short period of treatment.

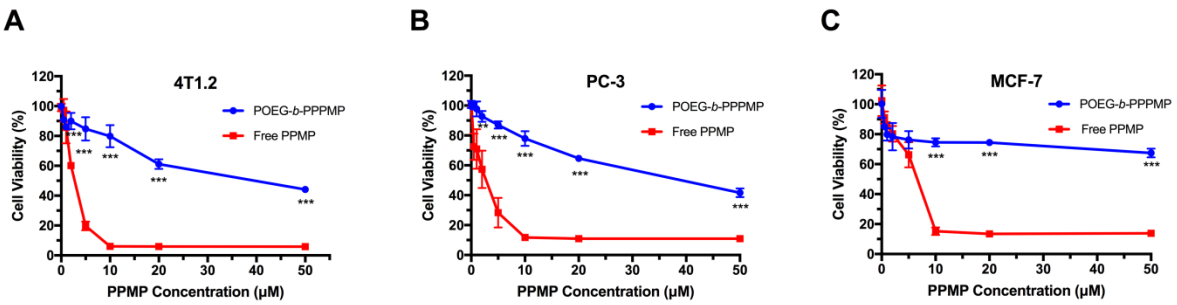

Figure 3-10. Cytotoxicity of POEG-*b*-PPPMP prodrug micelles in 4T1.2 mouse breast cancer cell line (A), PC-3 human prostate cancer cell line (B) and MCF-7 human breast cancer cell line (C) with free PPMP as the control.

Cells were treated with different micelles for 48 h and values reported are the means ± SD for triplicate samples. P values were determined by two-tailed Student's T test. *P < 0.05, **P < 0.01, *** P < 0.001 (POEG-*b*-PPPMP vs PPMP).

The cytotoxicity of DOX-loaded POEG-*b*-PPPMP micelles was also investigated in 4T1.2 (Figure 3-11A), PC-3 (Figure 3-11B) and MCF-7 (Figure 3-11C) cells. DOX-loaded POEG-*b*-POM, DOX·HCl and Doxil were included as controls. At all doses that were used for loading DOX, POEG-*b*-POM showed minimal impact on the proliferation of 4T1.2 cells (Figure 3-11A). POEG-*b*-PPPMP alone showed modest effects on tumor cell proliferation at higher doses. DOX formulated in POEG-*b*-PPPMP was more effective than DOX·HCl and Doxil in inhibiting the proliferation of 4T1.2 cancer cells. More importantly, DOX-loaded POEG-*b*-PPPMP was more potent than DOX-loaded POEG-*b*-POM in inhibiting the proliferation of 4T1.2 cells. The improved cytotoxicity was likely due to the released PPMP from POEG-*b*-PPPMP prodrug copolymer, via the cleavage of the hydrolyzable ester bond by the esterase in tumor cells, resulting in synergistic action with codelivered DOX. A trend of synergistic action between POEG-*b*-PPPMP-based carrier and codelivered DOX was also shown in PC-3 (Figure

3-11B) and MCF-7 (Figure 3-11C) cells. We have further shown a synergy between POEG-*b*-PPPMP and codelivered PTX (Figure 3-11 D-F) or C6-ceramide (Figure 3-11 G-I).

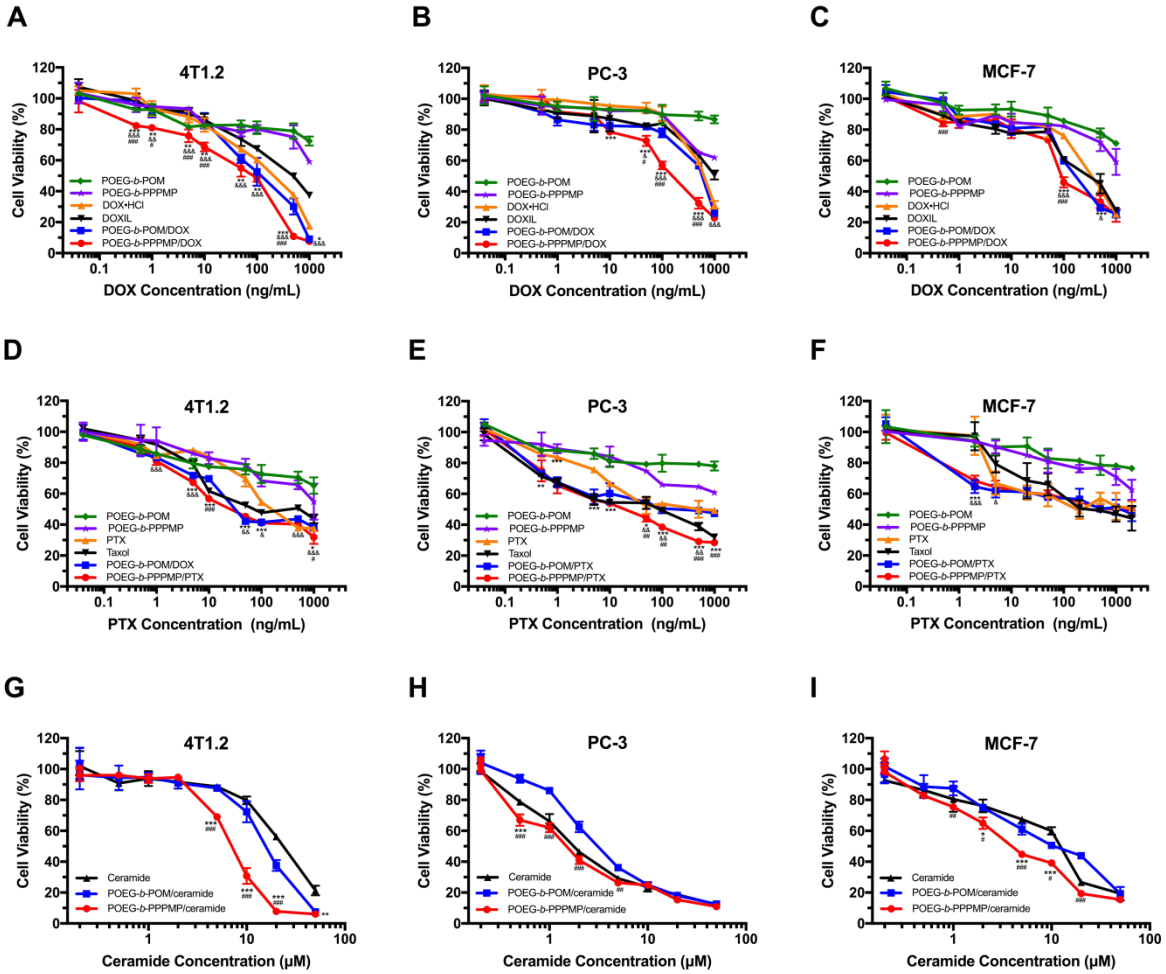

Figure 3-11. Cytotoxicity of DOX-loaded POEG-*b*-PPPMP micelles in 4T1.2 (A), PC-3 (B) and MCF-7 (C) cell lines, PTX-loaded POEG-*b*-PPPMP micelles in 4T1.2 (D), PC-3 (E) and MCF-7 (F) cell lines, and C6-ceramide-loaded POEG-*b*-PPPMP micelles in 4T1.2 (G), PC-3 (H) and MCF-7 (I) cell lines after 48 h treatment.

Data are presented as the means ± SD for triplicate samples. P values were determined by two-way ANOVA using the Tukey test for multiple comparisons. *P < 0.05, **P < 0.01, *** P < 0.001 (POEG-b-PPPMP/DOX vs DOX·HCl, POEG-b-PPPMP/PTX vs PTX, POEG-b-PPPMP/ceramide vs ceramide); &P < 0.05, &P < 0.01, &&&P < 0.001 (POEG-b-PPPMP/DOX vs DOXIL, POEG-b-PPPMP/PTX vs Taxol®); #P < 0.05, ##P < 0.01,

###P < 0.001 (POEG-b-PPPMP/DOX vs POEG-b-POM/DOX, POEG-b-PPPMP/PTX vs POEG-b-POM/PTX), POEG-b-PPPMP/ceramide vs POEG-b-POM/ceramide).

3.4.7 Effect of POEG-*b*-PPPMP on Regulation of Ceramides Production

As a prodrug of PPMP, the ability of POEG-*b*-PPPMP in regulating ceramides production was investigated in 4T1.2 and MCF-7 cells. The peak areas for different sphingolipid subspecies (C16-ceramide, C18-ceramide, C20-ceramide, C22-ceramide and C24-ceramide) were quantified using a non-naturally occurring C6-ceramide as an internal standard and then normalized to protein concentrations. We focused on these species as long-chain ceramides (C16-C20) are known to have anti-proliferative and pro-apoptotic effects[124]. It has been reported that the levels of C16, C24:0 or C24:1 ceramides are significantly increased in breast cancer tissues [125]. Especially, evidence is mounting that the endogenous levels of C16:0 ceramide were increased under pro-apoptotic conditions, which played a decisive role in regulating apoptosis[126-128] As shown in Figure 3-12A & G, treatment with PPMP as well as the POEG-*b*-PPPMP-based prodrug led to a modest increase in the amounts of C16 ceramide. As a ceramide-generating anticancer agent, DOX significantly induced C16 ceramide production in both tested cell lines, while free drug combination (DOX·HCl+PPMP) or POEG-*b*-PPPMP/DOX mixed micelles were most effective in promoting ceramide accumulation. Unlike its effect on C16 ceramide, our POEG-*b*-PPPMP/DOX formulation caused negligible changes in the amounts of C24 ceramides (Figure 3-12 E, F, K & L). Interestingly C24:0 or C24:1 has been reported to have minimal effect in promoting apoptosis and could even promote the proliferation of tumor cells [129, 130]. Therefore, our POEG-*b*-PPPMP/DOX system appears to selectively promote the accumulation of pro-apoptotic ceramide species.

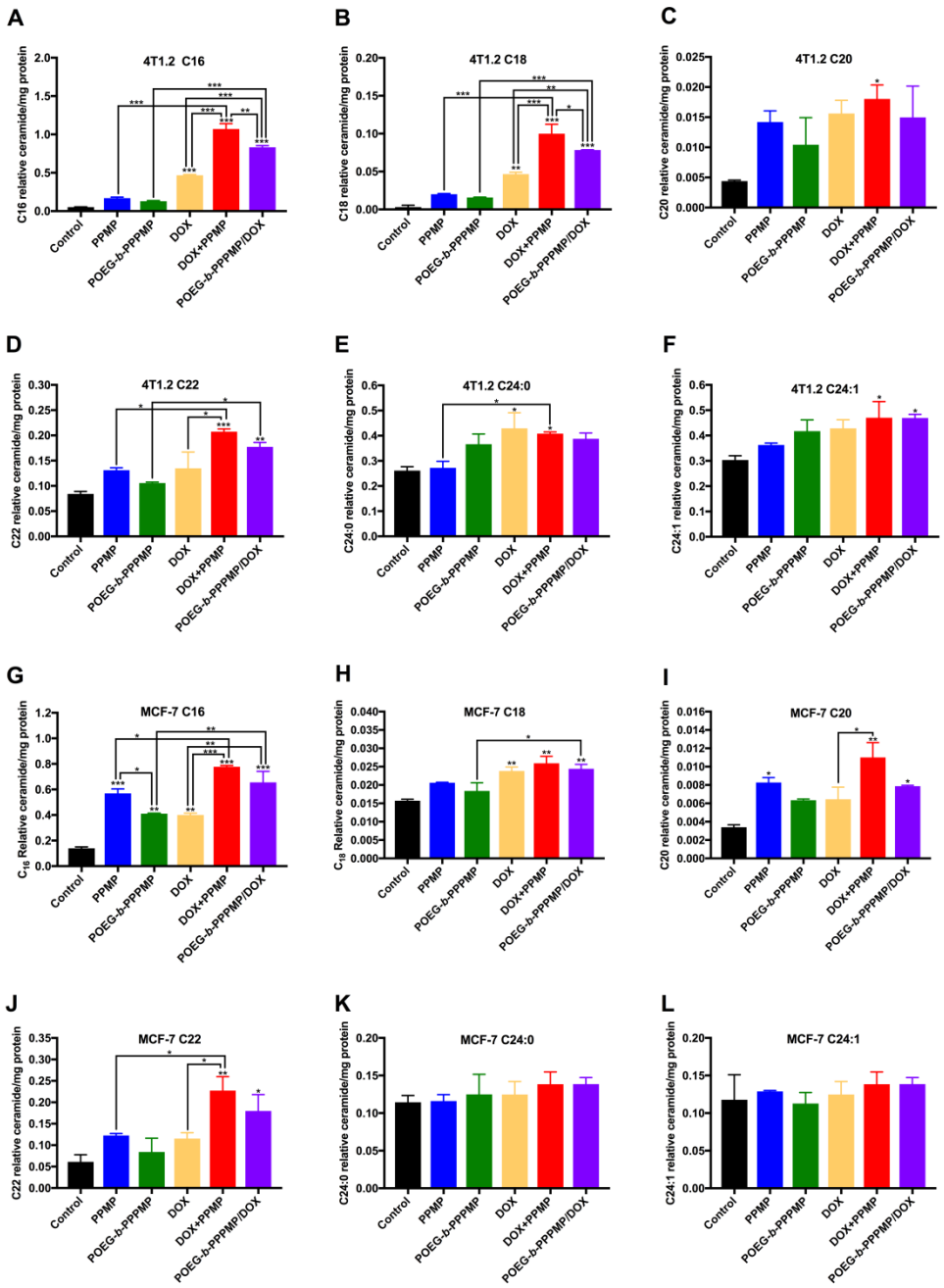

Figure 3-12. Different species of relative ceramide level in 4T1.2 or MCF-7 cells measured by LC/MS 48 h after POEG-*b*-PPPMP or POEG-*b*-PPPMP/DOX treatments compared to free drug alone or combination.

Tumor cells were treated with PPMP, POEG-b-PPPMP, DOX·HCl +PPMP or POEG-b-PPPMP/DOX at the same PPMP concentration of 1.7 μM; DOX·HCl, DOX·HCl +PPMP or POEG-b-PPPMP/DOX at the same DOX concentration of 100 nM. Data are presented as the means ± SD for triplicate samples. P values were generated by one-way ANOVA using the Tukey test for multiple comparisons. *P < 0.05, **P < 0.01, *** P < 0.001.

3.4.8 Effect of POEG-*b*-PPPMP on GCS mRNA Expression

In addition to direct inhibition of GCS enzymatic activity, PPMP has been shown to downregulate the mRNA expression of GCS in tumor cells. PPMP treatment was shown to cause decreases in GCS mRNA levels in drug-resistant cell lines with high endogenous GCS mRNA expression, including head and neck cancer (AMC-HN2, relative resistance to cisplatin) [131] and leukemia cell lines (K562/AO2, multidrug resistance)[132]. Accordingly, we examined the efficacy of POEG-*b*-PPPMP in downregulating GCS mRNA expression in both MCF-7 and 4T1.2 cells and compare to that of free PPMP. As shown in Figure 3-13, treatment with free PPMP led to significant decreases in the basal levels of GCS mRNA in both cancer cell lines. Free PPMP was also effective in inhibiting the DOX-induced upregulation of GCS mRNA expression. POEG-*b*-PPPMP was comparable to free PPMP in inhibiting both basal and DOX-induced expression of GCS mRNA.

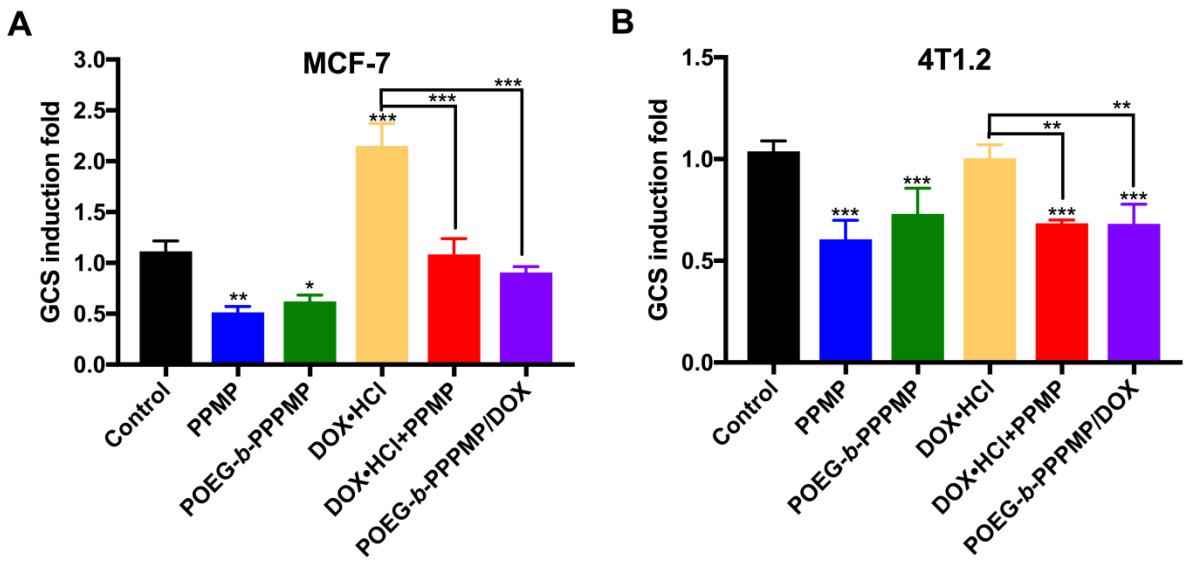

Figure 3-13. Effects of POEG-*b*-PPPMP and POEG-*b*-PPPMP/DOX on GCS mRNA expression in MCF-7 (A) or 4T1.2 (B) cells after 48 h treatment compared to free drug alone or combination.

Tumor cells were treated with PPMP, POEG-b-PPPMP, DOX·HCl+PPMP or POEG-b-PPPMP/DOX at the same PPMP concentration of 1.7 μM; DOX·HCl, DOX·HCl+PPMP or POEG-b-PPPMP/DOX at the same DOX concentration of 100 nM. Data are presented as the means ± SD for triplicate samples. P values were generated by one-way ANOVA using the Tukey test for multiple comparisons. *P < 0.05, **P < 0.01, *** P < 0.001.

3.4.9 Plasma Pharmacokinetics and Tissue Distribution

The POEG-*b*-PPPMP/DOX, POEG-*b*-POM/DOX or DOX·HCl was injected into tumor-free mice at a DOX dose of 5mg/kg. The plasma concentrations of DOX were examined at different time points. The initial blood concentration of POEG-*b*-PPPMP was around 3 mg/mL, which was 100-fold higher than its CMC (0.03 mg/mL). The concentrations of DOX in the blood following i.v. injection of different DOX formulations as a function of time were illustrated in Figure 3-14A. Compared to DOX·HCl, the plasma concentrations of DOX for both POEG-*b*-POM/DOX and POEG-*b*-PPPMP/DOX were significantly higher at early time points and maintained at relatively high levels until 12 h, which is attributed to the surface modification of PEG and stealth-shielding against RES system. With the same length of coated PEG, however, POEG-*b*-PPPMP/DOX provided higher levels of DOX in circulation than POEG-*b*-POM/DOX. This is likely due to a more effective interaction between POEG-*b*-PPPMP and DOX, which is also supported by the data from *in vitro* release study (Figure 3-9).

Next, the DOX tissue distribution of the three formulations was investigated in tumor-bearing mice. POEG-*b*-PPPMP/DOX, POEG-*b*-POM/DOX or DOX·HCl was injected into 4T1.2 tumor-bearing mice at a DOX dose of 5mg/kg. Twenty-four hours following the injection, major organs and tumors were harvested for the quantification of DOX. As shown in Figure

3-14B, compared to free DOX, both micellar formulations exhibited significantly greater amounts of DOX in tumor tissue, which is attributed to the EPR effect of nanoparticles. In addition, DOX formulated in POEG-*b*-PPPMP was more effective in tumor accumulation than in POEG-*b*-POM. This is consistent with the PK data and is likely ascribed to the better stability in blood stream due to the increased carrier-drug interaction between DOX and POEG-*b*-PPPMP. The DOX uptake in other organs was lower for POEG-*b*-PPPMP/DOX compared to free DOX group, although it was not statistically significant. The decreased accumulation of DOX in normal tissues, particularly in heart shall help to decrease the DOX-associated toxicity and allow higher doses of DOX to be administered to maximize the therapeutic effect.

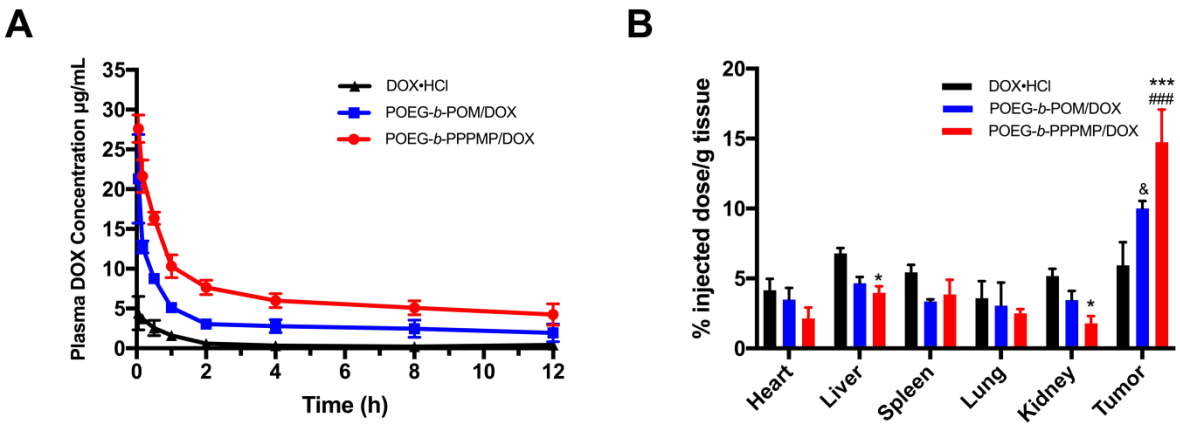

Figure 3-14. Pharmacokenetics and biodistribution POEG-*b*-PPPMP/DOX micelles in 4T1.2 breast tumor model.

(A) Pharmacokinetics of DOX·HCl, POEG-*b*-POM/DOX and POEG-*b*-PPPMP/DOX micelles in tumor-free female BALB/c mice. (B) Tissue distribution of DOX 24 h post injection in tumor-bearing female BALB/c mice treated with DOX·HCl, POEG-*b*-POM/DOX or POEG-*b*-PPPMP/DOX micelles at the same dose of 5mg DOX/kg. Values reported are the means ± SEM, n=5. P values were generated by two-way ANOVA using the Tukey test for multiple comparisons. *P < 0.05, *** P < 0.001 (POEG-*b*-PPPMP/DOX vs DOX·HCl; $^{\&}$P < 0.05 (POEG-*b*-POM/DOX vs DOX·HCl); $^{\#\#\#}$P < 0.001 (POEG-*b*-PPPMP/DOX vs POEG-*b*-POM/DOX).

Table 3-3. Pharmacokinetic Parameters of DOX in Different Formulations.

Groups	$T_{1/2}$(h)	$AUC_{0-\infty}$ (μg/ml*h)	Cmax (μg/mL)	CL (mL/h)	Vd (mL)
DOX.HCl	3.35	9.20	4.41	10.87	52.49
POEG-*b*-POM/DOX	15.96	84.31	21.30	1.19	27.31
POEG-*b*-PPPMP/DOX	16.19	180.16	27.60	0.56	12.97

3.4.10 *In Vivo* Therapeutic Study

The *in vivo* tumor growth inhibition efficiency of POEG-*b*-PPPMP/DOX micelles was investigated in a highly aggressive syngeneic murine breast cancer model (4T1.2, s.c. at mammary fat pad). As expected, the control carrier alone (POEG-*b*-POM) showed minimal antitumor activity (Figure 3-15A). POEG-*b*-PPPMP alone exhibited a modest but significant ($P<0.05$) tumor inhibition effect. Doxil formulation and POEG-*b*-POM/DOX showed comparable and enhanced tumor inhibitory effect. Among all treatment groups, POEG-*b*-PPPMP/DOX was most effective in inhibiting the tumor growth. Figure 3-15 B&D show the weights and images of tumor tissues that were collected at the end of the experiment, which was consistent with data of tumor growth curves (Figure 3-15A). There were slight increases in body weights in all groups over the period of study, suggesting the negligible toxicity of POEG-*b*-PPPMP/DOX micelles *in vivo* (Figure 3-15C).

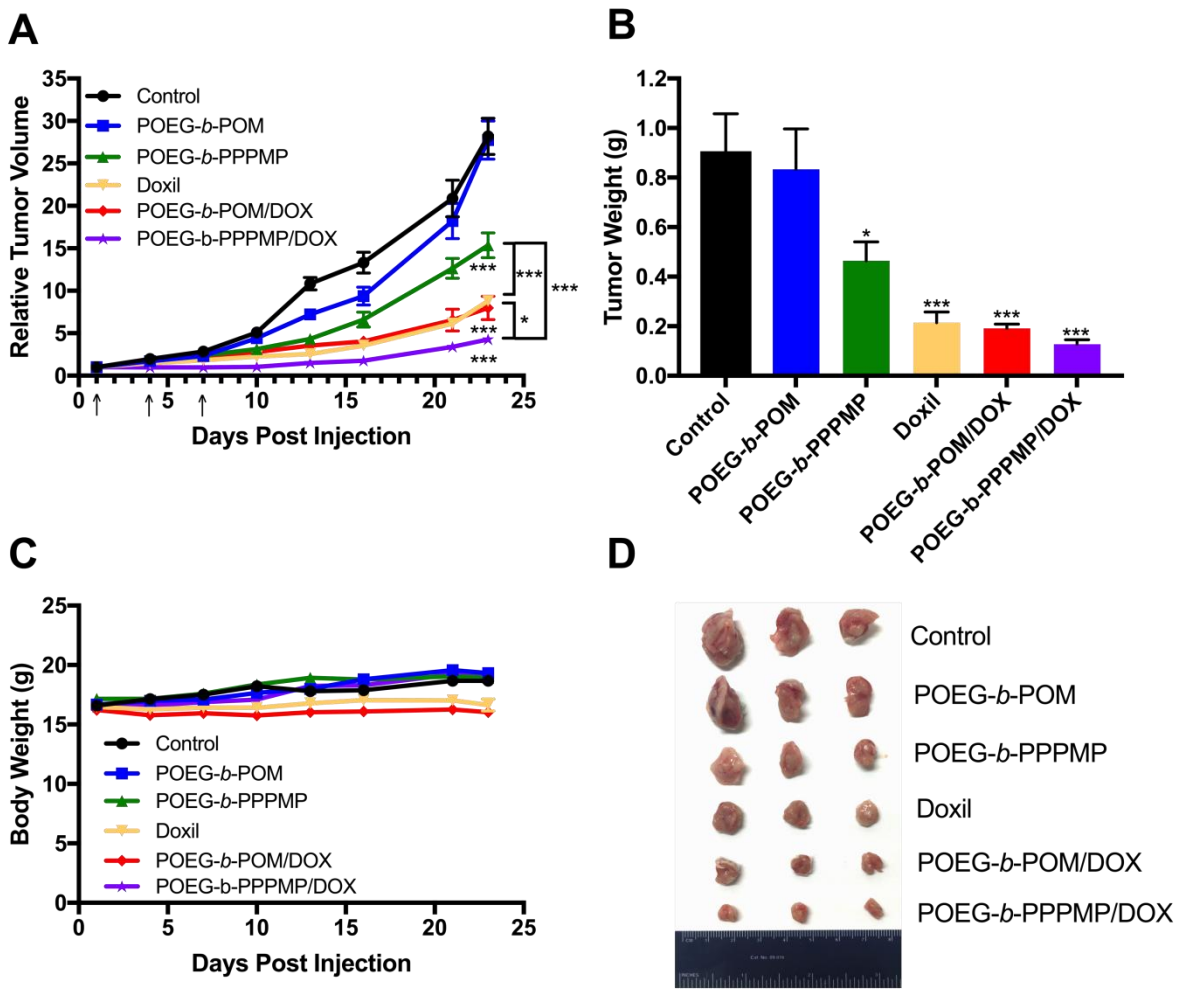

Figure 3-15. Antitumor activity of blank POEG-*b*-POM, blank POEG-*b*-PPPMP micelles, Doxil, DOX loaded POEG-*b*-POM and DOX loaded POEG-*b*-PPPMP micelles in a syngeneic murine breast cancer model (4T1.2).

Three injections were given on day 1, 4 and 7. (B) Weights of tumors collected from different groups at the end of experiment. (C) Changes of body weight in mice receiving different treatments. (D) Photographs of tumors collected from different treatment groups at the end of experiment. Values reported are the means ± SEM, n = 5. P values were generated by one-way ANOVA using the Tukey test for multiple comparisons. *P < 0.05, **P < 0.01, ***P < 0.001 (vs control).

3.4.11 Histochemical Staining

Histological analysis was conducted to further evaluate the therapeutic effect of POEG-*b*-PPPMP/DOX formulation. As shown in Figure 3-16, tumors treated with DPBS or POEG-*b*-POM carrier alone exhibited abundant aggregates of neoplastic cells with conspicuous nucleoli and scant cytoplasm due to high proliferation rate. In contrast, tumors that were treated with POEG-*b*-PPPMP/DOX showed significantly altered morphology with shrunken nuclei and the lowest tumor cell density.

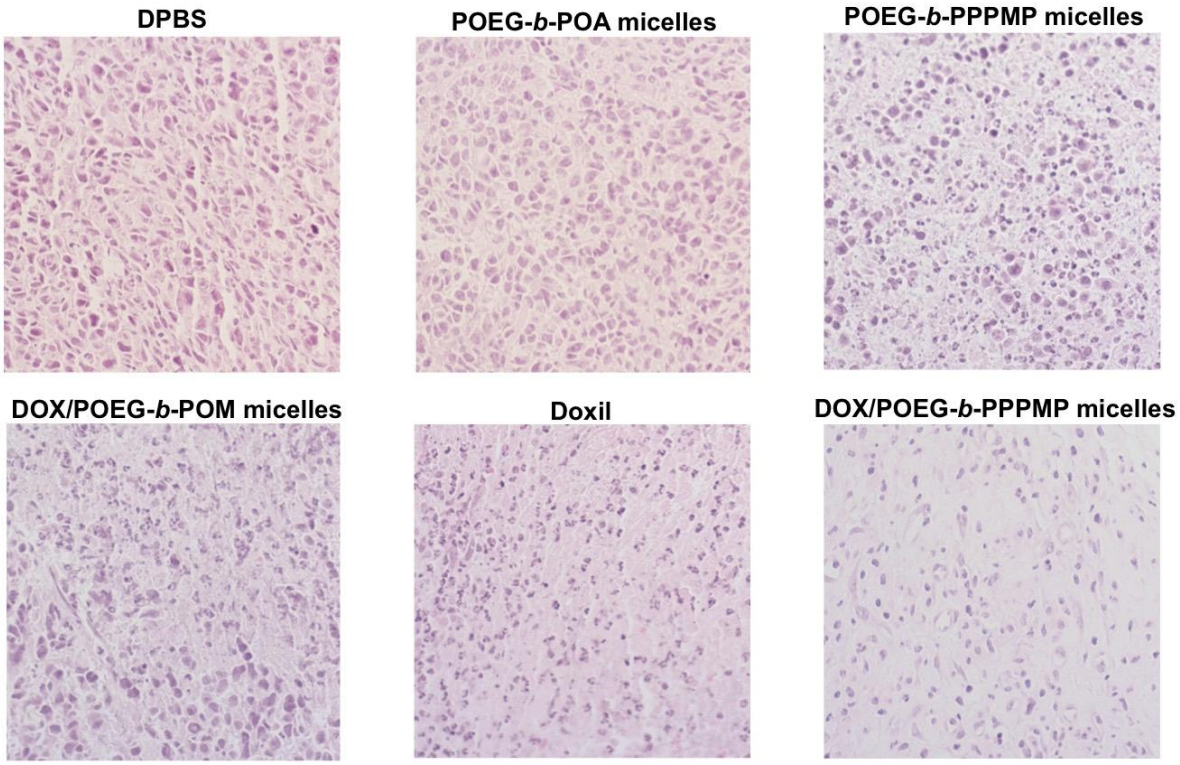

Figure 3-16. Histological analyses of tumor tissues collected from different groups at the end of *in vivo* therapeutic experiment using H&E staining.

3.5 Discussion

As a primary approach in cancer treatment, various classes of chemotherapeutic drugs are available in clinic. Regardless of the differences in the structures of the agents, their molecular targets, and the major mechanisms of action, the eventual onset of apoptosis seems to be a common consequence in chemotherapy-induced cell death. Ceramide, the central molecule in sphingolipids family, has recently been identified as a key mediator of this process and has attracted tremendous attention in cancer therapy[133]. Mounting evidence shows that most chemotherapeutic agents are capable of inducing endogenous ceramide accumulation through either activation of sphingomyelin catabolism and/or increases in *de novo* synthesis[91].

Various strategies have been developed to increase the intracellular levels of ceramides in tumor cells including intracellular delivery of exogenous ceramides, enhancement of ceramide synthesis, and inhibition of ceramide catabolism[99]. As a stand-alone strategy, the first two approaches are insufficient as the increased levels of ceramides are only short-lived due to activation of the ceramide catabolism pathways[91]. Importantly, many of the ceramide metabolites have the opposite effects of ceramides, playing an important role in tumor cell survival and drug resistance[112, 134, 135].

A number of pathways are involved in the catabolism of ceramides inside cells with GCS being the dominant mechanism for ceramide catabolism[136]. Drugs that cause increases in the intracellular levels of ceramides such as DOX, PTX and C6-ceramide itself, also induce upregulation of GCS expression. However, different types of tumor cells respond differently to a ceramide-generating drug (e.g., DOX) with respect to the extent of GCS upregulation. Our data

(Figure 3-1) show that GCS upregulation was much more dramatic in MCF-7 cells than in 4T1.2 cells following treatment of DOX, PTX or C6-ceramide. Nonetheless, combination of a ceramide-generating drug with an inhibitor of GCS shall represent an effective strategy to improve the therapeutic outcome.

PPMP is a small molecule drug that was initially known to inhibit the enzymatic activity of GCS. PPMP was later shown to be also effective in downregulating the mRNA expression levels of GCS in tumor cells (Figure 3-13). Our data show that PPMP effectively downregulated both basal and DOX-induced GCS mRNA levels in MCF-7 and 4T1.2 cells, which is consistent with what was found in other tumor cells [42,43]. Interestingly, PPMP appears to selectively upregulate the proapoptotic ceramide species while having minimal impact on those species that have no effect in promoting the apoptosis or even enhance the tumor cell proliferation (Figure 3-12). The underlying mechanism is unclear and requires more studies in the future.

As a strategy to faciliate the codelivery of PPMP and another ceramide-genertaiung anticancer agent, we initially developed a dual-functional carreir that is based on PEG-$PPMP_2$. One issue with this system is the low number (2) of PPMP units in the carrier, which will limit the amounts of PPMP that can be delivered to tumor tissues. This led us to the developemnt of an improved nanocarrier, which is a POEG-*b*-PPPMP-based copolymer with significantly increased number of PPMP units (7) in each molecule of polymer. A PPMP monomer was first synthesized, which allows the use of a simple and well-controlled polymerization protocol to obtain well-defined POEG-*b*-PPPMP polymers. This approach has an obvious advantage of simplicity compared to the strategy of post-conjugation of PPMP following the synthesis of a

polymer scaffold. It also avoids the issue of the presence of some remaining reactive groups in polymers after conjugation of PPMP. After synthesis, the formulation of blank or drug-loaded POEG-*b*-PPPMP could be prepared through a very simple film hydration method. In addition, POEG-*b*-PPPMP was effective in formulating a wide range of hydrophobic anticancer drugs of different structures.

POEG-*b*-PPPMP well retains the pharmacological activity of free PPMP. POEG-*b*-PPPMP exhibited comparable activity in downregulation of basal GCS mRNA expression (Figure 3-13), and similarly reversed the DOX-induced GCS upregulation as free PPMP (Figure 3-13). More importantly, like free PPMP, POEG-*b*-PPPMP also selectively increased the accumulation of pro-apoptotic ceramides with negligible effect on anti-apoptotic ceramides species.

POEG-*b*-POM was synthesized as a control carrier that has the same units of hydrophilic POEG and hydrophobic oleic acid (POEG15-*b*-POM_7) compared to POEG-*b*-POM. Interestingly, DOX formulated in POEG-*b*-POM showed a relatively slower kinetics of drug release (Figure 3-9), longer stay in blood (Figure 3-14A), and more effective accumulation at tumor tissues (Figure 3-14B) compared to DOX formulated in the control carrier. This is likely due to a more effective interaction between POEG-*b*-PPPMP and DOX. In addition to hydrophobic interaction as seen with POEG-*b*-POM/DOX, the aromatic rings of PPMPs in POEG-*b*-PPPMP further interact with DOX through π-π stacking, resulting in an enhancement in the overall carrier/drug interactions.

POEG-*b*-PPPMP demonstrated significant antitumor activity both *in vitro* and *in vivo*. This is likely due to the release of active PPMP following delivery of POEG-*b*-PPPMP to tumor cells. Importantly, codelivery of DOX via POEG-*b*-PPPMP led to effective growth inhibition of 4T1.2 breast tumor, much more effectively than Doxil and POEG-*b*-PPPMP/DOX. The improved antitumor activity of POEG-*b*-PPPMP/DOX over POEG-*b*-POM /DOX might be largely attributed to the synergistic action between the released PPMP from POEG-*b*-PPPMP and the codelivered DOX. The improved delivery of DOX via POEG-*b*-PPPMP-based carrier (Figure 3-14) may also play a role.

In summary, we have developed a well-characterized POEG-*b*-PPPMP prodrug-based micellar nanocarrier that consists of 7 units of PPMP and 15 units of POEG for efficient delivery of water insoluble anticancer drugs. POEG-*b*-PPPMP well retained the biological ability of PPMP. DOX loaded in POEG-*b*-PPPMP micelles exhibited slow release kinetics *in vitro* as well as a sustained PK profile in mice. Combination of DOX with POEG-*b*-PPPMP led to inhibition of DOX-induced upregulation of GCS, increased accumulation of pro-apoptotic ceramides, and enhanced cytotoxicity towards tumor cells. More importantly, systemic administration of DOX formulated in POEG-*b*-PPPMP micelles resulted in significant inhibition of 4T1.2 breast tumor, much more effectively than Doxil and POEG-*b*-POM /DOX.

4.0 Pendant HDAC Inhibitor SAHA Derivatized Polymer as a Novel Prodrug Micellar Carrier for Anticancer Drugs

4.1 Abstract

Suberoylanilide hydroxamic acid (SAHA), a histone deacetylase inhibitor (HDACI) approved by FDA for the treatment of cutaneous T cell lymphoma, is a promising anticancer drug for various cancers with a unique mode of action. However, it demonstrates limited clinical benefits in solid tumors as a single drug. In order to achieve enhanced and synergistic co-delivery of SAHA and Doxorubicin (DOX), a cleavable SAHA-based prodrug polymer (POEG-*b*-PSAHA), consisting of hydrophilic poly(oligo(ethylene glycol) methacrylate) (POEG) blocks and hydrophobic SAHA segments, has been developed. POEG-*b*-PSAHA prodrug polymer was able to form spherical micelles with a diameter around 60 nm, and well retained the pharmacological activity of SAHA in either inhibiting the proliferation of tumor cells or inducing histone acetylation. DOX formulated in POEG-*b*-PSAHA-based micelles showed a sustained release profile. DOX-loaded POEG-*b*-PSAHA exhibited more potent cytotoxicity towards tumor cells than free DOX and DOX loaded in a pharmacologically "inert" nanocarrier, POEG-*b*-POM. Consistently, DOX/POEG-*b*-PSAHA formulation resulted in an improved therapeutic effect *in vivo* compared to free DOX, Doxil, or DOX formulated in POEG-*b*-POM micelles. These results suggest that SAHA-based prodrug micelles may serve as a dual functional carrier for combination strategies in epigenetic-oriented anticancer therapy.

4.2 Background

Cancer development and progression is not only confined to genetic changes, but also involves epigenetic changes, leading to alterations in gene expression and cell phenotypes. Epigenetics is concerned with the heritable phenotypes based on changes in chromosome, as opposed to genetics, whose realm is on the basis of alterations in the primary DNA sequence [137, 138]. Alterations in the structure and modification status of chromatin represent powerful regulatory mechanisms for gene expression and genome stability [137]. The major epigenetic modifications in mammals, and particularly in humans, are DNA methylation and post-translational histone modifications (acetylation, methylation, phosphorylation etc.) [139]. In the context of histone modifications, the acetylation status of histones plays a crucial role in regulating gene expression by affecting the accessibility of DNA around them [140]. Acetylation levels are controlled by the balance of two enzymes families: histone acetyltransferase (HAT) and histone deacetylase (HDAC). HAT facilitates the acetylation of lysine in histone tails, which is associated with a more relaxed chromatin state, opening up access for transcription factors and polymerases, and therefore gene-transcription activation. In contrast, HDACs deacetylate the lysine residues thereby promoting a more condensed chromatin state and hence leading to transcriptional gene silencing [141, 142]. Specially, the removal of the acetyl groups by HDACs also exposes the protonated amino groups of lysine units of histones, thereby increasing ionic interactions between the positively charged histones and negatively charged phosphate backbone of DNA, which yields a more compact chromatin structure and represses gene transcription by limiting the accessibility of the transcription machinery [142].

A growing body of evidence indicates that the silence of tumor suppressor genes caused by HDAC overexpression could be a common phenomenon in tumor onset and progression [143-145]. Therefore, there is growing interest in the development of HDAC inhibitors (HDACi) as anticancer agents and a large number of studies demonstrated the potential of HDACi in different cancer cell lines and in animal models of tumors [146-148]. The oral drug Vorinostat, also known as SAHA (from suberoylanilide hydroxamic acid) was the first HDAC inhibitor approved by the U.S. FDA in 2006 for the treatment of cutaneous T cell lymphoma in patients who have progressive, persistent or recurrent disease or following failure of two systemic therapies. It was also approved for multiple myeloma with slight advantage over Velcade®. SAHA is a pan-HDAC inhibitor and inhibits both classes I and II enzymes but does not inhibit HDACs belonging to class III [146, 149]. SAHA acts as a micromolar inhibitor of HDACs by chelating the zinc atoms in HDAC catalytic sites via its hydroxamic end, with the phenyl ring protruding out of the binding pocket and lying on the hydrophobic surface of HDAC [150]. SAHA blocks the proliferation of cultured tumor cells and suppresses tumor growth in a variety of tumor models including prostate cancer [151], breast cancer [152], leukemia [153], glioma [154] and lung cancer [155] with little or no toxicity.

Although SAHA has significant anticancer activity as a monotherapy in hematological malignancies, it demonstrates limited clinical benefit for patients with solid tumors, prompting the investigation of novel combination treatments with existing neoplastic interventions [156]. Besides, the acceptable toxicity profile of SAHA permits a broad integration into currently approved chemotherapy regimens [157-159]. Based on a mechanistic rationale, SAHA has been shown to be additive or synergistic with a wide array of anticancer drugs, including conventional

chemotherapeutics (doxorubicin, paclitaxel, cisplatin, gemcitabine, 5-fluorouracil and etoposide) [160-163], targeted agents (imatinib, bevacizumab and trastuzumab) [164, 165] and transcriptional modulators (all-trans retinoic acid and the demethylating agent 5-aza-2′-deoxycytidine) [166]. One of the most significant combinations is with DNA damage-inducing therapies, which occurs, in part, through a SAHA-mediated increase in chromatin accessibility and downregulation of DNA repair [156]. Doxorubicin induces DNA strand breaks by binding to DNA, stabilizing the Topo II-DNA complex, and inhibiting the re-ligation of DNA strands during replication [167]. SAHA potentiates DOX-induced Topo II-mediated DNA damage, growth inhibition and cell death through the chromatin decondensation, facilitating the access of topo II inhibitors to their DNA substrate [158, 159]. Moreover, the synergy is further intensified by the effect of SAHA on the expression, regulation and activation of a variety of DNA repair and DNA damage response genes, like Ku70 [168].

Although the combination of SAHA and other anticancer agents helps, to some extent, achieve better treatment of cancer, the triumph of simple physical mixture of multiple drugs is largely hindered as a result of poor solubility, minimal distribution to tumor tissue, and suboptimal dose ratio [169]. Carrier-mediated combination therapy could offer some advantages to overcome the above challenges, including improved solubility and bioavailability of each drug, increased accumulation at tumor sites through EPR effect, synchronized and controlled pharmacokinetics of each drug and ratiometric dosing, that is, the ability to tailor the relative ratios of each agent based on its pharmacological disposition [170].

Among the commonly used drug delivery systems, polymers with diverse structures have been widely selected as the nanocarriers for hydrophobic anticancer drugs, including SAHA, DOX, and others. Several nanoscopic formulations of SAHA have been developed for parenteral administrations to improve the solubility and overall disposition profile. For example, PEG-b-PLA block copolymer-based micelles have been employed as a carrier to encapsulate SAHA, and it was found that SAHA loaded in micelles provided sustained exposure and improved pharmacokinetics characterized by a significant increase in serum $t_{1/2}$, AUC and mean residence time [171]. However, the use of a large amount of pharmacologically inert carriers may not only add to the cost but also imposes safety issue [172]. Prodrug polymer nanocarriers represent an effective strategy to reduce the amount of inert materials. More importantly, amphiphilic prodrug polymers self-assemble in aqueous solution and serve as dual-functional carriers to achieve the additive or synergistic effect with co-delivered anticancer drugs.

In this study, we designed and synthesized SAHA-based prodrug polymer, denoted as POEG-*b*-PSAHA. These amphiphilic polymers could self-assemble into prodrug micelles and serve as nanocarriers for DOX delivery. The size and structure of POEG-*b*-PSAHA were characterized. Moreover, the *in vitro* pharmacological activity of POEG-*b*-PSAHA prodrug micelles was examined and compared with free SAHA. Finally, the antitumor activity of DOX-loaded POEG-*b*-PSAHA micelles was investigated in a syngeneic breast cancer model.

4.3 Experiment Procedures

4.3.1 Materials

Aniline, N,N′-dicyclohexylcarbodiimide, 4-(dimethylamino)pyridine, hydroxylamine hydrochloride, 1-hydroxybenzotriazole hydrate, potassium carbonate, potassium hydroxide, vinylbenzyl chloride, 4-cyano-4-[(dodecylsulfanylthiocarbonyl)sulfanyl]pentanoic acid, oligo(ethylene glycol) methacrylate OEGMA (average Mn = 500), 2,2-Azobis(isobutyronitrile) (AIBN), trypsin-EDTA solution, 3-(4,5-dimethylthiazol-2-yl)-2,5-diphenyl tetrazolium bromide (MTT) and Dulbecco's Modified Eagle's Medium (DMEM) were all purchased from Sigma-Aldrich (MO, USA). AIBN was purified by recrystallization in anhydrous ethanol. Monomethyl suberate was purchased from TCI (OR, USA). DOX.HCl was purchased from LC Laboratories (MA, USA). Fetal bovine serum (FBS) and penicillin-streptomycin solution were purchased from Invitrogen (NY, USA.). Cell culture and animals were similarly handled as described before [55].

4.3.2 Synthesis of SAHA-monomer

SAHA was synthesized following a published method [173].

Vinylbenzyl chloride (1.0 g, 6.6 mmol), succinic acid (7.7 g, 66.0 mmol, 10 equiv) and K_2CO_3 (4.5 g, 32.8 mmol, 5 equiv) were dissolved in 30 mL DMF and immersed into an oil bath at 90 °C. After 4 h, the mixture was filtered through cottons to remove excess amount of salt. The reaction was quenched by addition of excess amount of pure water and centrifuged to remove DMF. The precipitate was dissolved in DCM, and the crude product was purified by

column chromatography on silica gel eluted with ethanol/DCM (v/v, 1: 9) to give the Compound 1 (1.4 mg, 91%).

For the synthesis of SAHA-monomer, CDI (69 mg, 0.43 mmol, 1.2 equiv) was added in portions to a stirred solution of Compound 1 (100 mg, 0.43 mmol, 1.2 equiv) in DCM. After stirring for 10 min, the reaction mixture turned into light yellow color. TLC showed that the intermediate was formed, and then SAHA (94 mg, 0.36 mmol) was added to the mixture in portions. After 2 h, the reaction was complete as confirmed by TLC, and the reaction was quenched by the addition of the saturated sodium bicarbonate. The aqueous layer was extracted with DCM, washed with brine, and dried over $MgSO_4$. The crude product was chromatographed on silica gel (ethyl acetate/hexane =2:1) to give SAHA monomer (125 mg, 69%).

4.3.3 Synthesis of POEG macroCTA

POEG macroCTA was synthesized and purified following a published literature [43].

4.3.4 Synthesis of POEG-*b*-PSAHA

POEG macroCTA (150 mg, 0.02 mmol), SAHA-monomer (125 mg, 0.26 mmol, 13 equiv), AIBN (1 mg, 0.0061 mmol, 0.3 equiv) and 2 mL dried 1, 4-Dioxane were added into an Schlenk tube and deoxygenated by free-pump-thawing for three times. The mixture was then protected under N_2 and immersed into an oil bath at 90 °C. After 24 h, the reaction was quenched by immersing the tube into liquid nitrogen. The mixture was purified through three cycles of dissolution/precipitation in DCM/hexane and dried in vacuum to afford POEG-*b*-PSAHA (260mg, 96%).

4.3.5 Preparation and Characterization of DOX-loaded POEG-*b*-PSAHA Micelles

The blank or DOX-loaded POEG-*b*-PSAHA micelles were prepared through the film hydration method. First, DOX.HCl was neutralized with 3 equivalents of triethylamine in a mixture of DCM/methanol (1:1, v/v). DOX (5 mg/mL) was then mixed with POEG-*b*-PSAHA (50 mg/mL in DCM) at various carrier/drug weight ratios. After removing the solvent by nitrogen flow, the thin film was formed, which was further dried under vacuum for 2 h to remove any trace of remaining solvent. Then the thin film was hydrated with PBS followed by vortexing. The blank micelles were similarly prepared. The average diameter and the size distribution of micelles were examined via a Zetasizer (DLS). The morphology of blank or DOX-loaded POEG-*b*-PSAHA micelles was observed using transmission electron microscopy (TEM).

The drug loading efficiency of DOX was examined by Waters Alliance 2695 Separations Module combined with Waters 2475 Fluorescence Detector (excitation, 490 nm; emission, 590 nm; gain, 3; sensitivity (FUFS), 10 000) and high performance liquid chromatography (HPLC) respectively as described in previous publications [56]. Drug loading capacity (DLC) and drug loading efficiency (DLE) were calculated according to the following equation: DLC %= [weight of drug loaded/(weight of polymer used + weight of drug used)]×100%, DLE %= (weight of loaded drug/weight of input drug)×100 %. The colloidal stability of drug-loaded micelles with various carrier/drug molar ratios at 4°C was evaluated by following the changes in sizes of the particles or visible precipitates every hour in the first 12 h and daily after 12 h following sample preparation.

The CMC of POEG-*b*-PSAHA was measured by fluorescence spectrometry using nile red as a fluorescence probe. Briefly, thirty microliters of nile red (0.05 mg/mL in DCM) were added to each tube and the solvent was removed by nitrogen flow. POEG-*b*-PSAHA micelles ranging from 6.1×10^{-5} to 5×10^{-1} mg/mL were prepared with serial dilution as described above and then added into the tubes with nile red. The final concentration of nile red was kept at 6.0×10^{-7} M. The micelles were vortexed and kept overnight at room temperature to reach the equilibrium of solubilization. The samples were excited at an excitation wavelength of 550 nm and fluorescence intensities were recorded at an emission spectrum from 600 to 700 nm. The peak intensities at 647 nm were plotted versus polymer concentrations. The CMC value was calculated as the cross-point where a sharp increase in fluorescence intensity was observed.

The *in vitro* release of DOX from DOX-loaded POEG-*b*-PSAHA micelles was examined using a dialysis method. Briefly, two hundred and fifty microliters of DOX/POEG-*b*-PSAHA micelles or free DOX·HCl (0.5 mg DOX/mL) were transferred to clamped dialysis bags (MWCO 3500 Da) in triplicate and incubated in 50 mL PBS as release medium, with gentle shaking at 100 rpm at 37 °C. One milliliter of medium was withdraw and same volume of fresh medium was supplemented at 10 min, 0.5, 1, 2, 4, 6, 8, 10, 12, 24, 48 and 72 h. DOX release from micelles was measured by fluorescence spectrometry at the excitation wavelength of 480 nm and emission wavelength of 590 nm by Synergy H1 Hybrid Multi-Mode Microplate Reader (Winooski, VT).

4.3.6 *In vitro* Cytotoxicity Assay

Cytotoxicity assay was performed with 4T1.2 mouse breast cancer cells, MCF-7 human breast cancer cells, and HCT-116 human colon cancer cells. 4T1.2 (1×10^3 cells/well), MCF-7 (5×10^3 cells/well), or HCT-116 (2×10^3 cells/well) cells were seeded in 96-well plates followed by 24 h of incubation in DMEM with 10% FBS and 1% streptomycin/penicillin. To evaluate the combinational effect of SAHA with other anticancer drugs, various concentrations of free SAHA, free DOX·HCl, or the combination of both were added in triplicate to cells and incubated for 48 h. To study the cytotoxicity of blank POEG-*b*-PSAHA micelles, cells were challenged with various concentrations of POEG-*b*-PSAHA micelles or free SAHA (in DMSO) at equivalent SAHA concentrations for 48 h. The cytotoxicity of DOX-loaded POEG-*b*-PSAHA micelles was also examined, in comparison to DOX.HCl and DOX loaded in a biologically inert polymer POEG-*b*-POM. Cells were treated with different DOX formulations of varied concentrations. Blank POEG-*b*-PSAHA or POEG-*b*-POM at concentrations equivalent to those of carriers in the corresponding DOX formulation groups, was also added into cells. Cells were incubated for 48 h and cell viability was determined by MTT assay. Briefly, ten microliters of 3-(4, 5-dimethylthiazol-2-yl)-2,5-diphenyltetrazoliumbromide (MTT) (5mg/mL in PBS) were added to cells. Following incubation for 4 h, the medium was removed and MTT formazan was solubilized by DMSO. The absorbance was measured by a microplate reader with wavelength at 590 nm and reference wavelength at 620 nm. Untreated cells were used as a control. Cell viability was calculated as $[(OD_{treat} - OD_{blank})/(OD_{control} - OD_{blank})\times100\%]$.

4.3.7 Western Blot

Western immunoblotting was conducted with 4T1.2 cells. Cells were treated with 0.1% DMSO (control) or indicated concentrations (1 μM or 5 μM) of SAHA or POEG-*b*-PSAHA, respectively. After 24 h treatment, cells were rinsed twice with ice-cold PBS and lysed by RIPA buffer. The lysates were centrifuged at 12,500 rpm for 10 min. Samples with equal amounts of total cellular proteins were subjected to sodium dodecylsulfate polyacryl amide gel electrophoresis (SDS-PAGE), followed by transferring to nitrocellulose membranes. The membranes were first blocked in 5% nonfat dry milk dissolved in DPBS with 0.1% Tween 20 (PBST) for 1 h at RT, and then incubated with primary antibody at a final dilution of 1:1,000 in 5% BSA in PBST overnight at 4 °C. After washing three times with PBST, the membranes were incubated with secondary antibody at a final dilution of 1:5,000 in PBST for 1 h at room temperature. After washing three times with PBST, bound antibodies were detected by chemiluminescence. Beta-actin was used as the loading control. Primary antibodies for AC-H3 and AC-H4 were from Cell Signaling Technology (MA, USA) and the antibody for beta-actin was from Sigma-Aldrich (MO, USA).

4.3.8 Plasma Pharmacokinetics

For plasma pharmacokinetics, DOX/POEG-*b*-PSAHA micelles or free DOX.HCl was injected intravenously into tumor-free female CD1 mice at a DOX dose of 5 mg/kg, with five mice in each group. Blood samples were collected in heparinized tubes at designated time points (3min, 10 min, 30 min, 1 h, 2 h, 4 h, 8 h and 12 h) post injection. The samples were centrifuged at 12,500 rpm for 10 min at 4 °C and 20 μL of the supernatant were collected. Then 200 μL

methanol, containing 500 ng/mL daunorubicin as the internal standard, was added and vortexed for 3 min. The samples were centrifuged at 12,500 rpm for 10 min at 4 °C and 150 μL of the clear supernatant was collected and injected into HPLC for DOX analysis.

4.3.9 *In vivo* Therapeutic Study

The *in vivo* antitumor efficacy of the DOX loaded in POEG-*b*-PSAHA prodrug nanocarrier was tested in a syngeneic 4T1.2 mouse breast cancer model. Female BALB/c mice were s.c. inoculated with 4T1.2 cells at right mammary fat pad with 2×10^5 cells/mouse. When the tumor sizes reached around 50 mm^3, mice were randomly divided into five groups (n=5), and treated via tail vein injection with PBS, DOX.HCl, Doxil, DOX/POEG-*b*-POM or DOX/POEG-*b*-PSAHA micelles at a DOX dose of 5 mg/kg on days 1, 4 and 7, respectively. Tumor sizes were measured with the digital caliper every three days following the initiation of the treatment and calculated by the formula: $(L\times W^2)/2$, in which L is the longest and W is the shortest in tumor diameters (mm). Data were plotted as the actual tumor volume. Body weights were also monitored for the indication of toxicity. On day 23 post injection, all mice were sacrificed and tumor tissues were collected for measurement of weights and photography.

4.3.10 Statistical Analysis

In vitro or *in vivo* data are presented as mean ± standard deviation (SD) or mean ± standard error of mean (SEM), respectively. Statistical analysis was performed with two-tailed Student's T test or one-way analysis of variance (ANOVA) for two groups or multiple groups,

respectively, followed by Turkey simultaneous post hoc test. In all statistical analyses, $P < 0.05$ was considered statistically significant.

4.4 Results and Discussion

4.4.1 Effect of Combination of SAHA and DOX on Tumor Cell Proliferation

The proliferation inhibitory effect of SAHA and DOX was examined in 4T1.2 and HCT-116 cell lines. As shown in Figure 4-1A, SAHA or DOX inhibited the proliferation of 4T1.2 cells in a concentration-dependent manner. It was also apparent that combination of the two agents led to enhanced cytotoxicity. A similar combinational effect was found in HCT-116 cells (Figure 4-1B). Combination index (CI) was then calculated to assess a potential synergism between SAHA and DOX, by the equation $CI=(d1/IC_{50}1) + (d2/IC_{50}2)$, with d1 or d2 being the concentration of SAHA or DOX required to achieve 50% killing effect in co-treatment, while $IC_{50}1$ or $IC_{50}2$ being IC50 of SAHA or DOX in single treatment, respectively. The CI of SAHA and DOX combination were 0.67 and 0.84 in 4T1.2 and HCT-116 cells respectively, suggesting a synergism between the two drugs.

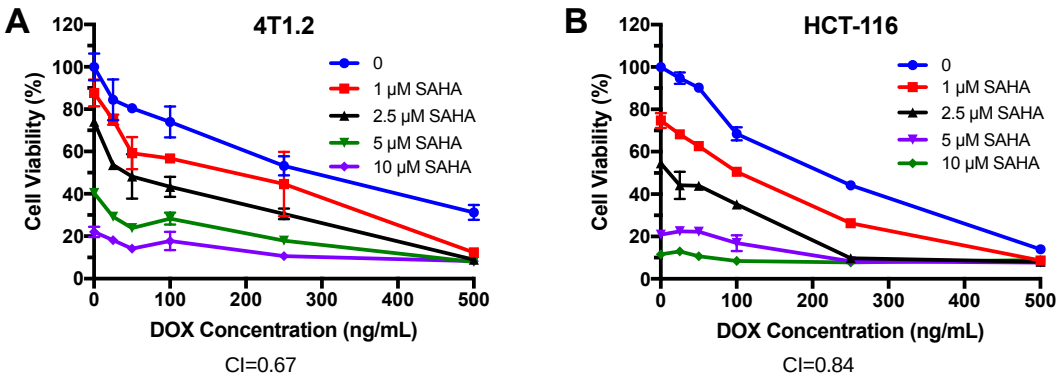

Figure 4-1. Synergistic effect between SAHA and DOX in inhibiting the proliferation of tumor cells.

4T1.2 (A) or HCT-116 (B) cells were treated with various concentrations of free SAHA, free DOX or the combination of SAHA and DOX. After 48 h, the cytotoxicity was determined by MTT assay. The experiments was performed in triplicate and repeated three times. Data are presented as means ± SD.

4.4.2 Synthesis and Characterization of the POEG-*b*-PSAHA Polymer

We initially designed and synthesized a SAHA-based monomer by directly conjugating SAHA with methacryloyl chloride. The macro-chain transfer agent POEG was then synthesized by RAFT polymerization of hydrophilic OEGMA monomer, which was further used to initiate the polymerization of hydrophobic SAHA monomer. However, micelles formed from this polymer had a size around 160 nm (data not shown), which is suboptimal for EPR effect. In order to decrease the hydrodynamic size, we re-designed a new SAHA monomer by introducing an additional 4 carbon hydrophobic chain and another benzyl ring to SAHA (Figure 4-2). Vinylbenzyl chloride was linked to succinic acid, followed by the condensation reaction with SAHA to form a hydrolysable diester bond. Then RAFT polymerization was similarly performed as described above, yielding the amphiphilic POEG-*b*-PSAHA block copolymer. The structure of POEG-*b*-PSAHA polymer was confirmed by ^{1}H NMR (Figure 4-3), and the average degree of

polymerization of the SAHA monomer was calculated. Each POEG-*b*-PSAHA molecule contained 12 units of SAHA.

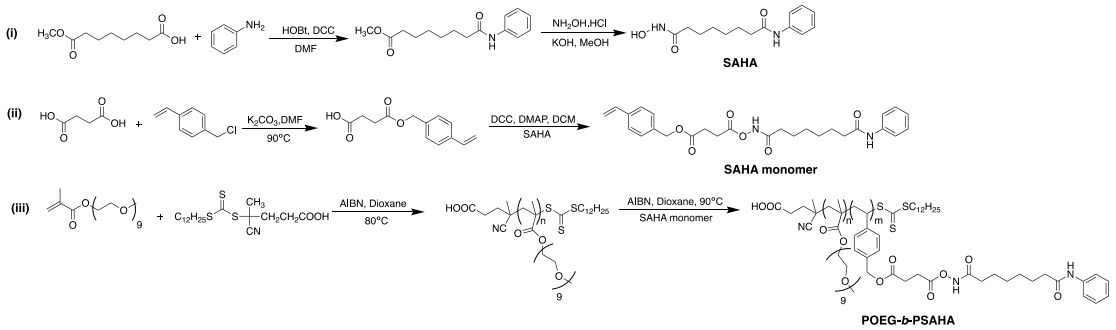

Figure 4-2. Synthesis of the SAHA-monomer and POEG-*b*-PSAHA polymers via RAFT polymerization.

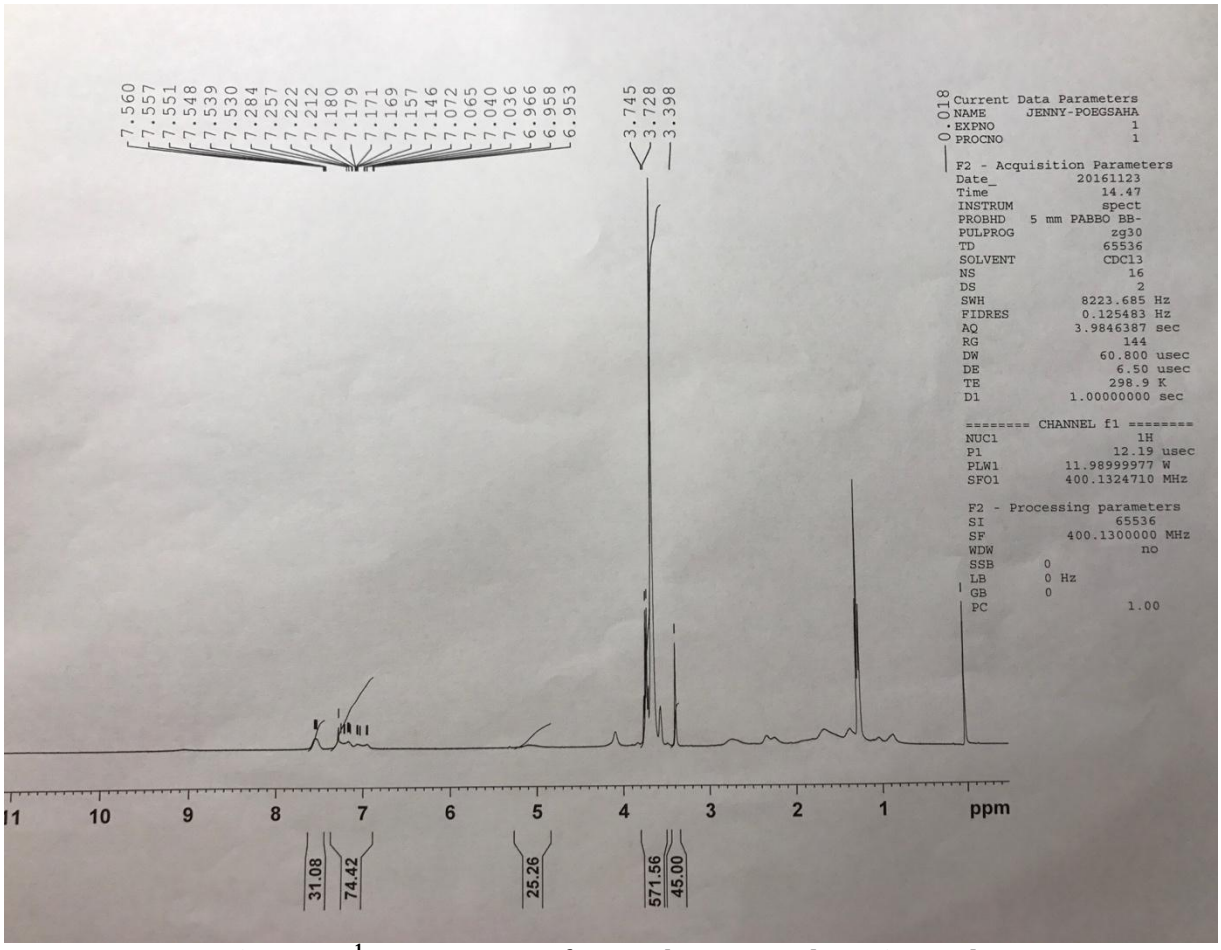

Figure 4-3. ^{1}H NMR spectra of POEG-*b*-PSAHA polymer in $CDCl_3$.

4.4.3 Characterizations of DOX-loaded POEG-*b*-PSAHA Micelles

Blank or DOX-loaded POEG-*b*-PSAHA micelles were prepared by a simple film hydration method. Unlike the initial SAHA polymer that formed relatively large-sized micelles (~160 nm), the size of drug-free POEG-*b*-PSAHA micelles was significantly smaller (63.7 nm). This is likely due to more effective carrier-carrier interaction as a result of incorporation of additional 4 carbon hydrophobic chain and another benzyl ring to SAHA monomer. Loading of DOX into POEG-*b*-PSAHA micelles at a carrier/drug weight ratio of 20:1 only led to a slight increase in the particle size (~70 nm) (Figure 4-4B). TEM showed sphere shape with a uniform size distribution, which was consistent with DLS (Figure 4-4C, D). The size, DLC, and formulation stability of drug-loaded POEG-*b*-PSAHA micelles were then examined and listed in Table 1. DOX could be loaded into POEG-*b*-PSAHA micelles at a carrier/drug ratio as low as 5/1 (mg/mg), at which ratio DOX loading capacity was 14.9 % and DOX-loaded micelles were stable for 5 days at 4 °C. With an increase in the carrier/drug ratio, the drug encapsulation efficiency and colloidal stability were further improved. As shown in Table 4-1, at a carrier/drug ratio of 50:1, DOX-loaded micelles were stable for 50 days at 4 °C. A carrier/drug mass ratio of 20:1 and 5:1 was used for *in vitro* and *in vivo* study, respectively.

Figure 4-5 shows that the CMC of POEG-*b*-PSAHA micelles was around 0.004 mg/mL (0.33 μM) as determined by a rapid change of fluorescence intensity of loaded nile red probe during serial dilution. This low CMC of POEG-*b*-PSAHA shall provide a good stability for the micelles upon dilution in blood stream after i.v. injection.

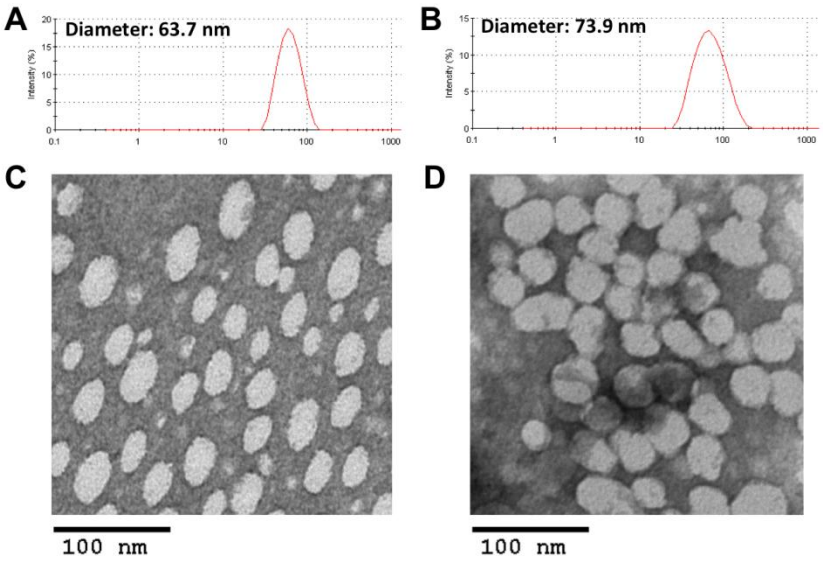

Figure 4-4. Particle size distribution of blank POEG-*b*-PSAHA micelles (A) and DOX-loaded POEG-*b*-PSAHA micelles (B). TEM images of blank POEG-*b*-PSAHA micelles (C) and DOX-loaded POEG-*b*-PSAHA micelles (D). Scale bar is 100 nm.

Table 4-1. Physicochemical characterizations of DOX-loaded POEG-*b*-PSAHA micelles.

Micelles	Mass ratio (mg/mg) [a]	Size (nm) [b]	PDI [c]	DLC (%) [d]	DLE (%) [e]	Stability [f]
POEG-*b*-PSAHA:		63.7 ± 0.7	0.14 ± 0.01			
POEG-*b*-PSAHA: DOX	5:1	78.4 ± 0.4	0.22 ± 0.01	14.9	89.3	5 d
POEG-*b*-PSAHA: DOX	10: 1	75.9 ± 0.6	0.18 ± 0.01	8.2	90.6	9 d
POEG-*b*-PSAHA: DOX	20:1	73.9 ± 0.9	0.26 ± 0.01	4.5	93.5	17 d
POEG-*b*-PSAHA: DOX	30: 1	79.7 ± 0.3	0.23 ± 0.01	3.0	92.3	32 d

POEG-*b*-PSAHA: DOX	50:1	86.6 ± 0.2	0.20± 0.01	1.9	96.7	50 d

[a] DOX concentration in micelles was kept at 0.5 mg/mL. [b] Measured by dynamic light scattering particle sizer. [c] PDI = polydispersity index. [d] DLC = drug loading capacity. [e] DLE = drug loading efficiency. f) Data mean there was no noticeable size change and visible precipitates during the follow-up period at 4 °C.

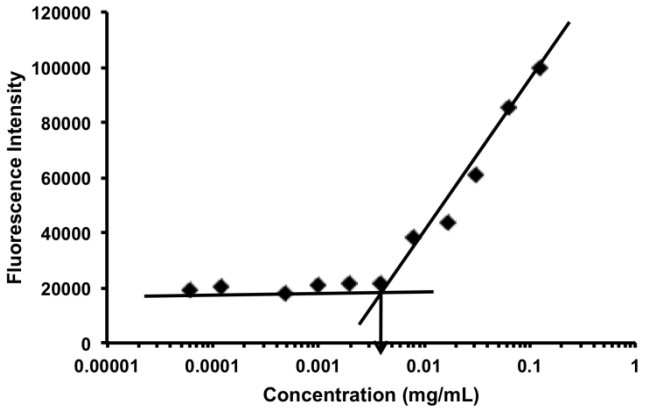

Figure 4-5. CMC of POEG-*b*-PSAHA micelles using nile red as a fluorescence probe.

4.4.4 *In vitro* Drug Release

The release profile of DOX loaded in POEG-*b*-PSAHA micelles in PBS was investigated by a dialysis method and compared to that of free DOX. As shown in Figure 4-6, around 50% of DOX was released from DOX.HCl in the first two hours and 85% of total DOX was released within 12 h. In contrast, less than 1% of DOX was released from the DOX-loaded POEG-*b*-PSAHA micelles in the first hour and a relatively sustained release continued for 72 hours, with only around 30% of total drug released. The slow release kinetics might be due to strong carrier-drug interaction, including hydrophobic interaction and π-π stacking, which shall provide a good stability of DOX/POEG-*b*-PSAHA in blood stream.

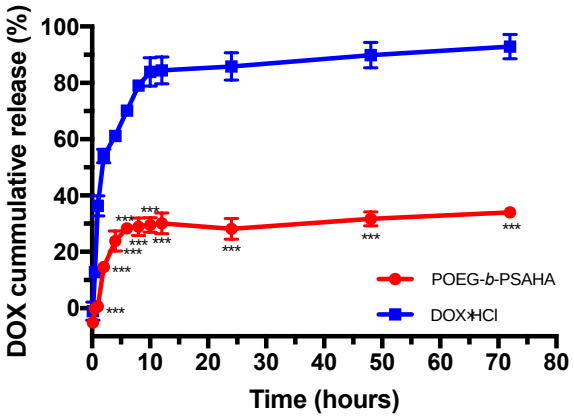

Figure 4-6. Cumulative DOX release profile from POEG-*b*-PSAHA micelles with free DOX as a control.

PBS was used as the release medium. DOX concentration was fixed at 0.5 mg/mL. Values reported are the means ± SD for triplicate samples. *** $P < 0.001$ (POEG-*b*-PSAHA/DOX vs. free DOX).

4.4.5 *In vitro* Cytotoxicity of Drug-Free or DOX-Loaded POEG-*b*-PSAHA Micelles

To evaluate whether POEG-b-PSAHA prodrug micelles maintained the ability of SAHA to inhibit tumor cell proliferation, 4T1.2, MCF-7 or HCT-116 cells were treated with POEG-b-PSAHA micelles or free SAHA (in DMSO) for 48 h. As shown in Figure 4-7A, free SAHA inhibited the proliferation of 4T1.2 tumor cells in a dose-dependent manner, while POEG-b-PSAHA showed a comparable cytotoxicity. Similar results were shown in MCF-7 and HCT-116 tumor cells (Figure 4-7B & C), suggesting that SAHA could be effectively released from POEG-b-PSAHA via the cleavage of carbamide bond.

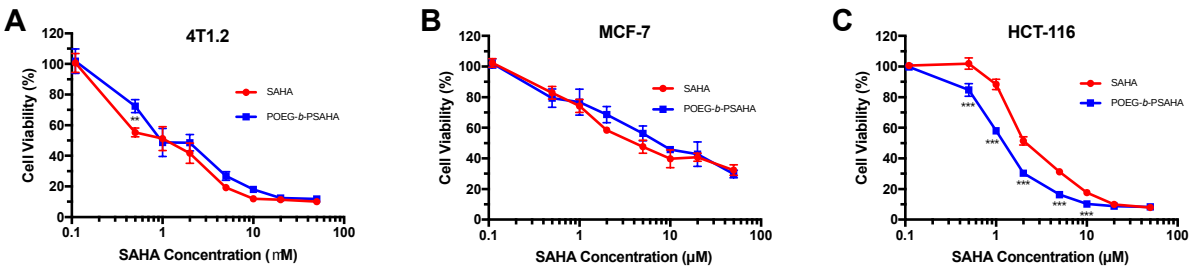

Figure 4-7. MTT cytotoxicity of POEG-*b*-PSAHA prodrug micelles in 4T1.2 mouse breast cancer cell line (A), MCF-7 human breast cancer cell line (B), and HCT-116 human colon cancer cell line (C) in comparison to free SAHA.

Cells were treated for 48 h and values reported are the means ± SD for triplicate samples. **P < 0.01, ***P<0.01 (POEG-*b*-PSAHA vs. SAHA).

The *in vitro* cytotoxicity of DOX-loaded POEG-*b*-PSAHA micelles was also tested, in comparison with DOX.HCl and DOX loaded in pharmacologically "inert" POEG-*b*-POM micelles. POEG-*b*-PSAHA and POEG-*b*-POM carrier alone were included as controls and were used at the same concentrations as those used in drug-loaded micelles. As shown in Figure 4-8A, POEG-*b*-POM blank micelles showed minimal cytotoxicity even at the highest concentration (20 μg/mL). In contrast, blank POEG-*b*-PSAHA micelles exhibited significant cytotoxicity, which was comparable to that of DOX.HCl. DOX loaded in POEG-*b*-PSAHA was more potent in killing tumor cells than DOX.HCl and DOX/POEG-*b*-POM formulation. Similar results were observed in MCF-7 and HCT-116 cells (Figure 4-8B & C). It is likely that the improved cytotoxicity of DOX/POEG-*b*-PSAHA is attributed to a synergistic action between DOX and SAHA that was released from the carrier following intracellular delivery.

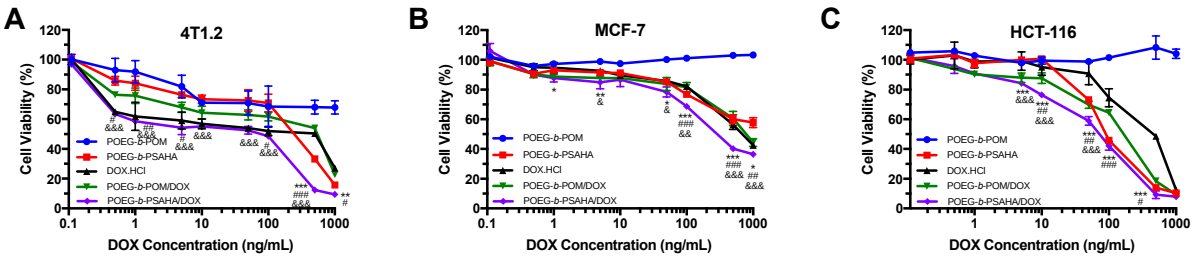

Figure 4-8. MTT cytotoxicity assay of DOX-loaded POEG-*b*-PSAHA micelles in 4T1.2 (A), MCF-7 (B) and HCT-116 (C) tumor cells after 48 h treatment.

Data are presented as the means ± SD for triplicate samples. *P<0.05, **P<0.01, ***P<0.001 (POEG-*b*-PSAHA/DOX vs. DOX.HCl); $^{\#}$P< 0.05, $^{\#\#}$P<0.01, $^{\#\#\#}$P<0.001 (POEG-*b*-PSAHA/DOX vs. POEG-*b*-POM/DOX); $^{\&}$P < 0.05, $^{\&\&}$P<0.01, $^{\&\&\&}$P<0.001 (POEG-*b*-PSAHA/DOX vs. POEG-*b*-PSAHA).

4.4.6 Effect of POEG-*b*-PSAHA on Histone Acetylation

To investigate if the POEG-*b*-PSAHA-mediated cytotoxicity is attributed to the specific action of released SAHA, we examined the efficiency of POEG-*b*-PSAHA in modulating the acetylation of histone in 4T1.2 breast cancer cells by Western blot. As shown in Figure 4-9, the basal levels of acetylated H3 and H4 were very low. SAHA treatment at submicromolar concentrations for 24 h led to significant increases in their levels in a dose-dependent manner. Interestingly, POEG-*b*-PSAHA was comparable to or even more potent than free SAHA in inducing acetylation of H3 or H4 at the same concentrations of SAHA. These data indicated that POEG-*b*-PSAHA well retained the bioactivity of SAHA in inhibiting HDAC, resulting in the hyperacetylation of histone H3 and H4 and subsequently inhibition of cancer cell proliferation. The possible mechanism for the comparable or even further enhanced efficacy in histone acetylation is that POEG-*b*-PSAHA protected the hydroxamic acid of SAHA from hydrolysis and pharmacologically active SAHA was slowly released from the polymer over a prolonged period of time. On the other hand, free SAHA with unprotected hydroxamic acid may be

subjected to rapid metabolic conversion to inactive metabolites, SAHA-glucuronide and 4-anilino-4-oxobutanoic acid [174].

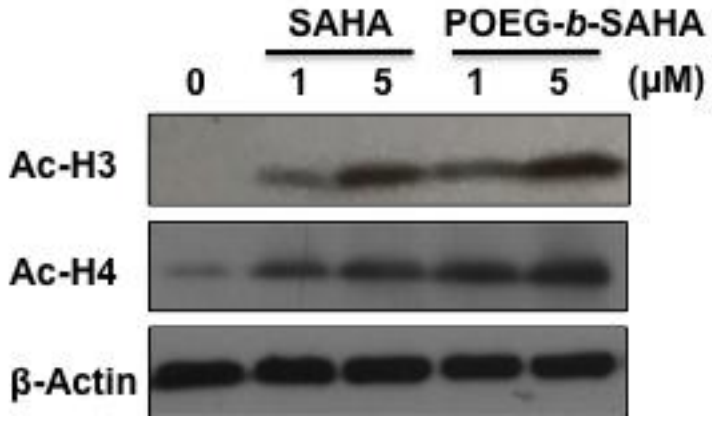

Figure 4-9. Effect of POEG-*b*-PSAHA prodrug micelles on expression of acetylated histone 3 (Ac-H3) and acetylated histone 4 (Ac-H4) compared to free SAHA.

4T1.2 cells were treated with various concentrations of SAHA or POEG-*b*-PSAHA at an equivalent concentration of SAHA for 24 h. Western blotting was performed with total protein extracts using antibodies against acetylated H3 and H4. Equal loading and transfer were verified by reproving the membranes for β-actin.

4.4.7 Plasma Pharmacokinetics

The DOX/POEG-*b*-PSAHA or DOX.HCl was injected into tumor-free mice at a DOX dose of 5 mg/kg. The plasma concentrations of DOX were examined at different time points. The initial concentration of POEG-*b*-PSAHA was around 1 mg/mL, which was 250-fold higher than its CMC (0.004 mg/mL). The concentrations of DOX in the blood following i.v. injection of different treatments as a function of time were illustrated in Figure 4-10. Compared to DOX.HCl group, the plasma concentrations of DOX from the group treated with POEG-*b*-PSAHA/DOX were significantly higher at early time points and maintained at relatively high levels until 12 h, which is likely attributed to the surface modification of PEG and stealth-shielding against RES

system. These data demonstrated that DOX formulated in POEG-*b*-PSAHA prodrug micelles was able to circulate for a significantly longer period of time in the blood.

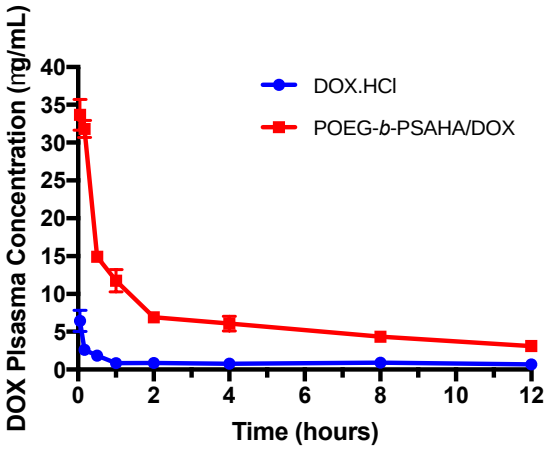

Figure 4-10. Plasma pharmacokinetics of DOX.HCl and DOX/POEG-*b*-PSAHA micelles in tumor-free female CD1 mice at the same dose of 5 mg DOX/kg.

Values reported are the means ± SEM, n =5.

4.4.8 *In vivo* Therapeutic Study

Following the demonstration of a potential synergistic effect between POEG-*b*-PSAHA-based carrier and the co-delivered DOX in cultured cancer cells, we then evaluated the tumor growth inhibitory effect of DOX/POEG-*b*-PSAHA in a highly metastatic syngeneic murine breast cancer model (4T1.2, s.c.). As shown in Figure 4-11A, free DOX exhibited a modest antitumor activity at a dose of 5 mg/kg. Doxil and DOX/POEG-*b*-POM formulations were more effective than free DOX. At the same dose of DOX, DOX/POEG-*b*-PSAHA was most effective in inhibiting the tumor growth (Figure 4-11A). Figure 4-11 B & D show the weights and images of tumor tissues collected at the end of the experiment, which were consistent with the result of tumor growth curves (Figure 4-11A). The significantly improved anti-tumor activity of DOX/POEG-*b*-PSAHA is likely attributed to the effective accumulation of the nanocarrier at

tumor sites due to its small size (~70 nm). The synergistic effect between the released SAHA and co-delivered DOX may also play an important role in tumor inhibition. More studies are needed in the future to further delineate the underlying mechanism. There were slight increases in body weights in all groups over the period of study, suggesting the negligible toxicity of DOX/POEG-*b*-PSAHA micelles in vivo.

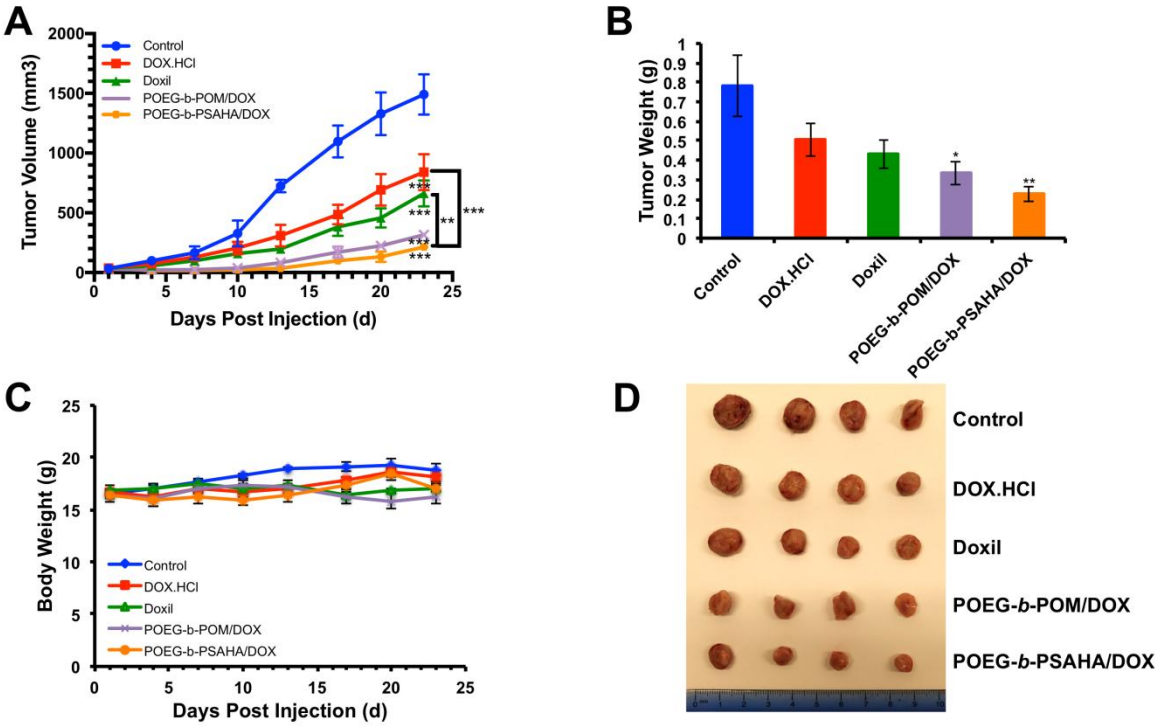

Figure 4-11. Antitumor activity of DOX-loaded POEG-*b*-PSAHA micelles in 4T1.2 breast tumor model.

(A) Antitumor activity of DOX.HCl, Doxil, DOX-loaded POEG-*b*-POM and DOX-loaded POEG-*b*-PSAHA micelles in female BALB/c mice bearing 4T1.2 breast tumor. Three injections were given on days 1, 4, 7 and each point represents the mean of actual tumor volume. (B) Weights of tumors collected from different groups at the end of experiment. (C) Changes of body weight in mice receiving different treatments. (D) Photographs of tumors collected from different treatment groups at the end of experiment. Values reported are the means ± SEM, n = 5. *P < 0.05, **P < 0.01, ***P < 0.001 (vs. control).

4.5 Discussion

In summary, we have developed a well-characterized POEG-*b*-PSAHA prodrug micellar nanocarrier, which consists of a hydrophobic segment composed of 12 SAHA-based units, and a POEG hydrophilic segment for efficient entrapment of DOX. Our POEG-*b*-PSAHA prodrug micelles well retained the biological activity of SAHA in inhibiting the proliferation of tumor cells and promoting the acetylation of histone H3 and H4. Besides, POEG-*b*-PSAHA was effective in formulating DOX and demonstrated a slow kinetics of drug release. More importantly, *in vivo* delivery of DOX via POEG-*b*-PSAHA led to significant inhibition of 4T1.2 tumor, much more effectively than DOX.HCl, Doxil and DOX/POEG-*b*-POM.

5.0 Creatine Based Polymer for Codelivery of Bioengineered MicroRNA and Chemodrugs against Breast Cancer Lung Metastasis

5.1 Abstract

Metastasis is the major cause for breast cancer related mortality. The combination of miRNA-based therapy and chemotherapy represents a promising approach against breast cancer lung metastasis. The goal of this study is to develop an improved therapy that co-delivers a novel bioengineered miRNA prodrug (tRNA-mir-34a) and doxorubicin (DOX) via a multifunctional nanomicellar carrier that is based on a conjugate of amphiphilic copolymer POEG-VBC backbone with creatine, a naturally occurring cationic molecule. Co-delivery of DOX leads to more effective processing of tRNA-mir-34a into mature miR-34a and down-regulation of target genes. DOX+tRNA-mir-34a/POEG-PCre exhibits potent synergistic anti-tumor and anti-metastasis activity in vitro and in vivo. Interestingly, the enhanced immune response contributes to the overall antitumor efficacy. POEG-PCre may represent a safe and effective delivery system for an optimal chemo-gene combination therapy.

5.2 Backgrounds

Breast cancer is the most common type of cancer and second cause of cancer-related mortality in women worldwide[175]. The main cause of death from breast cancer is metastasis, with lung, liver and bones as the major secondary target sites[176, 177]. Among different

subtypes of breast cancer, triple-negative breast cancer (TNBC) is notorious for its aggressive behavior and resistance to endocrine and anti-HER2 therapies[178]. Other than chemotherapy, treatments for metastatic TNBC are very limited[179]. Therefore, new and improved therapeutic strategies for metastatic TNBC are highly demanded.

MicroRNAs (miRNAs or miRs) are short endogenous non-coding RNAs, responsible for post-transcriptional regulation of many target genes that are involved in cancer cell proliferation and tumor progression[180]. Due to the imperfect complementarity with target mRNAs, miRs are capable of regulating a broad set of genes simultaneously, which benefits the treatment of cancer as a heterogenic disease[181]. Therefore, there has been growing interest in developing miR-based therapies. In particular, expression levels of tumor suppressive miR-34a is usually downregulated in cancerous tissues, which could be reintroduced into cancerous tissues to achieve replacement therapy[182]. Recent studies revealed that the introduction of exogenous miR-34a into cancer cells induced cell apoptosis and inhibited cell proliferation and migration through targeting Bcl-2, CD44, SIRT1, Rac1, Fra-1, Notch-1, and various cyclins[183, 184]. In addition, miR-34a has been reported to sensitize breast cancer cells to first-line chemotherapies, such as doxorubicin (DOX), paclitaxel and 5-FU[185]. Moreover, a liposome-formulated miR-34a, namely "MRX34", has entered Phase I clinical trials for the treatment of unresectable primary liver cancer[186].

One major limitation for miR-based therapies is that the source of miRs has been limited to synthetic RNAs with artificial modifications, which raises concerns over the stability, cost, specificity and safety of these RNA-based therapeutics[187]. To improve the miR-based therapy,

we have recently developed a novel miR-34a prodrug, pre-miR-34a fused to a transfer RNA (tRNA), namely tRNA-mir-34a[188]. These bioengineered miRs are produced and folded in Escherichia coli in large scale with high yield, which can effectively maintain the function and safety properties of natural RNAs and therefore represent a new class of more affordable and biocompatible miR-based agents for research and therapy. Indeed, this tRNA-carried pre-miR-34a was selectively processed into mature miR-34a in human carcinoma cells, resulting in reduced expression of the target genes and consequently the inhibition of cancer cell proliferation *in vitro* and *in vivo*[188]. However, the use of tRNA-mir-34a alone only exhibited modest effect against human lung cancer or hepatocarcinoma. The combination of tRNA-mir-34a with DOX-based chemotherapy might work synergistically to increase the antitumor efficacy while minimizing the toxicity associated with each single treatment. In this study, we aimed to develop a nanocarrier for systemic co-delivery of tRNA-mir-34a and DOX to treat metastatic TNBC.

Currently, a variety of delivery systems have been developed for gene delivery including viral carriers, peptides, liposomes and cationic polymers. Despite the high efficiency in gene delivery, viral vector-based therapies are limited by their safety concerns such as immunogenicity, and the difficulty of large-scale production[189, 190]. In contrast, non-viral nanocarriers have attracted increasing attention in nucleic acid delivery due to their favorable safety profiles and the ease of production[191]. In addition to nanocarriers designed exclusively for genes, there are growing interests in developing multi-functional nanocarriers that can simultaneously deliver multiple types of therapeutic payloads to disease sites in a targeted and controlled manner for combination therapy[192]. It has been suggested that the use of naturally

occurring molecules as building blocks of the nanocarriers is superior in achieving the properties of non-toxic, biodegradable, biocompatible and non-immunogenic[193-196].

We herein developed a multi-functional delivery system based on an amphiphilic polymer (POEG-PCre) with a naturally occurring cationic molecule creatine attached to the pendent side chain, for the co-delivery of bioengineered tRNA-mir-34a and small molecule chemodrugs. The backbone of POEG-PCre (POEG-PVBC), which consists of hydrophobic alkyl main chains and pendent benzyl rings, forms the core of micelles to load hydrophobic anticancer drugs through hydrophobic-hydrophobic interaction and π-π stacking. Creatine was post-conjugated to the backbone to introduce the positive charges, which further formed complexes with the negatively charged nucleic acids. In addition, the cationic creatine groups in the polymer can also facilitate the accumulation of nanoparticles in the lung tissue and thereby promote the subsequent interaction with tumor cells. That is because the lung is the first capillary bed encountered by cationic NPs after intravenous (i.v.) injection and therefore acts as the most effective target organ.[197] Also, the lung tissue has been reported to be endowed with a much higher polyamine active uptake system than any other major organs,[198] which may benefit the targeted delivery of creatine-based nanocarrier with amine groups to the lungs. The excess amount of positive charges on the nanocarrier was shielded by PEG to improve in vivo stability of the system. We hypothesized that the co-delivery of tRNA-mir-34a and DOX via our multi-functional nanocarrier represents a safe and effective approach for the treatment of metastatic TNBC. We first examined the biophysical properties of the nanocarrier co-loaded with DOX and tRNA-mir-34a. The efficiency of delivery and transfection was then examined both in vitro and

in vivo. Finally, the antitumor effect of DOX+tRNA-mir-34a/polymer as well as the underlying mechanism was investigated.

5.3 Experiment Procedures

5.3.1 Reagents

DOX·HCl was purchased from LC Laboratories (MA, U.S.A). Creatine, 4-Cyano-4 [(dodecylsulfanylthiocarbonyl)sulfanyl]pentanoic acid, vinylbenzyl chloride (VBC) monomer, and oligo(ethylene glycol) methacrylate (average Mn = 500, OEG500), 2-Azobis(isobutyronitrile) (AIBN), trypsin-EDTA solution, 3-(4,5-dimethylthiazol-2-yl)-2,5-diphenyl tetrazolium bromide (MTT) and Dulbecco's Modified Eagle's Medium (DMEM) were purchased from Sigma-Aldrich (MO, U.S.A). AIBN was purified by recrystallization in anhydrous ethanol. Opti-MEM medium, fetal bovine serum (FBS), Dulbecco's phosphate buffered saline (DPBS), penicillin-streptomycin solution and TRIzol lysis reagent were purchased from Invitrogen (NY, U.S.A.). QuantiTect Reverse Transcription Kit was purchased from Qiagen (MD, U.S.A). All solvents used in this study were HPLC grade.

5.3.2 Animals

Female BALB/c mice (4–6 weeks) were purchased from Charles River (CA, U.S.A). All animals were housed under pathogen-free conditions according to AAALAC (Association for Assessment and Accreditation of Laboratory Animal Care) guidelines. All animal-related

experiments were performed in full compliance with institutional guidelines and approved by the Animal Use and Care Administrative Advisory Committee at the University of Pittsburgh.

5.3.3 Cell Culture

Mouse triple negative breast cancer cells 4T1.2 and human triple negative breast cancer cells MDA-MB-231 were cultured in DMEM medium supplemented with 10% FBS and 1% penicillin/streptomycin at 37 $^{\circ}$C in a humidified atmosphere with 5% CO_2. All cell lines used in this work were obtained from ATCC (VA. U.S.A).

5.3.4 Production of MiR-34a Prodrug

The expression and purification of tRNA-mir-34a and control tRNA-MSA was carried out using a novel RNA bioengineering technology as described recently[188]. Briefly, recombinant RNAs were produced in HST08 *E. coli* and verified by denaturing urea (8 M) polyacrylamide (8%) gel electrophoresis (PAGE) analysis of total bacterial RNA isolated by phenol extraction. Target RNAs were isolated by an anion exchange fast protein liquid chromatography (FPLC) method[199] on a NGC QUEST 10PLUS FPLC system (Bio-Rad, CA, U.S.A). RNA concentrations were determined with a NanoDrop 2000 Spectrophotometer (Thermo Fisher Scientific, MA, U.S.A), and RNA purity was further determined by a high performance liquid chromatography (HPLC) assay. [188, 200] RNAs over 98% pure (by HPLC) were used in this study.

5.3.5 Synthesis of POEG-PVBC Polymer

OEG500 (550 mg, 1.1 mmol), VBC monomer (600 μL, 4.27 mmol), 4-Cyano-4-(phenylcarbonothioylthio) pentanoic acid (8 mg, 0.0286mmol), AIBN (3 mg, 0.0186 mmol), and 1 mL of dried tetrahydrofuran were added into a Schlenk tube, and deoxygenated by free-pump-thawing for three times. Then the mixture was filled with N_2 and immersed into an oil bath thermostated at 82 °C to start the polymerization. After 16 h, the reaction was quenched, and the mixture was precipitated in hexane for 3 times. The product POEG-PVBC was obtained after vacuum drying. Conversion of OEG500 monomer was 66.0% and conversion of VBC monomer was 80.0%.

5.3.6 Synthesis of POEG-PCre Polymer

The POEG-PVBC polymer (270 mg) and creatine (1 g) were mixed in 15 mL anhydrous DMF with K_2CO_3 (1 g). After stirring at 80 °C for 36 h, the reaction mixture was cooled down and transferred into a dialysis bag (MWCO=3500 Da). After dialysis against a dilute hydrochloric acid solution for 1 day and deionized water for 3 days, the solution in the dialysis bag was centrifuged at 4,500 rpm for 12 min and the supernatant was lyophilized to give the POEG-PCre polymer. ^{1}H NMR spectra were examined on a 600.0 MHz Bruker spectrometer using DMSO-d_6 as the solvent.

5.3.7 Preparation of DOX+tRNA-mir-34a Co-formulated Micelles

DOX solution was first prepared by dissolving DOX·HCl in DMSO containing triethylamine (5 equiv) overnight to remove HCl. DOX-loaded POEG-PCre micelles were prepared by the dialysis method. Briefly, 2 mg of polymer was dissolved in 200 μL DMSO and mixed with 20 μL of DOX solution (10 mg/mL). The mixture was then dialyzed against distilled deionized (DD) water using a dialysis bag (MWCO=3500) overnight to remove the unloaded free DOX. Drug-free micelles were similarly prepared without adding DOX solution. For tRNA-mir-34a complexation, polymeric micelles were diluted to different concentrations in DD water and mixed with the equivalent volume of tRNA-mir-34a (in 10% of glucose) to obtain the desired N/P ratios. This nanocomplexes was allowed to incubate at RT for 20 min prior to further characterization. *In vitro* studies were performed with freshly prepared nanocomplexes. For *in vivo* studies, micelles and tRNA-mir-34a were first mixed in DD water for 20 min, and then lyophilized with glucose as a cryoprotectant.

5.3.8 Physical Characterization of DOX+tRNA-mir-34a Co-formulated Micelles

The particle size and zeta potential of different POEG-PCre micellar formulations were assessed by dynamic light scattering (DLS) via a Zetasizer (Nano-ZS 90, Malvern Instruments, Malvern, UK). The morphology of POEG-PCre blank micelles and gene-drug-coloaded micelles was observed by transmission electron microscopy (TEM). The micelles were mounted on a copper grid with nitrocellulose supporting film. The samples were negatively stained with phosphotungstic acid and dried at room temperature before examination.

To quantify the incorporated DOX, the fluorescence intensity (λex/λem= 480 nm/590 nm) of DOX-loaded micelles and various known amounts of DOX dissolved in DMSO was measured with a SpectraMax M3 microplate reader (Molecular Devices, CA, U.S.A). The colloidal stability of POEG-PCre micellar formulations with various carrier/drug mass ratios at room temperature and 4°C was evaluated by following the changes in sizes of the particles or visible precipitates every hour in the first 12 h and daily after 12 h following sample preparation.

The CMC of POEG-PCre micelles was determined by using nile red as a fluorescence probe as described previously[201].

5.3.9 Gel Retardation Assay and Dextran Sulfate Replacement Assay

tRNA-mir-34a/polymer complexes were prepared at different N/P ratios, ranging from 1 to 40 (tRNA-mir-34a concentration was fixed at 0.02 mg/ml). The resulting nanocomplexes were then electrophoresed on a 2% agarose gel. The gels were prepared with 2% agarose in Tris-acetate-EDTA (TAE) buffer containing 0.5 μg/mL ethidium bromide (Biotium, CA, U.S.A). For electrophoretic mobility shift analysis, samples were incubated at room temperature for 20 min; BlueJuice™ Gel Loading Buffer (10X) (Invitrogen, NY, U.S.A) was then added to the samples. Gel electrophoresis was carried out at 120 V for 20 min and the gel was subsequently visualized using a UV illuminator. Free tRNA-mir-34a was served as a control. The gel retardation of plasmid/polymer complexes and siRNA/polymer complexes at different N/P ratios were performed similarly.

For replacement assay, tRNA-mir-34a/polymer complexes of various N/P ratios were first prepared. Dextran sulfate was then added to the samples with various S/P ratios (molar ratio between the sulfur from dextran sulfate and the phosphate from nucleic acid). The samples were then electrophoresed similarly as described above.

5.3.10 Stability of DOX+tRNA-mir-34a Co-formulated Micelles

Nanocomplexes were suspended in Dulbecco's phosphate-buffered saline (DPBS) of pH=7.4, BSA (30 mg/mL in DPBS) and RMPI 1640 with 10% FBS, respectively. The stability of nanocomplexes at various time periods (0, 1, 2, 4, 6, 8, 24 and 48 hours) was followed by examining their sizes via DLS.

5.3.11 Release of DOX from POEG-PCre Micelles *In Vitro*

The kinetics of DOX release from DOX/POEG-PCre or DOX+ tRNA-mir-34a/POEG-PCre was performed according to a previous report[202].

5.3.12 Cellular Uptake of DOX+tRNA-miR-34a/Polymer Complexes

tRNA-mir-34a was labeled with fluorescent dye MFP488 using Label IT® miRNA Labeling Kits (Mirus Bio, WI, U.S.A). Cellular uptake of nanocomplexes carrying tRNA-mir-34a^{MFP488} (green fluorescence) and DOX (red fluorescence) was evaluated by using confocal laser scanning microscopy (CLSM, FluoView 1000, Olympus, Japan). 4T1.2 cells were seeded in 6-well plates at a density of 2×10^4 cells/well followed by 24 h of incubation in DMEM

containing 10% FBS and 1% streptomycin/penicillin. The cells were then treated with tRNA-mir-34a^{MFP488}/POEG-PCre, DOX+ tRNA-mir-34a^{MFP488}/POEG-PCre, or DOX/POEG-PCre in Opti-MEM medium at a dose of 100 nM and 10 μM for tRNA-mir-34a^{MFP488} and DOX respectively. Free DOX.HCl and naked tRNA-mir-34a^{MFP488} were used as controls. Four h later, the cells were washed three times with cold DPBS to remove the remaining nanocomplexes. Cell nuclei were then stained with Hoechst 33342 (1 μg/mL) at room temperature for 15 min. Cells were then washed with cold DPBS three times before observation under a confocal scanning microscope.

5.3.13 Real-Time PCR

Real-Time PCR (RT-PCR) was applied to evaluate the expression level of mature miR-34a and its target genes Bcl-2 and PD-L1. Total RNA was extracted from cultured cells or frozen tumor tissues using Trizol reagent (Invitrogen, NY, U.S.A) following the protocols of the manufacturer.

For miRNA expression analysis, 1 μg of total RNA was applied for reverse transcription to synthesize cDNA of miRNA using miScript PCR starter kit (Qiagen, MD, U.S.A). Quantitative real-time PCR was performed using miScript SYBR Green PCR Kit (Qiagen, MD, U.S.A) containing miScript Universal Primer (reverse primer) and QuantiTect SYBR Green PCR Master Mix on a 7900HT Fast Real-time PCR System. Relative miRNA levels were analyzed using delta-delta-Ct calculations and normalized to U6. Each sample was analyzed in triplicate. The primers were as follows: miR-34a: 5'-TGGCAGTGTCTTAGCTGGTTGT-3''; U6: 5'-CGCAAGGATGACACGCAAATTC-3'; chimeric ncRNAs forward 5'-

GGCTACGTAGCTCAGTTGGT-3', chimeric ncRNAs reverse 5'-TGGTGGCTACGACGGGATTC-3'; pre-miR-34a forward 5'-GGCCAGCTGTGAGTGTTTCTTTGG-3', pre-miR-34a reverse 5'-GGGCCCCACAACGTGCAG-3'.

For mRNA expression analysis, cDNA was generated from the 1 μg of total RNA using QuantiTect Reverse Transcription Kit (Qiagen, MD, U.S.A) according to the manufacturer's instructions. Quantitative real-time PCR was performed using SYBR Green Mix on a 7900HT Fast Real-time PCR System. Relative target mRNA levels were analyzed using delta-delta-Ct calculations and normalized to GAPDH. The primers were as follows: mouse Bcl-2 forward 5'-GTCGCTACCGTCGTGACTTC-3', mouse Bcl-2 reverse 5'-CAGACATGCACCTACCCAGC-3'; human Bcl-2 forward 5'-GGTGGGGTCATGTGTGTGG-3', human Bcl-2 reverse 5'-CGGTTCAGGTACTCAGTCATCC-3'; mouse Dicer forward 5'-GGTCCTTTCTTTGGACTGCCA-3', mouse Dicer reverse 5'-GCGATGAACGTCTTCCCTGA-3'; human Dicer forward 5'-CGAGCCTCCATTGTTGGTCCAC-3', human Dicer reverse 5'-CCAGTTCGCCAATTTTGTGCAG-3'; mouse PD-L1 forward 5'-GCATTATATTCACAGCCTGC-3', mouse PD-L1 reverse 5'-CCCTTCAAAAGCTGGTCCTT-3'.

5.3.14 Western Blot Assay

Cultured cells or frozen tumors were harvested and lysed with RIPA lysis buffer (Thermo Fisher Scientific, MA, U.S.A) by gently shaking on ice for 30 min. After centrifugation at 12,500 g for 10 min, the supernatants were collected and the concentrations of proteins were measured

using Pierce BCA Protein Assay Kit (ThermoFisher Scientific, MA, U.S.A). The protein samples were denatured by boiling for 5 min and loaded onto 10% SDS-PAGE gel for electrophoresis. The proteins were then incubated in blocking buffer (5% non-fat dry milk in TBST) at RT for 1 h after being transferred onto PVDF membranes (Bio-Rad, CA, U.S.A). The membranes were then incubated with anti-Bcl-2 or anti-PD-L1 antibody (Cell Signaling Technology, MA, U.S.A) in antibody dilution buffer (5% BSA in TBST) with gentle agitation overnight at 4°C. After washing with TBST for three times, the membranes were subsequently incubated with the secondary HRP-linked goat anti-rabbit IgG antibody (Cell Signaling Technology, MA, U.S.A) for 1 h at RT. After another three washes washing with TBST, the membranes were incubated with Pierce™ ECL Western Blotting Substrate (Thermo Fisher Scientific, MA, U.S.A) for 1 min, wrapped in plastic and exposed to X-ray film. Protein expression was normalized against GAPDH or β-Actin expression.

5.3.15 *In Vitro* Cytotoxicity

4T1.2 (1×10^3 cells/well) or MDA-MB-231 (5×10^3 cells/well) cells were seeded in 96-well plates followed by incubation in DMEM with 10% FBS and 1% streptomycin/penicillin for 24 h. Cells were then treated with various formulations including free DOX.HCl, DOX-loaded POEG-PCre micelles, DOX+ tRNA-MSA/POEG-PCre micelles, DOX+ tRNA-mir-34a/POEG-PCre micelles, blank POEG-PCre micelles, tRNA-MSA/POEG-PCre micelles and tRNA-mir-34a/POEG-PCre micelles. The former four DOX-containing groups were compared at various equivalent concentrations of DOX. The concentrations of POEG-PCre carrier in the last three DOX-free micelles were same as those of the carrier in DOX-loaded groups. After 48 h, MTT assay was performed as described before[202].

5.3.16 Cell Apoptosis

4T1.2 cells were seeded in 6-well plates at a density of 2×10^4 cells/well followed by 24 h of incubation in DMEM containing 10% FBS and 1% streptomycin/penicillin. Cells were then treated with blank POEG-PCre micelles, tRNA-MSA/POEG-PCre micelles, tRNA-mir-34a/POEG-PCre micelles, free DOX.HCl, DOX/POEG-PCre micelles, DOX+ tRNA-MSA/POEG-PCre micelles or DOX+ tRNA-mir-34a/POEG-PCre micelles. All DOX-loaded groups contained the equivalent DOX concentration of 100 nM while the dose of tRNA-mir was100 nM of in all tRNA-miR complexed groups. After 48 h, cells were harvested, processed by using AnnexinV/propidium iodide (PI) apoptosis detection kit (BD), and subjected to flow cytometric analysis (FACSCalibur, BD, U.S.A).

5.3.17 *In Vivo* Biodistribution

Female Balb/c mice bearing 4T1.2 tumor lung metastasis were used to investigate the biodistribution of nanocomplexes. tRNA-mir-34a was labeled with MFP488 similarly as described above. Mice were injected with free DOX.HCl, DOX-loaded POEG-PCre micelles, tRNA-mir-34a ^{MFP488} loaded POEG-PCre micelles or DOX+ tRNA-mir-34a ^{MFP488}-co-loaded POEG-PCre micelles through tail vein. Major organs including lung, liver, heart, spleen and kidney were harvest from mice at 1h post injection. Tissues were then embedded in OCT and frozen in liquid nitrogen. The specimens were cryosectioned into 5 μm sections. The signals of DOX and tRNA-mir-34a ^{MFP488} in different tissues were examined under a confocal microscope.

5.3.18 *In Vivo* Anti-tumor Efficacy and Safety Profile

Female Balb/c mice at age of 4-6 weeks were injected with 4T1.2 cells (2×10^5 in 100 μL DPBS) through the tail vein. Five days after tumor cell injection, mice were randomly divided into 7 groups (n=5). Mice were treated intravenously with DPBS, tRNA-MSA-complexed POEG-PCre micelles, tRNA-mir-34a-complexed POEG-PCre micelles, free DOX.HCl, DOX-loaded POEG-PCre micelles, DOX+tRNA-MSA-co-loaded POEG-PCre micelles or DOX+tRNA-mir-34a-co-loaded POEG-PCre micelles, at a DOX dose of 5 mg/kg and a tRNA/mirs dose of 30 μg per mouse, respectively. The treatments were conducted every three days for a total of three times. Sixteen days after the first injection, all mice were sacrificed, and lung tissues were harvested, weighted and photographed. Pulmonary metastases were enumerated by intra-tracheal injection of India ink solution. India ink-injected lungs were washed in Feket's solution (300 ml 70% EtOH, 30 ml 37% formaldehyde and 5 ml glacial acetic acid) and white tumor nodules against a dark blue lung background were counted. In addition, blood sample was collected, and serum was isolated after centrifuging at 12,500 rpm for 10 min. ALT, AST and creatinine levels in serum were measured.

5.3.19 Histopathological Analysis

Major organs including lung, liver, heart, spleen and kidney were harvested and fixed in 10% formalin at the end of above treatments. The fixed samples were then embedded in paraffin and the tissue sections were performed with immunohistochemical analysis including H&E and Ki67 staining. H&E staining were performed for histological evaluation of the tumor nodules in

lungs, and Ki67 staining was carried out to evaluate the cell proliferation rate of the tumor cells. The toxicity of formulations was also assessed by H&E staining of several major organs.

5.3.20 Immune Cell Infiltration Profile in Tumor-Bearing Lungs

The immune cell population in tumor-bearing lungs with various treatments was conducted in an independent *in vivo* study. Mice received similar treatments as described in the therapeutic study. Twenty-four hours after the last injection, lungs and spleens were collected in serum free RPMI medium. Lungs were cut mechanically with scissors and digested with Liberase TL and DNase I. Tissues were further grinded and filtered through a 70 mm cell strainer with red blood cells lysed by ACK lysis buffer. TILs and MDSC cells were further purified and stained with fluorescence-labeled antibody for flow cytometry analysis using a FACS flow cytometer according to a previous report[203].

5.3.21 Statistics

In vitro or in *vivo* data are presented as mean ± standard deviation (SD) or mean± standard error of mean (SEM), respectively. Two-tailed Student's T test or analysis of variance (ANOVA) was used to compare two groups or multiple groups, respectively. Significance was determined with Tukey simultaneous post hoc test. In all statistical analyses, $P < 0.05$ is considered statistically significant.

5.4 Results

5.4.1 Synthesis of POEG-PCre Polymers

The POEG-PCre polymer was synthesized by RAFT co-polymerization of OEG500 monomer and VBC monomer, followed by conjugation with creatine (Figure 5-1). The ^{1}H nuclear magnetic resonance (NMR) spectra of the POEG-PVBC and POEG-PCre were shown in Figure 5-2. The units of OEG and VBC were calculated to be 25 and 118, respectively, according to the monomer conversion. The conjugated units of creatine were calculated to be 47 by comparing the characteristic signals at 4.12-4.8 (f), 5.07 (e), and 5.95-7.88 (c and d) ppm (Figure 5-2b).

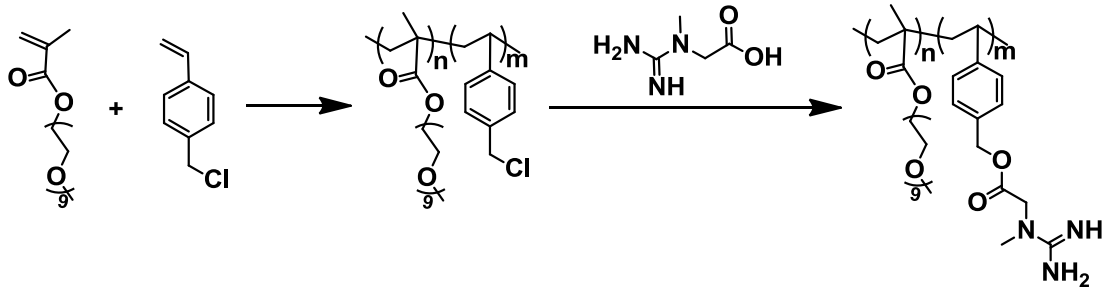

Figure 5-1. Synthesis of POEG-PCre polymer via RAFT co-polymerization of OEG500 monomer and VBC monomer, followed by conjugation with creatine.

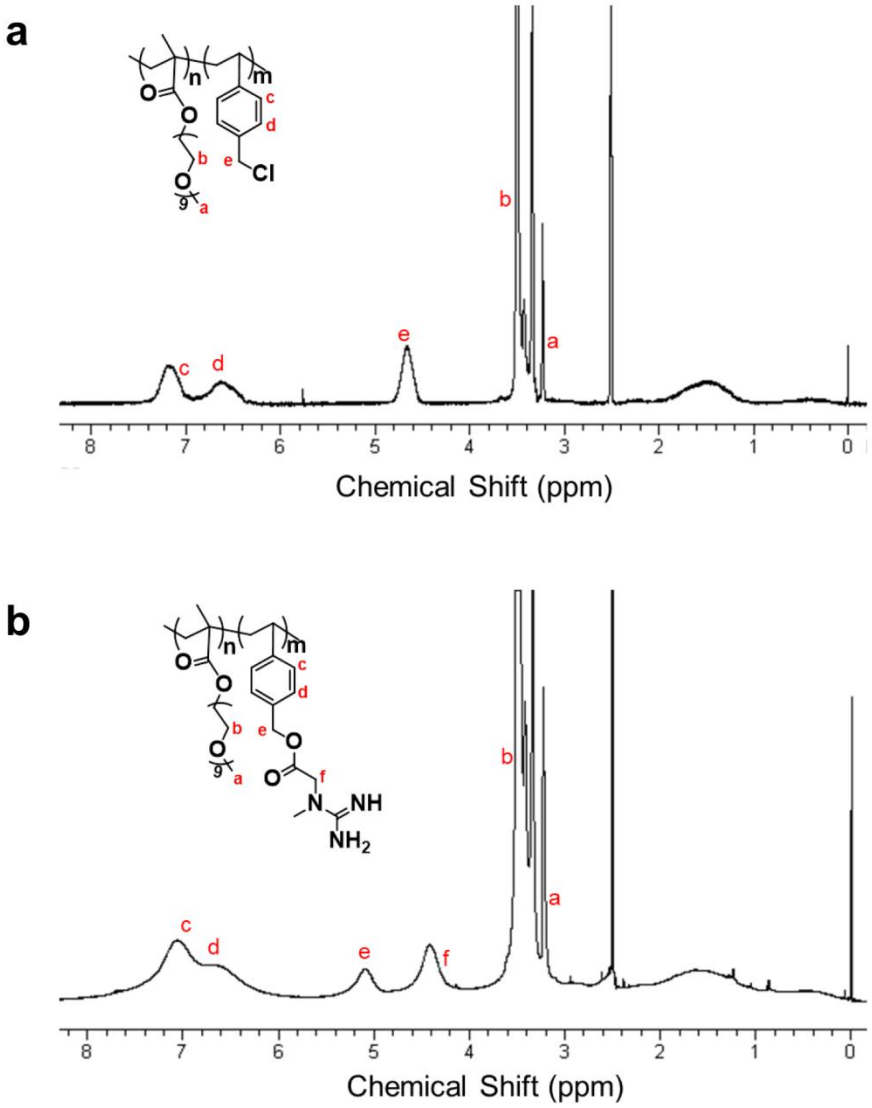

Figure 5-2. ^{1}H NMR spectra of the a) POEG-PVBC and b) POEG-PCre polymers in DMSO-d_6.

5.4.2 Characterization of Micellar Nanoparticles

POEG-PCre micelles were prepared by dialysis. As shown in Figure 5-3a, POEG-PCre copolymer self-assembled into spherical nanoparticles with a size around 180 nm as indicated by dynamic light scattering (DLS) and transmission electron microscopy (TEM). The critical micellar concentration (CMC) of POEG-PCre copolymer, determined using nile red as a

fluorescence probe,[202] was as low as approximately 0.05 mg/mL (3.0 μM) ((Figure 5-3b). The low CMC indicated the stability of POEG-PCre micelles upon dilution in the blood stream after i.v. injection. The DOX-loaded POEG-PCre micelles were similarly prepared. DOX could be incorporated into POEG-PCre micelles at a carrier/drug ratio of 5:1 (w/w) or higher (data not shown). A carrier/drug ratio of 10:1 was chosen for the subsequent studies due to the relatively high drug loading capacity and the excellent colloidal stability (stable for one month and two months at RT and 4°C, respectively). DOX-loaded POEG-PCre micelles were comparable to blank POEG-PCre micelles in size and morphology (Figure 5-3a).

The surface zeta potential of POEG-PCre micelles was approximately +40 mV (Figure 5-3e). We then tested whether the cationic micelles could form stable complexes with tRNA-mir-34a via gel retardation assay. POEG-PCre micelles were mixed with tRNA-mir-34a at various N/P ratios (the number of nitrogen residues (N) in the cationic polymer per phosphate (P) of nucleic acids) from 1:1 to 40:1. As shown in Figure 5-3c, complete complexation of tRNA-mir-34a by POEG-PCre polymer was achieved at an N/P ratio of 5:1 or greater. Accordingly, in Figure 5-3e, at N/P ratios of below 5, the net charges of nanocomplexes were negative with the particle sizes similar to that of blank micelles. At an N/P ratio of 5, a significant increase in particle size was observed with particle charges close to neutral. Interestingly, further increases in N/P ratios led to continuous increases in zeta potentials and decreases in particle sizes, suggesting gradual condensation of nucleic acid by POEG-PCre cationic polymer. In order to form more compact POEG-PCre/tRNA-mir-34a complexes as well as to overcome the neutralization by serum proteins, an N/P ratio of 20 was chosen for all subsequent studies. At this N/P ratio, the average size of the nanocomplexes decreased to around 120 nm (Figure 5-3a). In

addition, DOX loading had negligible effect on the size distribution, zeta-potential and nucleic acid binding ability of POEG-PCre micelles (Figure 5-3a, 1c, 1e).

The binding ability of POEG-PCre to plasmid or siRNA was also investigated. Compared to complexation with tRNA-mir-34a, POEG-PCre polymer could form stable complexes with plasmid at a lower N/P ratio of 2.5:1 (Figure 5-4a). However, POEG-PCre polymer was not effective in complexing with siRNA at an N/P ratio as high as 80:1 (Figure 5-4b), suggesting that our POEG-PCre carrier was unique in forming complexes with nucleic acids with appropriate sizes and secondary structures including tRNA-mirs. To further investigate the interaction between POEG-PCre nanocarrier and tRNA-mirs, a competitive binding gel-shift assay with dextran sulfate was performed. As shown in Figure 5-3d, at an N/P ratio of 5:1, substantial amounts of tRNA-mir-34a began to be released from POEG-PCre nanocarrier or PEI at an S/P ratio (molar ratio between the sulfur from dextran sulfate and the phosphate from tRNA-mir-34a) of 5 or greater. When the N/P ratios reached 10:1 or higher, tRNA-mir-34a could not be replaced by dextran sulfate even at an S/P ratio as high as 80. In contrast, an obvious release of tRNA-mir-34a was observed from PEI carrier at the corresponding N/P ratios. These data suggest that, in addition to electrostatic interaction as seen with PEI, other interactions, such as π-π stacking between the pendent benzyl rings of our polymer and the base π-systems of nucleic acids, might also contribute to a more stable nanocomplexing system.

The release kinetics of DOX from DOX-loaded POEG-PCre micelles was investigated by dialysis against DPBS of pH 7.4 at 37 °C. As shown in Figure 5-3f, more than 80% of free DOX was diffused out of dialysis bag (MWCO=3500) in the first 4 h. On the contrary, only 16 % of

DOX was released from DOX/POEG-PCre micelles in first 4 h, and less than 40 % of DOX was released for an extended period of 96 h. POEG-PCre micelles co-loaded with DOX and tRNA-mir-34a exhibited a comparable but slightly slower release profile compared with micelles loaded with DOX alone.

We further examined the stability of our nanocomplexes in various solutions that mimic commonly used buffer, routine cell culture medium or serum (i.e. DPBS of pH 7.4, DMEM medium with 2% FBS or 30 mg/mL of BSA), respectively. As shown in Figure 5-3g, no aggregation of nanoparticles was observed in all tested solutions and all of the nanocomplexes showed minimal changes in sizes for up to 48 h.

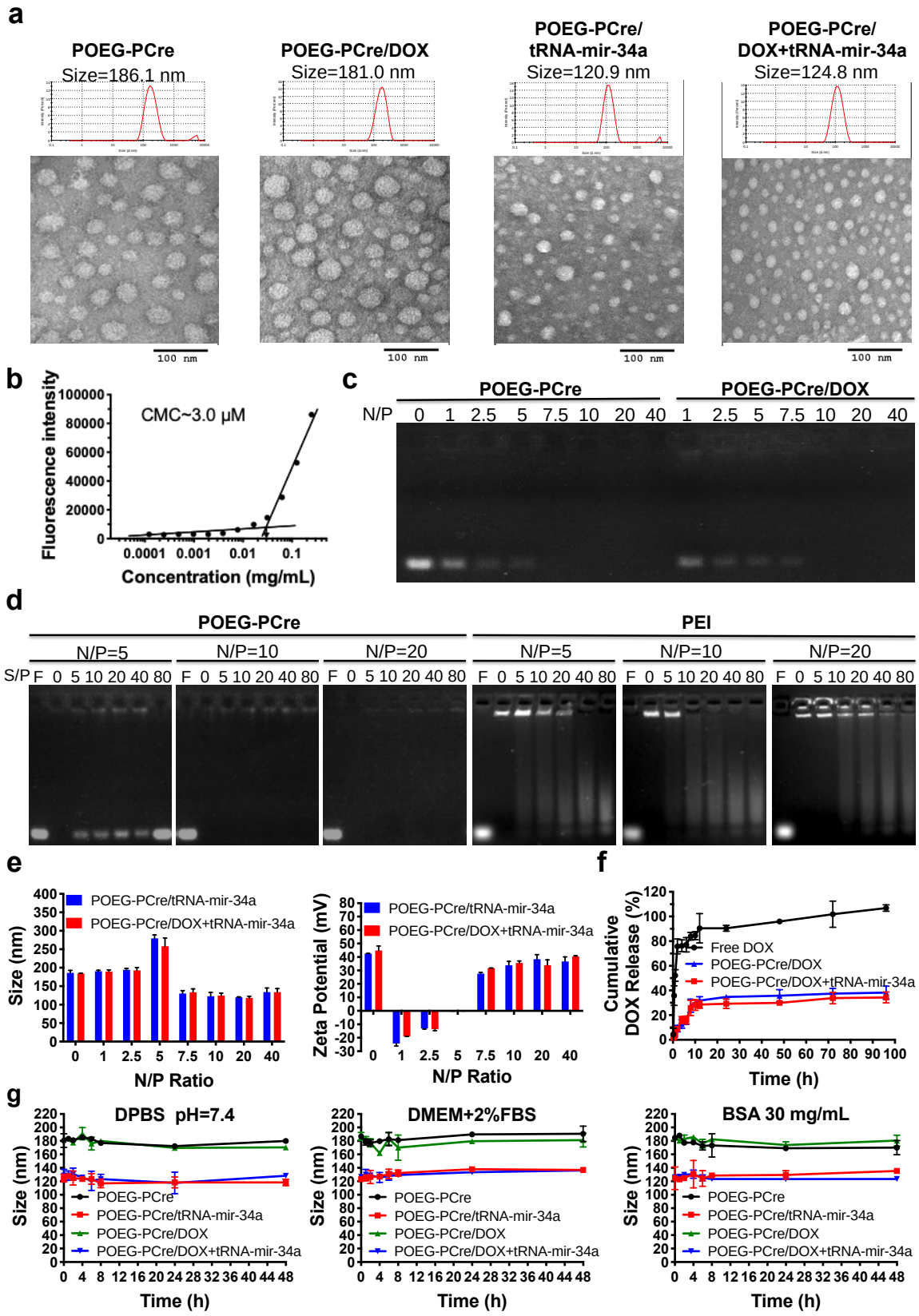

Figure 5-3. ***In vitro*** **biophysical characterizations of micelles.**

a) Size distribution and morphology of blank micelles, tRNA-mir-34a complexed micelles, DOX-loaded micelles and micelles co-loaded with tRNA-mir-34a and DOX (carrier: drug = 10: 1, w/w; carrier: tRNA-mir-34a = 20: 1, N/P) were examined by DLS and TEM, respectively. Scale bar, 100 nm. b) CMC of POEG-PCre polymers determined from the plot of nile red fluorescence intensity. c) Gel retardation assay of tRNA-mir-34a/polymer and tRNA-mir-34a+DOX/polymer complexes at different N/P ratios. Samples were incubated for 20 min at room temperature before being loaded onto a 2% (w/v) agarose gel (120 V, 20 min). d) Dextran sulfate competitive binding gel electrophoresis assay for tRNA-mir-34a/vector complexes (N/P=5, N/P=10 and N/P=20) at various S/P ratios. The experiments were repeated three times. e) Particle sizes and zeta potentials of tRNA-mir-34a/polymer and tRNA-mir-34a+DOX/polymer complexes formed at different N/P ratios. f) In vitro drug release profiles of DOX from DOX/POEG-PCre and DOX+tRNA-mir-34a/POEG-PCre in comparison with free DOX diffusion in DPBS at 37°C. g) The stability of blank micelles, tRNA-mir-34a complexed micelles, DOX-loaded micelles and micelles co-loaded with tRNA-mir-34a and DOX was examined by incubating nanocomplexes with DPBS (pH=7.4), DMEM with 2% FBS or BSA (30mg/mL) at room temperature. Changes in sizes of the complexes were followed by DLS. Data are means ± SD (n=3).

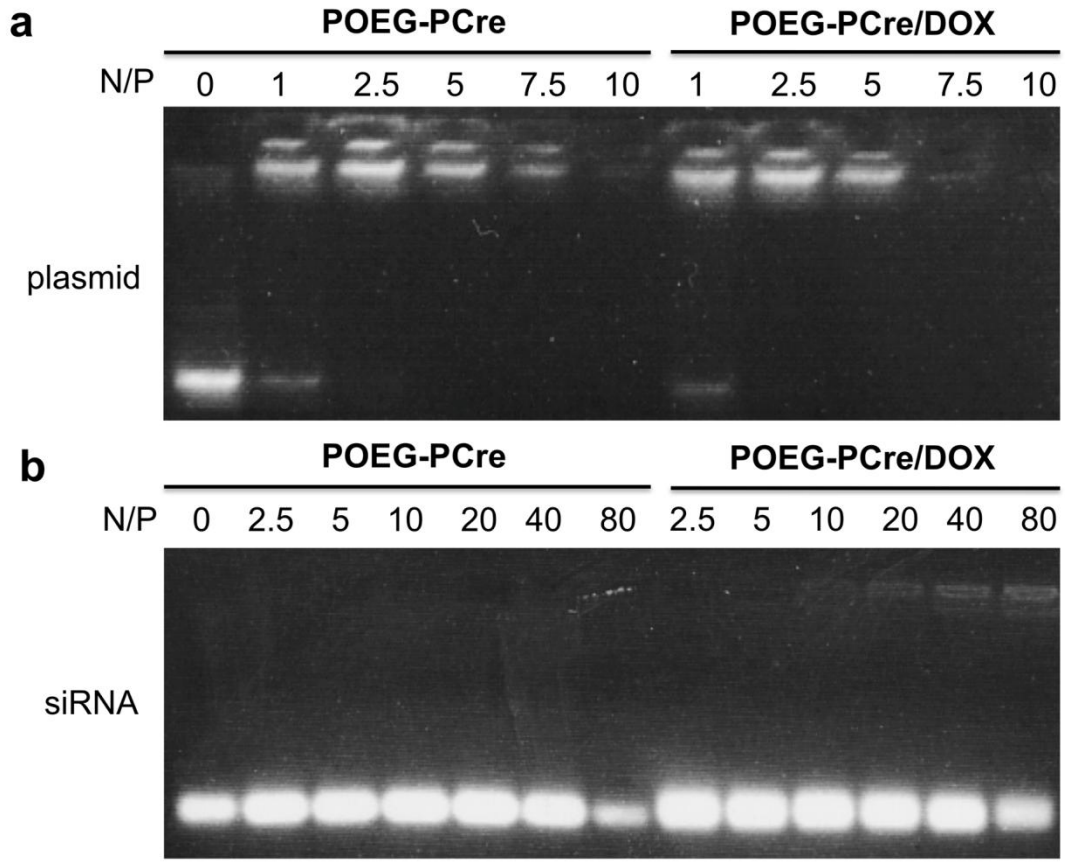

Figure 5-4. a) Gel retardation assay of EGFP plasmid/POEG-PCre complexes at different N/P ratios. b) Gel retardation assay of siRNA/ POEG-PCre complexes at different N/P ratios. The experiments were repeated three times.

5.4.3 Cellular Internalization of Nanocomplexes

To monitor intracellular co-delivery of DOX and tRNA-mir-34a, tRNA-mir-34a was labeled with MFP488 fluorescent dye in order to visualize the cell uptake of tRNA-mir-34a along with red fluorescence of DOX. 4T1.2 cells were incubated for 4 h with micelle complexes carrying DOX and/or MFP488-labeled tRNA-mir-34a and then observed under a confocal microscope. Naked tRNA-mir-34a without any transfection agent was used as a negative control. As shown in Figure 5-5, DOX/POEG-PCre showed more DOX fluorescence signal compared to

free DOX at the same dose of DOX. Interestingly, the DOX+tRNA-mir-34a^{MFP488} co-loaded POEG-PCre micelles showed even more uptake of DOX than that of the DOX/POEG-PCre micelles, which might be due to a more condensed structure after complexation with tRNA-mir-34a, leading to higher endocytosis efficiency. Overlay of DOX (red) and tRNA-mir-34a^{MFP488} (green) generated the yellow signals in the merged channel, suggesting the co-localization of DOX and tRNA-mir-34a^{MFP488} inside tumor cells. In addition, fluorescence signals of both DOX and tRNA-mir-34a^{MFP488} were present in the perinuclear regions of the cytoplasm in nanocomplexes treated groups, while the DOX fluorescence signals in free DOX treated group were profoundly observed in the nucleus overlapping with Hoechst staining (blue). These data suggest different cellular uptake routes of free DOX and DOX-loaded micelles, through passive diffusion and endocytosis, respectively.

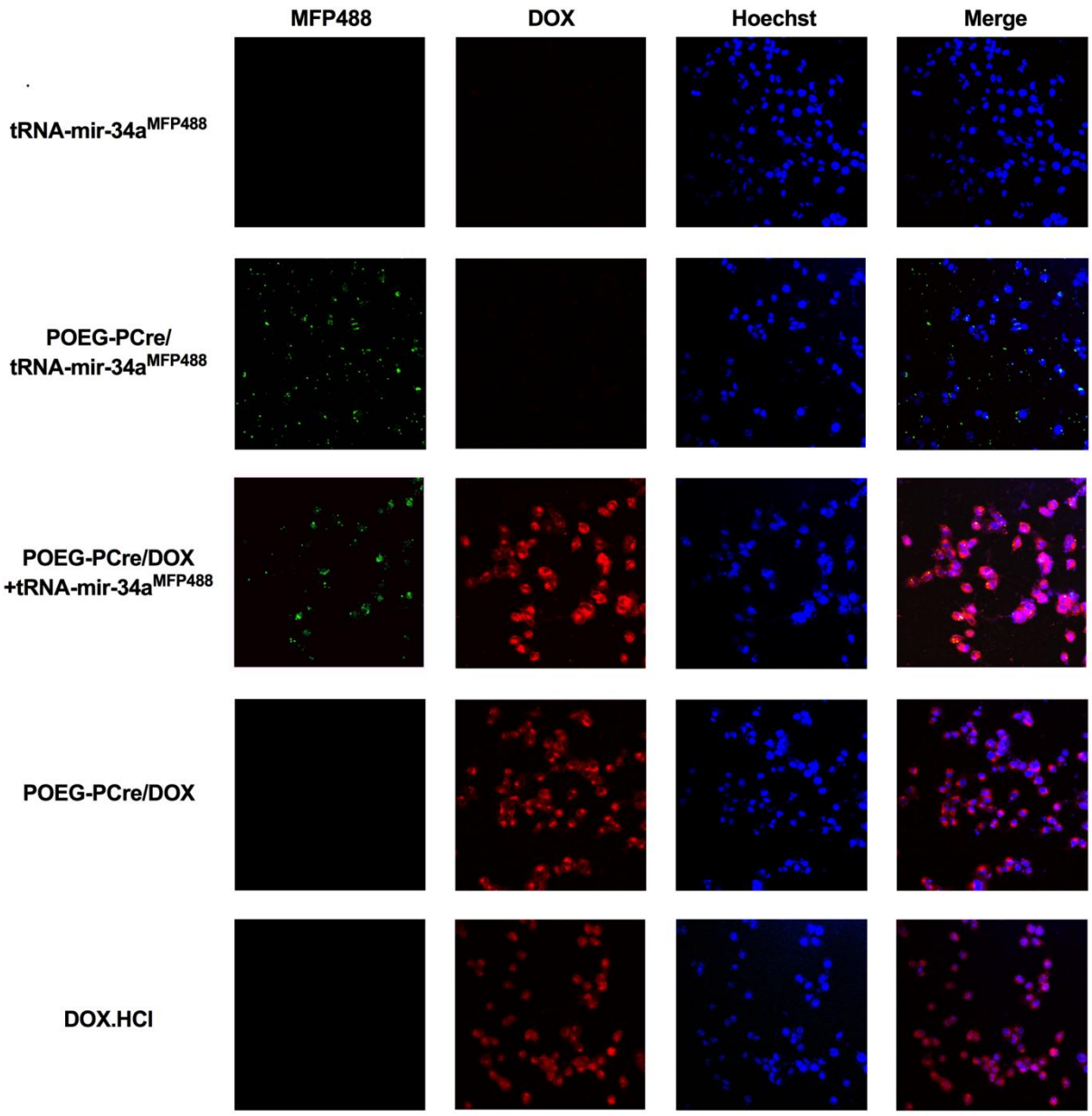

Figure 5-5. Internalization and colocalization of DOX+tRNA-mir-34a^{MFP488}/POEG-PCre in 4T1.2 breast cancer cells at 4h post incubation was monitored by confocal microscope.

From left to right: MFP488-labeled tRNA-mir-34a (green); DOX (red); nuclear staining with Hoechst 33342 (blue); an overlay of MFP488, DOX and Hoechst. The experiments were repeated three times.

5.4.4 Generation of Mature MiR-34a and Suppression of Target Gene Expression

The processing of tRNA-mir-34a into mature tumor suppressor miR-34a was evaluated by quantitative RT-PCR. As shown in Figure 5-6a, there was over a 200-fold increase in the amount of mature miR-34a in 4T1.2 cells after treatment with tRNA-mir-34a/POEG-PCre nanocomplexes. Interestingly, significantly greater amounts of mature miR-34a (~1200-fold increase) were found in cells treated with the DOX+tRNA-mir-34a co-loaded POEG-PCre micelles. This is unlikely due to the differences in the amounts of tRNA-mir-34a delivered intracellularly since comparable levels of MFP488 fluorescence were found for the two groups (Figure 5-6). Consistently, Figure 3b shows that the amounts of chimeric ncRNA scaffold inside 4T1.2 cells were similar after treatment with either POEG-PCre/tRNA-mirs or POEG-PCre/DOX+tRNA-mirs, suggesting comparable efficiency of delivery of the two formulations. Rather it might be due to a more efficient processing of tRNA-mir-34a in cells following co-delivery of DOX. Figure 5-7 shows that treatment with free DOX or DOX-loaded POEG-PCre micelles led to the induction of Dicer, an RNase III enzyme involved in pre-miRs cleavage, in a dose-dependent manner. As a result, the level of pre-miR-34a in DOX+tRNA-mir-34a/POEG-PCre-treated cells was significantly lower than that in cells treated with tRNA-mir-34a/POEG-PCre, suggesting a more complete processing of pre-miR-34a into mature miR-34a as a result of the co-delivered DOX (Figure 5-6c). Similar trends were observed in MDA-MB-231 cells (Figure 5-6a-c; Figure 5-7).

The anti-apoptotic Bcl-2 has been previously identified as a downstream target of miR-34a.[204] The expression of Bcl-2 was then evaluated at both the transcript and protein levels after intracellular delivery of tRNA-mir-34a. tRNA-MSA (Sephadex aptamer tagged methionyl-

tRNA), the sole tRNA scaffold, was used as a control. As shown in Figure 5-6d, the mRNA expression levels of Bcl-2 in cells treated with blank POEG-PCre micelles, tRNA-MSA/POEG-PCre micelles, free DOX, DOX/POEG-PCre micelles or DOX+tRNA-MSA/POEG-PCre micelles were similar to that of untreated control cells, suggesting that POEG-PCre carrier, tRNA-MSA and DOX had minimal regulatory effects on the expression of Bcl-2. In contrast, significant down-regulation of Bcl-2 expression was observed in the tumor cells treated with POEG-PCre/tRNA-mir-34a or the co-loaded formulation. Consistently, the downregulation of Bcl-2 was reaffirmed at the protein level by Western blotting (Figure 5-6e). Importantly, the down-regulation of Bcl-2 was more significant in cells treated with the co-loaded formulation than cells treated with POEG-PCre/tRNA-mir-34a. Similar results were found in MDA-MB-231 cells (Figure 5-6d and e).

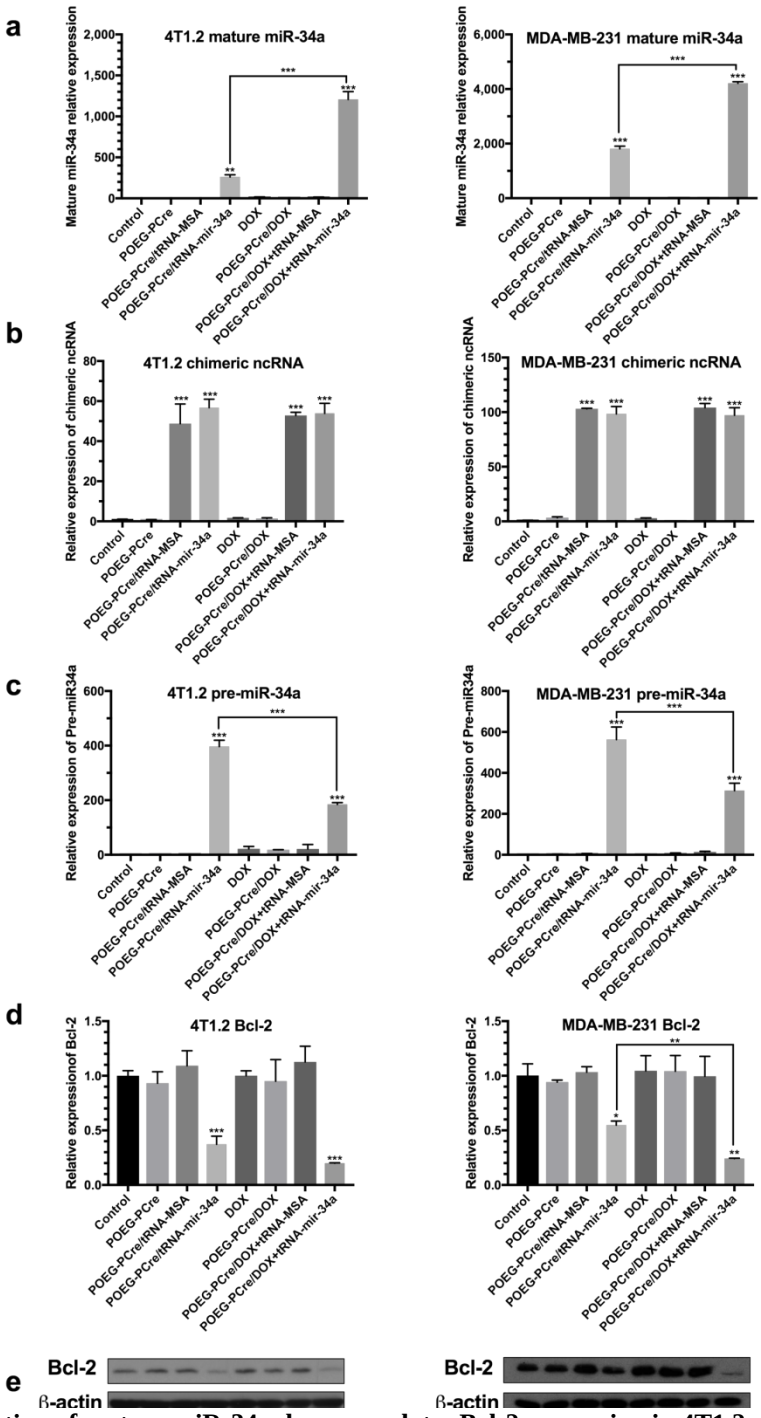

Figure 5-6. Restoration of mature miR-34a down-regulates Bcl-2 expression in 4T1.2 and MDA-MD-231 cancer cells after treatment with different formulations.

Cells were harvested at 48 h after treatment. a-c) Mature miR-34a (a), chimeric ncRNA (b) and pre-miR-34a (c) expression levels were detected by RT-PCR. d) The mRNA expression of Bcl-2 was quantitatively analyzed by RT-PCR. e) The protein expression of Bcl-2 was

evaluated by Western blot. Data are means ± SD (n=3). P values were generated by one-way ANOVA using the Tukey test for multiple comparisons. *P < 0.05, **P < 0.01, ***P < 0.001.

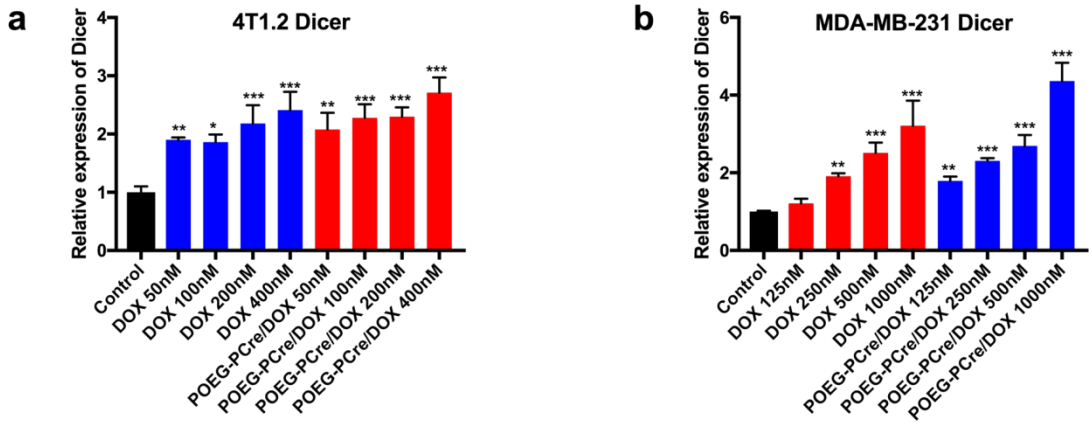

Figure 5-7. The mRNA expression of Dicer in a) 4T1.2 and b) MDA-MB-341 cells after treatment with various doses of DOX-containing formulations evaluated by RT-PCR.

5.4.5 MTT Assay, Apoptosis Assay and Cell Migration

The *in vitro* cytotoxicity of DOX+tRNA-mir-34a co-loaded POEG-PCre micelles was evaluated by MTT assay. Tumor cells were treated with various formulations for 48 h, with the doses of DOX, tRNA-mirs, and POEG-PCre carrier ranging from 7.8 to 1,000 ng/mL, 0.78 nM to 100 nM, and 78 ng/mL to 10000 ng/mL, respectively. As shown in Figure 5-8a, no obvious cell growth inhibition was noticed in cells treated with POEG-PCre nanocarrier alone or tRNA-MSA loaded POEG-PCre micelles, even at the concentration of the polymer as high as 10 μg/mL. TRNA-mir-34a/POEG-PCre micelles showed a moderate level of cytotoxicity at high concentrations. Free DOX inhibited the proliferation of tumor cells in a dose-dependent manner and the cytotoxicity of DOX/POEG-PCre was comparable to that of free DOX. Incorporation of tRNA-MSA into DOX/POEG-PCre micelles showed minimal impact on the overall cytotoxicity of the co-loaded formulation. In contrast, incorporation of tRNA-mir-34a into DOX/POEG-

PCre micelles led to a significant enhancement in the cytotoxicity of nanocomplexes on 4T1.2 cells, indicating the synergistic effect between co-delivered tRNA-mir-34a and DOX via our POEG-PCre system. A similar trend was also observed in MDA-MB-231 breast cancer cells (Figure 5-8a).

We then assessed the enhanced cytotoxicity of DOX+tRNA-mir-34a-co-loaded nanocomplexes via apoptosis assay. Cell apoptosis was evaluated quantitatively by Annexin V/propidium iodide flow cytometry. As shown in Figure 5-8b, few apoptotic cells were detected in control cells or cells treated with POEG-PCre carrier alone or tRNA-MSA loaded nanocomplexes, which was in agreement with the results of MTT assay. An increase in cell apoptosis (~21%) was observed in cells treated with tRNA-mir-34a loaded nanoparticles, suggesting that increased expression of mature miR-34a after delivery of tRNA-mir-34a into tumor cells can trigger the apoptosis of breast cancer cells due to the tumor suppressor functions of miR-34a. Free DOX, DOX/POEG-PCre and DOX+tRNA-MSA/POEG-PCre were comparable in inducing cell apoptosis to a significantly higher level (~31%). Importantly, a significantly higher percentage of necrosis (~ 13%), in addition to much greater degree of late apoptosis (~20%) and comparable level of early apoptosis, was obtained in cells treated with DOX+tRNA-mir-34a co-loaded formulation, which confirms a potent synergy between tRNA-mir-34a and DOX in inducing apoptosis and necrosis.

Besides cancer cell viability, cell migration is a critical process for tumor progression and metastasis. MiR-34a was reported to be functional as an anti-metastatic miRNA by directly targeting CD44 and NOTCH-1.[184, 205] Therefore, we investigated the effects of tRNA-mir-

34a and DOX co-loaded nanocomplexes on the cell migration using the wound closure assay. As shown in Figure 5-8c and Figure 5-9, the wounded area was substantially repopulated by highly aggressive 4T1.2 cancer cells after 24 h in groups with no treatment or treated with POEG-PCre nanocarrier alone or tRNA-MSA loaded nanocomplexes. Significant inhibition (~75%) of cell migration was observed in cells treated with tRNA-mir-34a/POEG-PCre. Three DOX-containing formulations (free DOX, DOX/POEG-PCre or DOX+tRNA-MSA/POEG-PCre) had comparable potency with a modest inhibition of ~40 %. In contrast, the DOX/tRNA-mir-34a-co-loaded group was most effective in inhibiting the migration of cancer cells; the denuded area was well retained with only 4.9 % of repopulated cells.

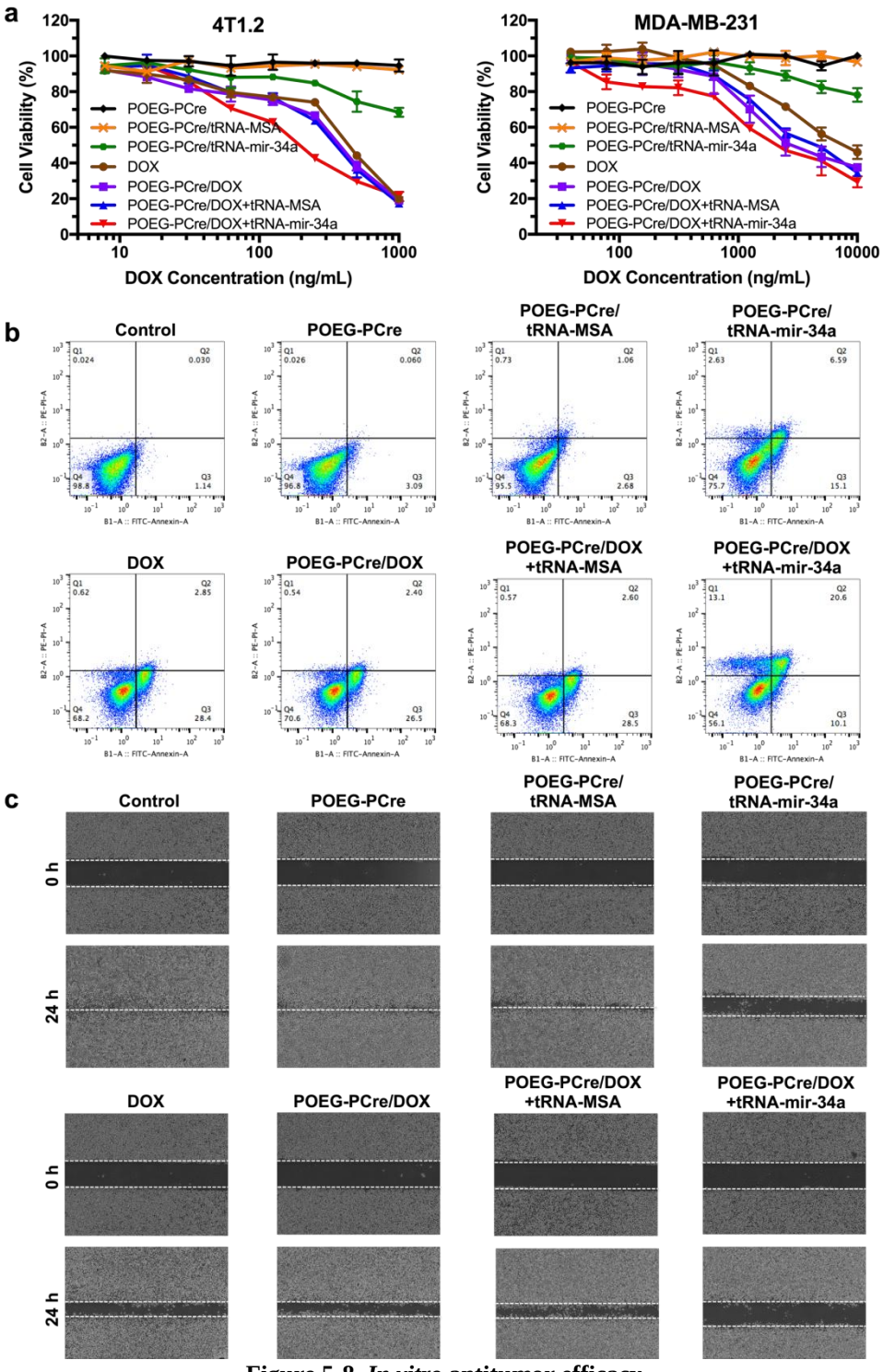

Figure 5-8. *In vitro* antitumor efficacy.

a) Cell cytotoxicity of 4T1.2 and MDA-MD-231 cancer cells treated with different formulations after 48 h. Data are means ± SD (n=3). b) Cell apoptosis of 4T1.2 cells detected by flow cytometry using an AnnexinV-FITC/PI

apoptosis detection kit after 48 h. c) Inhibition migration of 4T1.2 cells examined by wound healing assay after 24 h. The experiments were repeated three times.

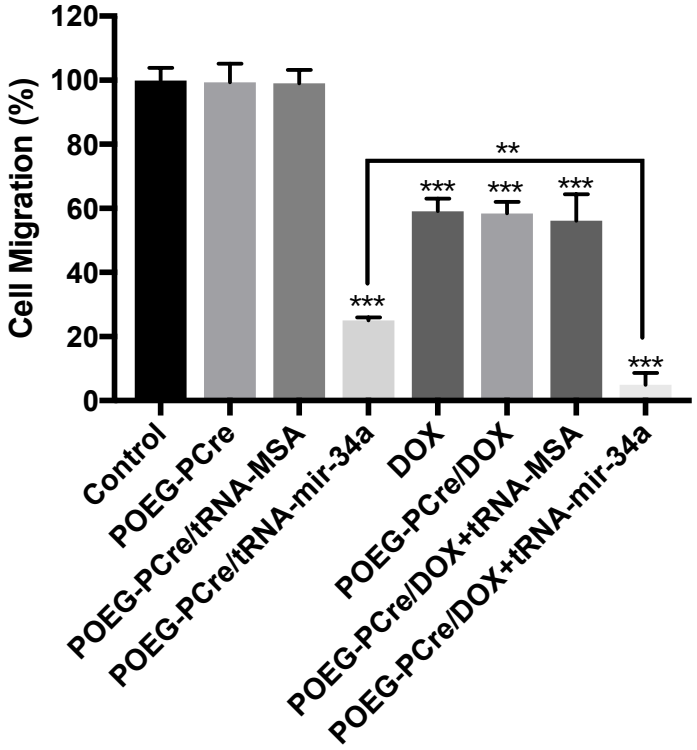

Figure 5-9. Quantitative determination of cell migration of 4T1.2 cells after 24 h.

Data are means ± SD (n=3). P values were generated by one-way ANOVA using the Tukey test for multiple comparisons. **P < 0.01, ***P < 0.001.

5.4.6 *In Vivo* Biodistribution

To gain insight into the biodistribution of nanocomplexes, the fluorescence signals of DOX and MFP488-labeled tRNA-mir-34a in tissue sections were examined by confocal microscopy. As shown in Figure 5-10, substantial amounts of fluorescent signals of both DOX and MFP488 were detected in lungs treated with DOX+tRNA-mir-34aMFP488 co-loaded micelles. The yellow color in the merged channel indicated the co-localization of DOX and tRNA-mir-34a in lung tissues. Compared to the lungs, substantially lower levels of fluorescent

signals were observed in other major organs (Figure 5-11), suggesting that POEG-PCre nanocarrier is particularly suitable for targeted co-delivery of DOX and tRNA-mir-34a to lungs, which may benefit the prevention and treatment of breast cancer lung metastasis.

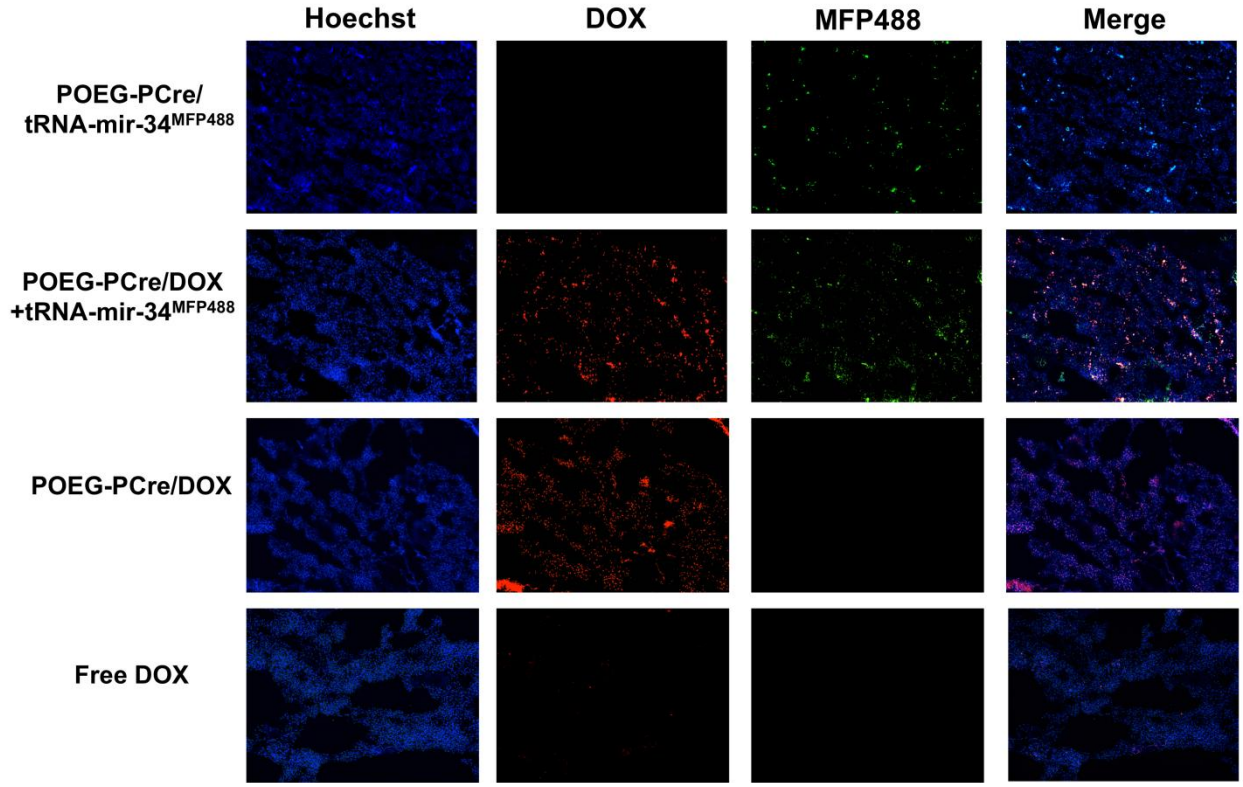

Figure 5-10. Biodistribution of nanocomplexes in tumor-bearing lungs. Balb/c mice bearing 4T1.2 lung metastatic tumors were i.v. injected with DOX+tRNA-mir-34a^{MFP488}/POEG-PCre nanocomplexes.

Fluorescent signals in tumor-bearing lungs were examined after 1 h. The experiments were repeated three times.

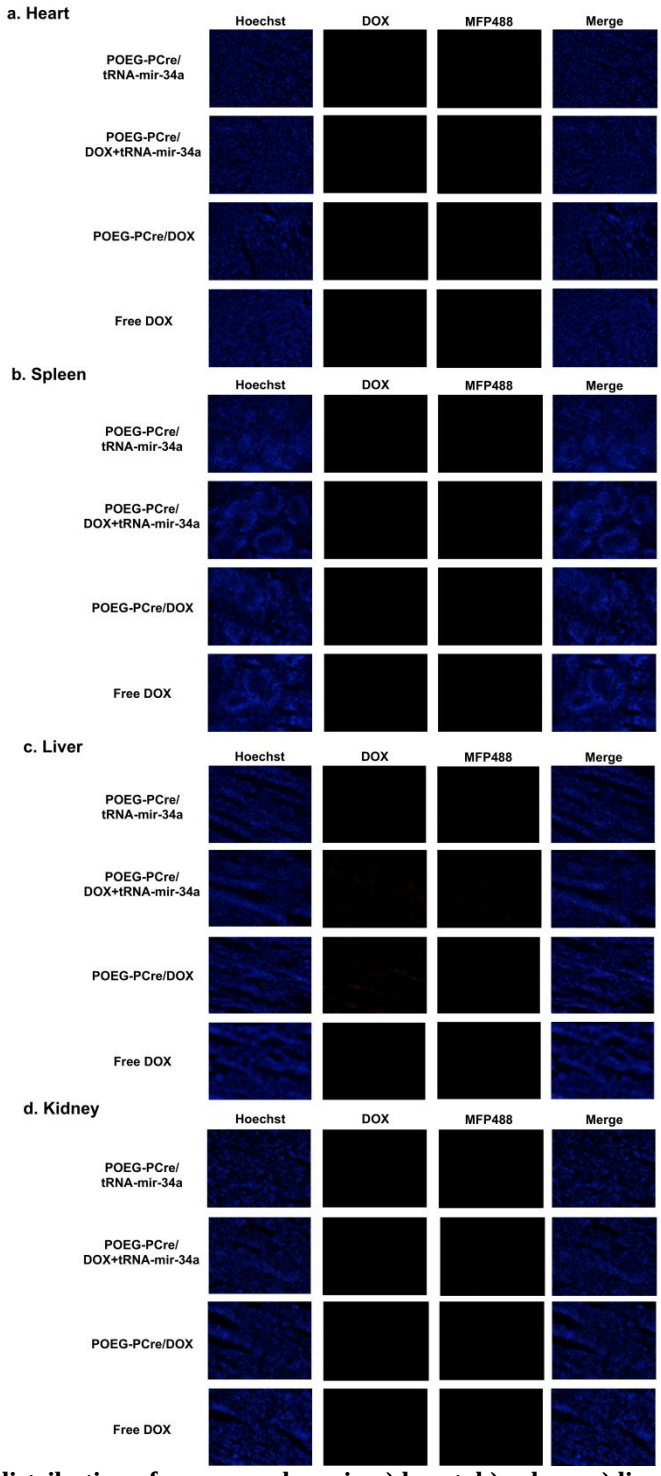

Figure 5-11. Biodistribution of nanocomplexes in a) heart, b) spleen, c) liver and d) kidney.

Balb/c mice bearing 4T1.2 lung metastatic tumors were i.v. injected with DOX+tRNA-mir-34aMFP488/POEG-PCre nanocomplexes. Fluorescent signals in major organs were examined after 1 h. The experiments were repeated three times.

5.4.7 *In Vivo* Therapeutic Study

The *in vivo* anti-tumor efficacy of DOX+tRNA-mir-34a co-loaded nanocomplexes was evaluated in a breast cancer lung metastasis model, generated by tail-vein injection of 4T1.2 tumor cells into female Balb/c mice. Five days after tumor inoculation, various treatments were applied to each group of mice (n=5) via i.v. administration every 3 days for 3 times (Figure 5-12a). The tumor burdens in the lungs were analyzed 5 days after the last treatment. As shown in Figure 5-12b, c and h, tRNA-MSA loaded in POEG-PCre micelles showed negligible therapeutic effect compared to the control group. tRNA-mir-34a/POEG-PCre nanocomplexes exhibited a moderate inhibition of lung metastasis ($P<0.05$). Dramatic reduction in the number of tumor nodules in lungs was found in groups treated with free DOX, DOX/POEG-PCre or DOX+tRNA-MSA/POEG-PCre micelles. More importantly, POEG-PCre micelles co-loaded with DOX and tRNA-mir-34a was significantly superior to all other treatments in the inhibition of 4T1.2 tumor metastasis.

Figure 5-12e showed that the levels of mature miR-34a was significantly and selectively upregulated in tumors treated with tRNA-mir-34a loaded micelles. In consistency to *in vitro* data, codelivery of tRNA-mir-34a and DOX via POEG-PCre micelles led to a further increase in the amounts of mature miR-34a likely due to the upregulation of Dicer expression by DOX-containing formulations in vivo (Figure 5-13). Figure 5-12f, g showed that the expression levels of Bcl-2 in tumor tissues were significantly suppressed at both mRNA and protein levels following treatment with tRNA-mir-34a, particularly for the co-loaded formulation. To further evaluate the anticancer efficacy, H&E staining and immunohistochemical analysis of Ki67 were performed in tumor-bearing lungs. As shown in Figure 5-12i, H&E staining of lung tissues

showed clearly infiltration of tumor cells (with large nuclei) in all of the groups except the DOX/tRNA-mir-34a co-delivery group. In addition, DOX/tRNA-mir-34a co-delivery group showed the lowest number of Ki67-positive tumor cells (Figure 5-12j). Together, the above data clearly demonstrate a synergy between DOX and tRNA-mir-34a in the overall antitumor activity in the lung metastasis model.

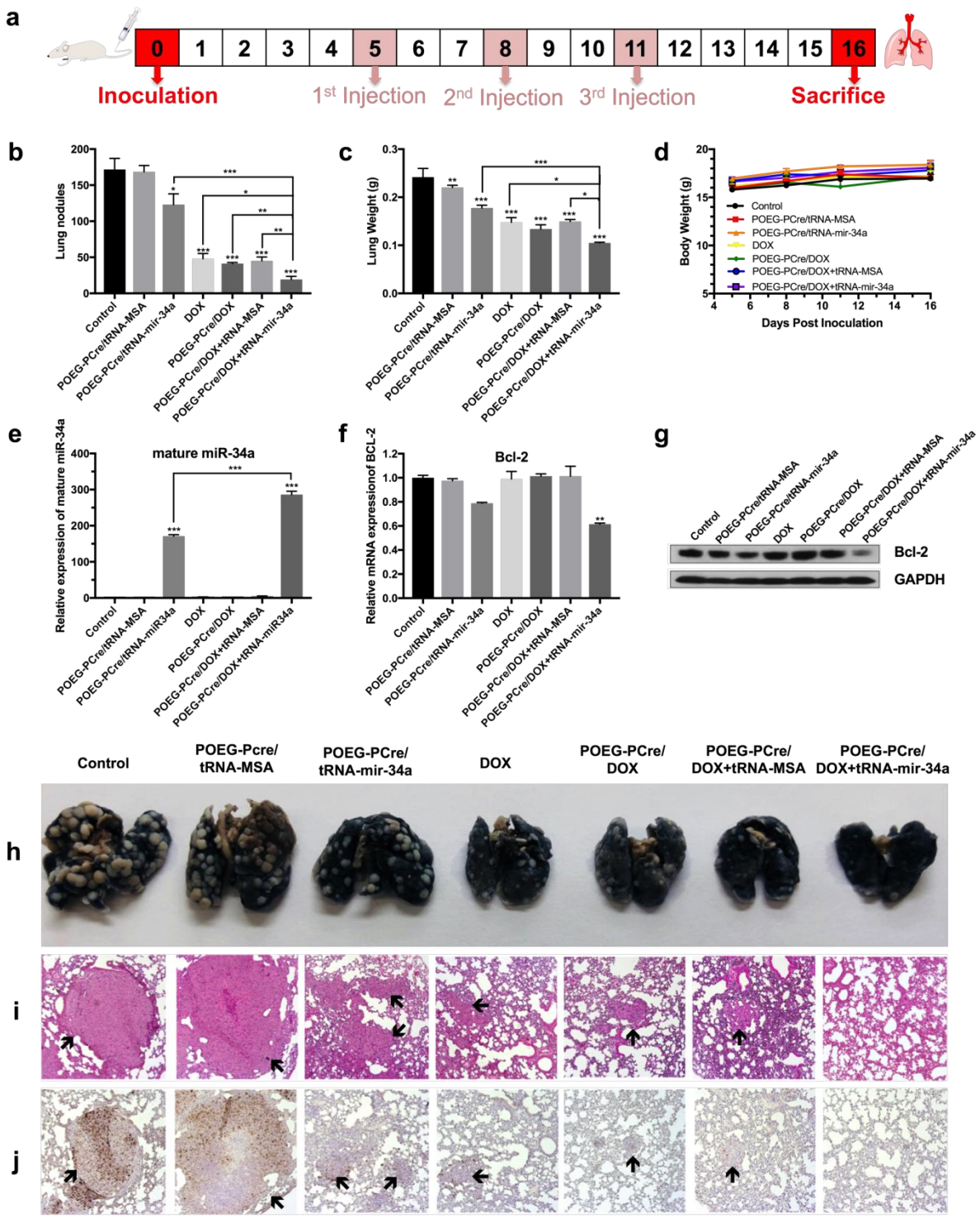

Figure 5-12. Synergistic antitumor activity of tRNA-mir-34a and DOX co-delivered by POEG-PCre micelles in a mouse model of breast cancer (4T1.2) lung metastasis.

a) Experimental scheme for the establishment of lung metastasis and treatment. b-c) Quantification of tumor nodules (b) and lung weights (c). d) Changes in mouse body weights during the treatment period. e-f) Quantification of

mature miR-34a (e) and Bcl-2 mRNA (f) in tumor-bearing lungs by RT-PCR. g) Bcl-2 protein level was evaluated by Western blot. h) Representative images of lungs collected from mice receiving various treatments. i-j) H&E (i) and Ki67 (j) staining of lung tissues. Data are means ± SEM (n=5). P values were generated by one-way ANOVA using the Tukey test for multiple comparisons. *P < 0.05, **P < 0.01, ***P < 0.001.

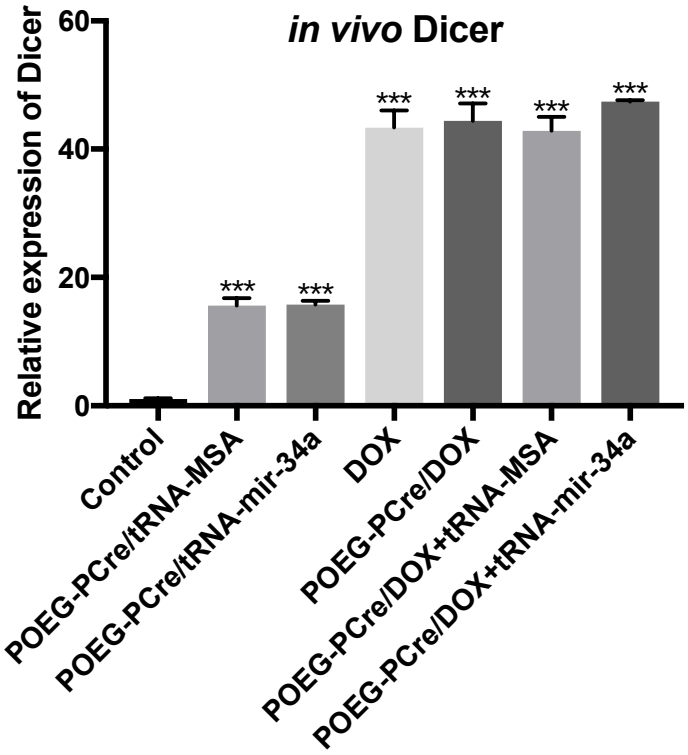

Figure 5-13. Quantification of Dicer mRNA expression in tumor-bearing lungs harvested the end of *in vivo* therapeutic study by RT-PCR.

Data are means ± SEM (n=5). P values were generated by one-way ANOVA using the Dunnett test for multiple comparisons to one control. ***P < 0.001.

5.4.8 Safety Profile

Compared to control or monotherapy, co-delivery of DOX and tRNA-mir-34a did not cause loss of body weight (Figure 5-12d) or any other signs of stress such as hunched posture and labored movement. In addition, blood chemistry tests were performed to evaluate the effect of our formulations on liver and kidney functions. As shown in Figure 5-14a-c, none of the

measured blood biomarkers including alanine aminotransferase (ALT), aspartate aminotransferase (AST) and creatinine were significantly altered by our therapies, indicating the absence of hepatic and renal toxicity. Moreover, the H & E staining of major organs was carried out to further evaluate the potential toxicity of different treatments. As shown in Figure 5-14d, there were signs of myocytolysis and myofibrillolysis with fibrils dearrangement in the heart sections in free DOX group. In addition, hepatocellular vacuolation was found in this group, suggesting possible cardiac and liver toxicities despite no significant alterations in ALT and AST levels. In contrast, no significant pathological changes were observed in the major organs in the groups treated with single-loaded or co-loaded nanocomplexes. These results suggested that POEG-PCre based formulations were well tolerated at the doses tested.

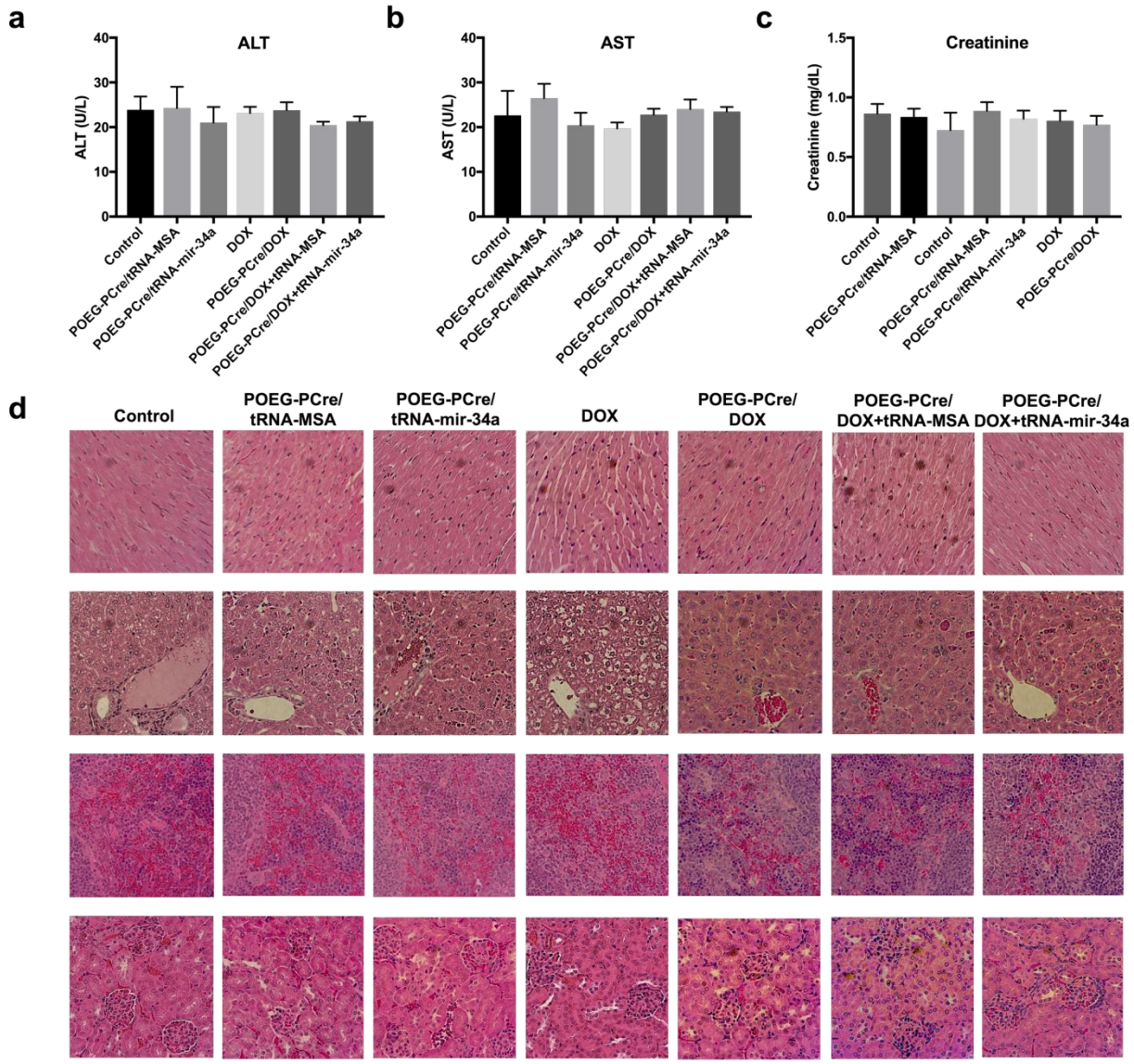

Figure 5-14. Safety profile of tRNA-mir-34a and DOX codelivered by POEG-PCre micelles in a mouse model.

a-c) ALT (a), AST (b) and creatinine (c) level detected at the end of therapy. (d) H & E staining of major organs harvested at the end of therapy. Data are means ± SEM (n=5).

5.4.9 Immune Cell Infiltration Profile in Tumor-Bearing Lungs

Figure 5-15a, b and g showed that DOX treatment led to a significant increase in the numbers of CD4 and CD8 cells in the tumor-bearing lungs. DOX treatment also led to an

increase in the numbers of functional CD8 (IFN-γ+ CD8) cells (Figure 5-15c, h). However, the above changes were much more significant following the tRNA-mir-34a/DOX combination treatment (Figure 5-15a-c, g, h). Treatment with tRNA-mir-34a alone or tRNA-mir-34a/DOX combination reduced the numbers of PD1+ CD8 cells (Figure 5-15d, i) and T-regulatory cells (Tregs) (Figure 5-15e, j). Figure 5-15f and k show that the numbers of MDSC were significantly decreased following the tRNA-mir-34a/DOX combination treatment. There was a trend of decreases in the numbers of MDSC following the treatment with DOX alone.

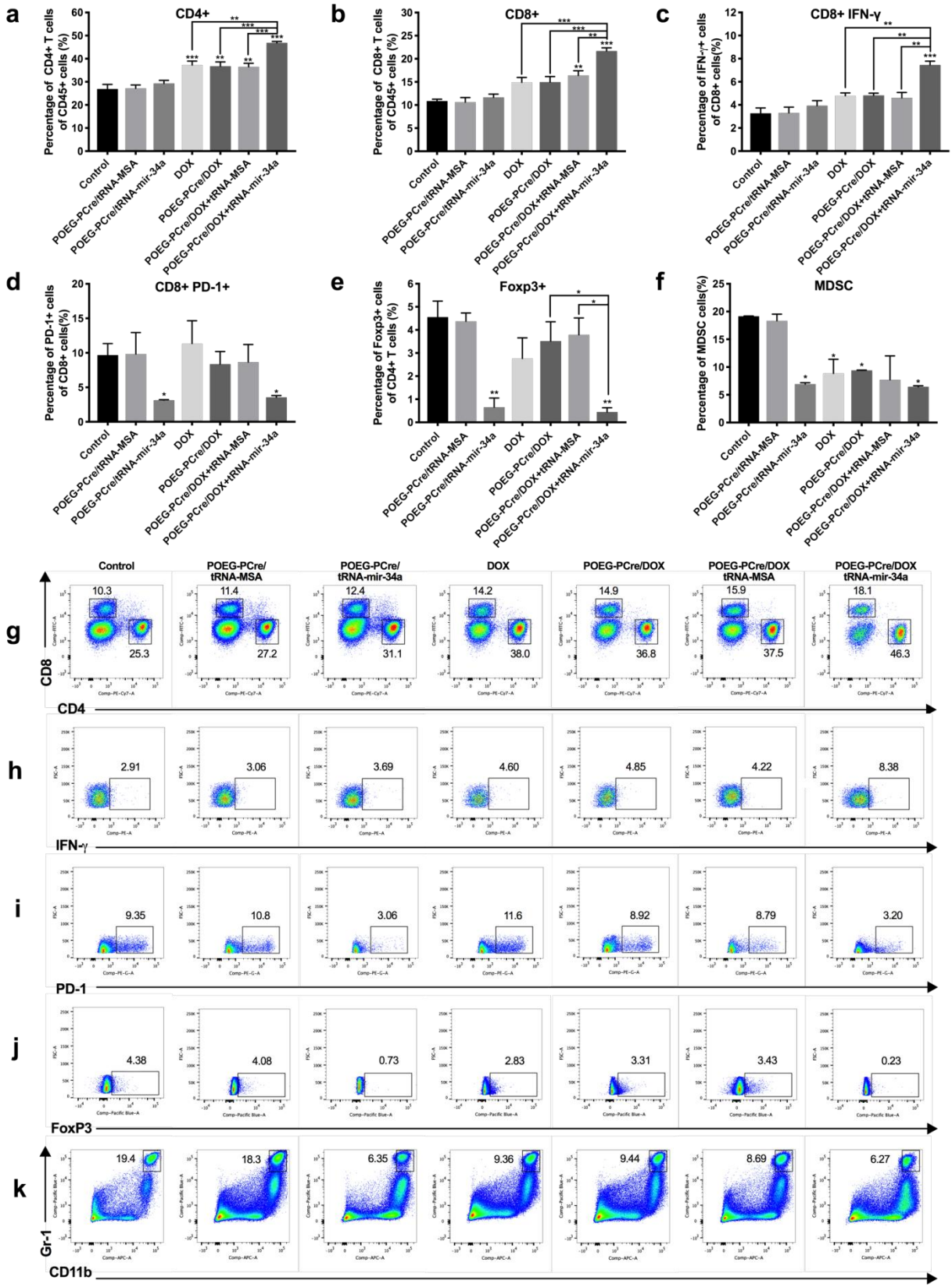
a
CD4+
Percentage of CD4+ T cells of CD45+ cells (%)
b
CD8+
Percentage of CD8+ T cells of CD45+ cells (%)
c
CD8+ IFN-γ
Percentage of IFN-γ+ cells of CD8+ cells(%)
d
CD8+ PD-1+
Percentage of PD-1+ cells of CD8+ cells(%)
e
Foxp3+
Percentage of Foxp3+ cells of CD4+ T cells (%)
f
MDSC
Percentage of MDSC cells(%)
Control
POEG-PCre/tRNA-MSA
POEG-PCre/tRNA-mir-34a
DOX
POEG-PCre/DOX
POEG-PCre/DOX+tRNA-MSA
POEG-PCre/DOX+tRNA-mir-34a
g
CD8
CD4
10.3
25.3
11.4
27.2
12.4
31.1
14.2
38.0
14.9
36.8
15.9
37.5
18.1
46.3
h
IFN-γ
2.91
3.06
3.69
4.60
4.85
4.22
8.38
i
PD-1
9.35
10.8
3.06
11.6
8.92
8.79
3.20
j
FoxP3
4.38
4.08
0.73
2.83
3.31
3.43
0.23
k
Gr-1
CD11b
19.4
18.3
6.35
9.36
9.44
8.69
6.27

Figure 5-15. Flow analysis of infiltration of immune cells in tumor-bearing lungs following various treatments.

Balb/c mice were injected with $2*10^5$ 4T1.2 cells via tail vein. Five days later, mice were treated with tRNA-MSA/POEG-PCre, tRNA-mir-34a/POEG-PCre, free DOX, DOX/POEG-PCre, DOX+tRNA-MSA /POEG-PCre and DOX+tRNA-mir-34a/POEG-PCre respectively for three times. T lymphocyte subsets isolated from lung tissues with 4T1.2 metastasis was analyzed by flow cytometry. a-f) The percentage of $CD4^+$ (a), $CD8^+$ (b), IFN-γ positive intratumoural CD8 T cells (c), PD-1 positive intratumoural CD8 T cells (d), FoxP3+ Treg cells (e) and MDSC cells (f) in tumor-bearing lungs were detected by flow cytometry. g-k) Flow cytometry gating and representative figures of $CD4^+$ and $CD8^+$ (g), IFN-γ positive intratumoural CD8 T cells (h), PD-1 positive intratumoural CD8 T cells (i), FoxP3+ Treg cells (j) and CD11b+/Gr-1+ MDSC cells (k). The results are shown as the means ± SEM with 3 mice in each group. The experiments were repeated two times. P values were generated by one-way ANOVA using the Tukey test for multiple comparisons. *P < 0.05, **P < 0.01, ***P < 0.001.

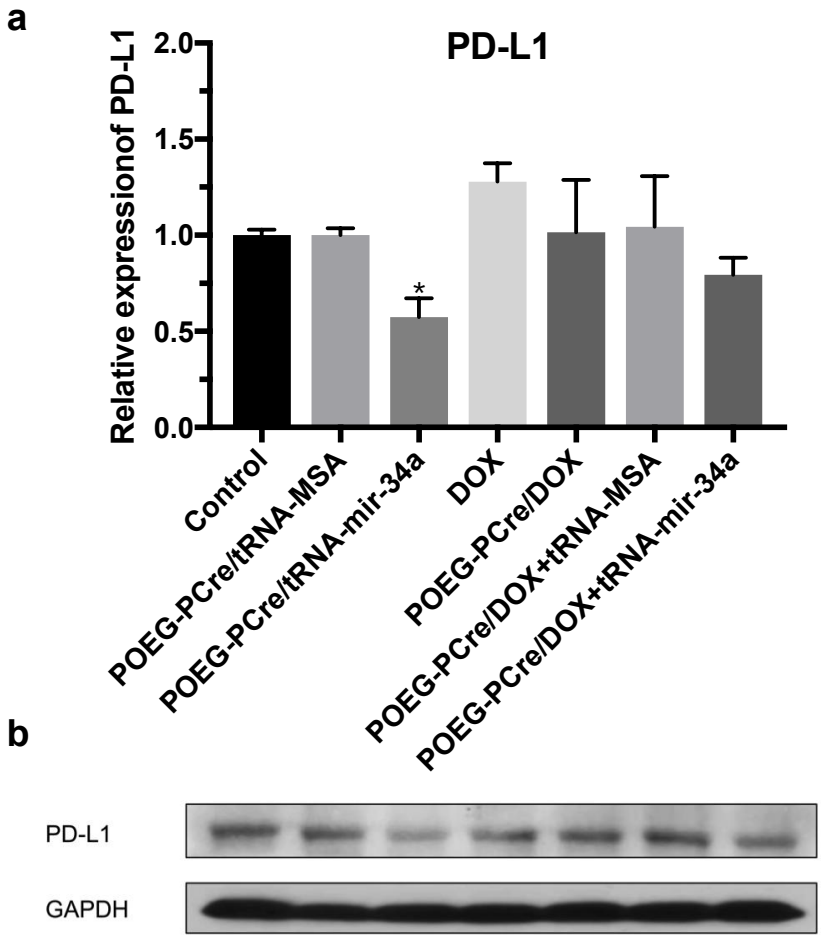

Figure 5-16. PD-L1 mRNA and protein expression in tumor-bearing lungs harvested the end of *in vivo* therapeutic study.

a) Quantification of PD-L1 mRNA expression in tumor-bearing lungs harvested the end of *in vivo* therapeutic study by RT-PCR. Data are means ± SEM (n=5). P values were generated by one-way ANOVA using the Dunnett test for multiple comparisons to one control. *P < 0.05. **b)** PD-L1 protein level was evaluated by Western blot.

5.5 Discussion

We have developed a novel co-delivery system for DOX and miR-34a, which is based on a natural and endogenous cationic molecule—creatine. A primary function of creatine is to facilitate recycling of ATP primarily in muscle and brain tissues; therefore it is widely used by

athletes as an ergogenic aid to enhance anaerobic exercise performance[206]. Typically, creatine is produced endogenously or obtained through the diet at a rate of 1 g per day in young adult[207]. Excess amounts of creatine could be metabolized to creatinine and excreted through kidney[208]. Our carrier is a polymeric system in which creatine was post-conjugated to the polymer backbone via ester bond. The biodegradability of the polymer and the nontoxic nature of creatine may account for the excellent safety profile of our new nanocarrier as shown in Figure 5-12d and Figure 5-14. We further improved our DOX/miR-34a combination therapy via employing a bioengineered miR-34a prodrug that will be processed into mature miR-34a upon intracellular delivery. Currently miRNA replacement therapy is limited to the use of synthetic RNAs that are chemically modified to improve their stability[209]. Such modifications may alter the folding, biologic activities, and more importantly the safety profiles, such as the proinflammatory cytokine response.[210] In contrast, bioengineered miR-34a prodrug is folded in living cells, which may better maintain the functions and safety properties of natural miR-34a[188].

Besides the favorable safety, our creatine-based nanocarrier is also noted for its ability in co-delivery of both small molecule drugs and nucleic acid-based therapeutics. Generally, most chemotherapeutic drugs are poorly water-soluble, while miRNAs are polyanionic molecules with high water-solubility, instability and high molecular weight[211]. Most carriers reported so far are designed for delivery of either small molecule drugs or nucleic acid therapeutics alone[52, 53]. Some carriers were developed for codelivery of the two different types of therapeutics but they often involved complicated preparation process[54]. POEG-PCre represents a simple nanocarrier for effective co-loading of small molecule drugs and nucleic acids-based therapeutics. POEG-PCre readily self-assembles to form a hydrophobic core that allows

effective loading of hydrophobic drugs such as DOX. At the same time, the multiple positive charges from creatine at the interface of the POEG-PCre micelles facilitate the interaction with the negatively charged nucleic acids. Interestingly, the multivalent charge-charge interactions between the cationic polymer and nucleic acids may also serve as a simple approach to cross-link and stabilize the micelles[212, 213]. As a result, the size of tRNA-mir-34a complexed micelles (~120 nm) was much smaller than that of blank micelles or DOX-loaded micelles (~180 nm) (Figure 5-3a). In addition, DOX/tRNA-mir-34a-coloaded nanoparticles exhibited a slightly slower release kinetics compared to that of micelles loaded with DOX only (Figure 5-3f).

Complexation of cationic polymers with large-sized nucleic acids such as plasmid DNA is known to lead to formation of compact particles, which involves structure arrangement and condensation of DNA[214]. On the other hand, cationic polymers tend to form loose complexes with short oligonucleotides due to their small lengths[215]. Accordingly, our POEG-PCre polymer readily formed stable complexes with plasmid DNA at N/P ratios above 2.5 but failed to do so with short siRNA at N/P ratio as high as 80 (Figure 5-4). Interestingly, tRNA-mir-34a appears to have an appropriate size (~ 200 nt) to form stable complexes with POEG-PCre polymer. It should be noted that POEG-PCre/tRNA-mir-34a complexes were more stable than PEI/tRNA-mir-34a complexes as evidenced by the fact that tRNA-mir-34a in POEG-PCre/tRNA-mir-34a complexes was more resistant to the replacement by the negatively charged dextran sulphate compared to PEI/tRNA-mir-34a (Figure 5-3d). This is likely due to additional mechanisms of interactions between POEG-PCre and nucleic acids in addition to charge interactions.[216] The backbone of POEG-PCre consists of hydrophobic alkyl main chains and pendent benzyl rings that can interact with the base π-systems of nucleic acids through

hydrophobic interaction and π–π stacking[217]. The enhanced interaction of our polymer with nucleic acids may help to improve the stability of polymer/nucleic acid complexes in the blood circulation.

POEG-PCre was highly effective in mediating codelivery of tRNA-mir-34a and DOX to cultured tumor cells *in vitro* and pulmonary circulation *in vivo*. Creatine is a derivative of the guanidinium cation. Positively charged guanidinium group is able to form electrostatic association and bidentate hydrogen bond with anionic cell surface phosphates, carboxylates and/or sulfates to initiate the event of cellular entry[218]. This feature has been widely utilized to design several new guanidinium-rich transporter scaffolds to improve the performance of cell penetration for small molecules, peptides and genes[219]. The efficient intracellular delivery of tRNA-mir-34a and DOX (Figure 5-5) shall likely benefit from this multivalent effect. Following systemic administration, the creatine-based polymer may take advantage of the lung-enriched polyamine transporters to guide the targeted accumulation of nanocomplexes to lung tissues[198]. Indeed, a more predominant distribution of the nanocomplexes in the lungs was observed (Figure 5-10, Figure 5-11), which should be beneficial to the prevention and treatment of lung metastasis.

Codelivery of DOX and tRNA-mir-34a via POEG-PCre-based nanoparticles led to an enhanced combinational effect both *in vitro* and *in vivo*. It is interesting to note that codelivery of DOX facilitates the processing of tRNA-mir-34a, resulting in increased levels of mature miR-34a ($P<0.001$) (Figure 5-6a). The underlying mechanism is not clearly understood; however, our data suggest that DOX induced the expression of RNase III enzyme Dicer (Figure 5-7). It has

been reported that Dicer is required for activating the DNA damage response when double-strand DNA breaks and non-coding RNA is synthesized at the site of DNA damage[220]. Therefore, DOX may enhance the expression of Dicer through the DNA damage response. More studies are needed to better understand the underlying mechanism for the DOX-mediated enhancement of tRNA-mir-34a processing.

The improved antitumor activity of DOX/tRNA-mir-34a-based therapy is likely attributed to various factors. Overexpression of miR-34a is effective in inhibiting the proliferation of cancer cells and inducing apoptosis. In addition, miR-34a sensitizes cancer cells to chemotherapeutic agents such as DOX. Our data further suggest a role of immune response in the overall antitumor activity of DOX/tRNA-mir-34a combination therapy. DOX was reported to trigger immunogenic cell death by promoting tumor infiltration of IL-17-secreting γδ T cells and enhancing the proliferation and activation of IFNγ-secreting CD8+ T cells in tumor draining lymph nodes[221]. Similar results were shown in our studies with a lung metastatic tumor model. However, treatment with DOX+tRNA-mir-34a co-loaded nanocomplexes resulted in even greater numbers of tumor-infiltrating CD4+, CD8+ and CD8+ IFN-γ^+ $CD8^+$ T cells (Figure 5-15), which may be attributed to the effect of miR-34a on the down-regulation of PD-L1 expression (Figure 5-16). In addition, the co-treatment led to significantly reduced numbers of MDSCs that are highly immunosuppressive and play an important role in suppressing the antitumor immunity. Therefore, our combination therapy helps to create an active tumor immune microenvironment that likely contributes to the overall antitumor activity.

In summary, we have developed a novel nanocarrier (POEG-PCre) for co-delivery DOX and bioengineered miR-34a prodrug, based on the built-in blocks of naturally occurring cationic

molecule—creatine. Stable and nanosized micelles co-loaded with DOX and tRNA-mir-34a could be readily prepared and were highly effective in targeted delivery of payloads to lungs. Significantly improved antitumor activity was demonstrated with codelivery of DOX and miR-34a prodrug in comparison with other control groups in a 4T1.2 lung metastasis model. POEG-PCre may represent a simple and effective delivery system for an optimal chemo-gene combination therapy.

6.0 Summary and Perspectives

During my graduate study, I worked on several projects to develop multi-functional nanomicellar system for the combinational co-delivery of anticancer agents. We first improved our previous PEG-FTS conjugates dual-functional micellar system, through the incorporation of both reduction-responsive disulfide bond and drug-interactive motif Fmoc, to form a simple PEG_{5k}-Fmoc-S-S-FTS_2 system. Compared with PEG_{5k}-Fmoc-FTS_2, our novel system exhibited further strengthened drug loading capacity and colloidal stability. More FTS was freed from PEG_{5k}-Fmoc-S-S-FTS_2 in treated tumor cells compared to PEG_{5k}-Fmoc-FTS_2. After loading Paclitaxel (PTX) into PEG_{5k}-Fmoc-S-S-FTS_2 micelles, it showed more potent efficiency in inhibition of 4T1.2 tumor cell proliferation *in vitro* and *in vivo* than Taxol® and PTX-loaded PEG_{5k}-Fmoc-FTS_2.

In order to increase the drug content from the prodrug-based carrier, we modified the structure and synthesis route of prodrug-based nanocarrier, from the conjugation of limited amount of hydrophobic drug with PEG to the polymerization of drug-based monomer. The increased units of hydrophobic drugs in each prodrug polymer could not only decrease the amounts of carrier materials in *in vivo* application by increase the drug loading capacity and micelle stability, but also provide better synergistic effect with loaded anticancer drugs. We applied this strategy to other two targeted therapeutics: PPMP (GCS inhibitor) and SAHA (HDAC inhibitor), and developed POEG-*b*-PPPMP and POEG-*b*-PSAHA respectively. $POEG_{15}$-*b*-$PPPMP_7$ consists of 7 units of PPMP and well retained the biological ability of PPMP. Combination of DOX with POEG-*b*-PPPMP led to inhibition of DOX-induced upregulation of GCS, increased accumulation of pro-apoptotic ceramides, and enhanced cytotoxicity towards

tumor cells. More importantly, systemic administration of DOX formulated in POEG-*b*-PPPMP micelles resulted in significant inhibition of 4T1.2 breast tumor, much more effectively than Doxil and POEG-*b*-POM/DOX.

POEG-*b*-PSAHA prodrug micellar nanocarrier consists of a hydrophobic segment composed of 12 SAHA-based units, and a POEG hydrophilic segment for efficient entrapment of DOX. Our POEG-*b*-PSAHA prodrug micelles well retained the biological activity of SAHA in inhibiting the proliferation of tumor cells and promoting the acetylation of histone H3 and H4. More importantly, *in vivo* delivery of DOX via POEG-*b*-PSAHA led to significant inhibition of 4T1.2 tumor, much more effectively than DOX.HCl, Doxil and DOX/POEG-*b*-POM.

To further improve the combination cancer therapy, we developed multifunctional cationic polymer for the co-delivery of small molecule drugs (for known targets) and nucleic acid therapeutics (for "undruggable" targets). we have developed POEG-PCre cationic polymer for co-delivery DOX and bioengineered miR-34a prodrug, based on the built-in blocks of naturally occurring cationic molecule—creatine. Significantly improved antitumor activity was demonstrated with codelivery of DOX and miR-34a prodrug in comparison with other control groups in a 4T1.2 lung metastasis model. POEG-PCre may represent a simple and effective delivery system for an optimal chemo-gene combination therapy.

Although the biophysical property and antitumor efficacy of multifunctional nanocarriers for combination cancer therapy has improved progressively by the continuous creation and modification from previous systems, there still some issues remain unsolved.

Firstly, Despite the passive targeting of nanoparticles to the tumor tissues, the majority of nanoparticles were still cleared by the RES system, resulting in short half-lives and unwanted micelle deposition in the liver and spleen. More accumulation of nanoparticles to the tumor sites

could be achieved by coating active targeting ligand to the surface of the micelles, such as folic acid[222], transferrin[223], RGD[224], whose receptors are highly expressed on tumor cells compared to normal cells. These modifications can potentially increase the targeting of micelles to tumor sites, as well as boost the binding to cells and subsequent internalization. Alternatively, stimuli-responsive polymeric micelles offer promising opportunities to trigger the micellar dissociation and drug release at tumor sites in response to specific external or internal stimuli, such as temperature, pH, ultrasound or enzymes, by including thermo- or pH-sensitive components.

In addition, the size of polymeric micelles developed in my graduate research is still relatively large (60~200 nm). Further decrease the size of nanoparticles might contribute to better tumor penetration. It has been reported that the accumulation of sub-100 nm polymeric micelles in poorly permeable tumors largely depended on size, with only 30 nm micelles could penetrate tumors with hypovascular and hypopermeable characteristics (such as intractable pancreatic tumors)[225]. To further reduce the size of nanomicelles, the effort might be made to decrease the ratio of hydrophobic segment in the polymer molecule. However, more subtle modification is demanded to keep the balance between the smaller size and lower drug loading capacity.

Moreover, in spite of shielding by PEG, there are a significant number of unanswered questions related to micelle stability. Generally, the overall stability of micelles formulation is suboptimal compared to other formulations. Crosslinking the core or the corona might be a promising strategy to enhance the colloid stability. Besides, our micelles were not fully evaluated in physiologically relevant media but only in water or aqueous buffer, which limited the predictability of the *in vitro* assay to the complex *in vivo* microenvironment. More stability

related tests should be done in serum, major protein constituents (e.g. albumin, globulins), blood or cells. Additional questions relate to micelle stability during freeze-drying and re-constitution. These impact scalability and development of micelles for clinical use. Selection of suitable lyoprotectants and optimization of freeze-dry process cycles might be helpful to enhance the stability during the formulation and storage.

Furthermore, due to limited time, sophisticated design and systemic optimization of each system was not fully explored before moving to the pharmacologic evaluation. More systematic studies on the structure-activity relationship of polymeric micellar systems are needed to better understand the mechanism of drug-carrier interaction and establish a stable micellar system with a high drug loading capacity.

Last but not least, all systems developed in my graduate study have not been evaluated in human tumor cell line xenograft model or patient-derived xenograft (PDX) cancer models, which might compromise the translation from preclinical into clinical study[226, 227]. In addition, survival studies should also be performed to better evaluate therapeutic benefit of our systems. the These studies shall lead to the development of further improved micellar systems with potential for rapid translation into clinical study to advance the treatment of cancers.

Bibliography

[1] S. Garattini, New approaches to cancer therapy, Annals of Oncology 14(6) (2003) 813-816.
[2] R. Bayat Mokhtari, T.S. Homayouni, N. Baluch, E. Morgatskaya, S. Kumar, B. Das, H. Yeger, Combination therapy in combating cancer, Oncotarget 8(23) (2017) 38022-38043.
[3] J.A. DiMasi, R.W. Hansen, H.G. Grabowski, The price of innovation: new estimates of drug development costs, Journal of health economics 22(2) (2003) 151-85.
[4] L. Ma, M. Kohli, A.J.A.n. Smith, Nanoparticles for combination drug therapy, 7(11) (2013) 9518-9525.
[5] N. Kolishetti, S. Dhar, P.M. Valencia, L.Q. Lin, R. Karnik, S.J. Lippard, R. Langer, O.C.J.P.o.t.N.A.o.S. Farokhzad, Engineering of self-assembled nanoparticle platform for precisely controlled combination drug therapy, 107(42) (2010) 17939-17944.
[6] D.J.N.b. Lane, Designer combination therapy for cancer, 24(2) (2006) 163.
[7] M. Maemondo, A. Inoue, K. Kobayashi, S. Sugawara, S. Oizumi, H. Isobe, A. Gemma, M. Harada, H. Yoshizawa, I.J.N.E.J.o.M. Kinoshita, Gefitinib or chemotherapy for non–small-cell lung cancer with mutated EGFR, 362(25) (2010) 2380-2388.
[8] J. Zhang, P.L. Yang, N.S.J.N.r.c. Gray, Targeting cancer with small molecule kinase inhibitors, 9(1) (2009) 28.
[9] V. Wagner, A. Dullaart, A.-K. Bock, A. Zweck, The emerging nanomedicine landscape, Nature biotechnology 24 (2006) 1211.
[10] R.K. Jain, T. Stylianopoulos, Delivering nanomedicine to solid tumors, Nature Reviews Clinical Oncology 7 (2010) 653.
[11] O.C. Farokhzad, R. Langer, Impact of Nanotechnology on Drug Delivery, ACS Nano 3(1) (2009) 16-20.
[12] H. Maeda, The enhanced permeability and retention (EPR) effect in tumor vasculature: the key role of tumor-selective macromolecular drug targeting, Advances in Enzyme Regulation 41(1) (2001) 189-207.
[13] Y.H. Bae, K. Park, Targeted drug delivery to tumors: Myths, reality and possibility, Journal of Controlled Release 153(3) (2011) 198-205.
[14] T. Lammers, F. Kiessling, W.E. Hennink, G. Storm, Drug targeting to tumors: Principles, pitfalls and (pre-) clinical progress, Journal of Controlled Release 161(2) (2012) 175-187.
[15] L.D. Mayer, T.O. Harasym, P.G. Tardi, N.L. Harasym, C.R. Shew, S.A. Johnstone, E.C. Ramsay, M.B. Bally, A.S.J.M.c.t. Janoff, Ratiometric dosing of anticancer drug combinations: controlling drug ratios after systemic administration regulates therapeutic activity in tumor-bearing mice, 5(7) (2006) 1854-1863.
[16] J. Sun, Y. Liu, Y. Chen, W. Zhao, Q. Zhai, S. Rathod, Y. Huang, S. Tang, Y.T. Kwon, C. Fernandez, R. Venkataramanan, S. Li, Doxorubicin delivered by a redox-responsive dasatinib-containing polymeric prodrug carrier for combination therapy, Journal of Controlled Release 258 (2017) 43-55.
[17] U. Kedar, P. Phutane, S. Shidhaye, V. Kadam, Advances in polymeric micelles for drug delivery and tumor targeting, Nanomedicine: Nanotechnology, Biology and Medicine 6(6) (2010) 714-729.

[18] V.P. Torchilin, Structure and design of polymeric surfactant-based drug delivery systems, Journal of Controlled Release 73(2) (2001) 137-172.
[19] J. Deng, N. Gao, Y. Wang, H. Yi, S. Fang, Y. Ma, L. Cai, Self-Assembled Cationic Micelles Based on PEG-PLL-PLLeu Hybrid Polypeptides as Highly Effective Gene Vectors, Biomacromolecules 13(11) (2012) 3795-3804.
[20] B. Jeong, Y. Han Bae, S. Wan Kim, Biodegradable thermosensitive micelles of PEG-PLGA-PEG triblock copolymers, Colloids and Surfaces B: Biointerfaces 16(1) (1999) 185-193.
[21] Y. Nagasaki, T. Okada, C. Scholz, M. Iijima, M. Kato, K. Kataoka, The Reactive Polymeric Micelle Based on An Aldehyde-Ended Poly(ethylene glycol)/Poly(lactide) Block Copolymer, Macromolecules 31(5) (1998) 1473-1479.
[22] V.S. Trubetskoy, V.P. Torchilin, Use of polyoxyethylene-lipid conjugates as long-circulating carriers for delivery of therapeutic and diagnostic agents, Advanced Drug Delivery Reviews 16(2) (1995) 311-320.
[23] A.N. Lukyanov, V.P. Torchilin, Micelles from lipid derivatives of water-soluble polymers as delivery systems for poorly soluble drugs, Advanced Drug Delivery Reviews 56(9) (2004) 1273-1289.
[24] A.N. Lukyanov, Z. Gao, L. Mazzola, V.P. Torchilin, Polyethylene Glycol-Diacyllipid Micelles Demonstrate Increased Accumulation in Subcutaneous Tumors in Mice, Pharmaceutical research 19(10) (2002) 1424-1429.
[25] T. Musacchio, V. Laquintana, A. Latrofa, G. Trapani, V.P. Torchilin, PEG-PE Micelles Loaded with Paclitaxel and Surface-Modified by a PBR-Ligand: Synergistic Anticancer Effect, Molecular pharmaceutics 6(2) (2009) 468-479.
[26] Z. Gao, A.N. Lukyanov, A. Singhal, V.P. Torchilin, Diacyllipid-Polymer Micelles as Nanocarriers for Poorly Soluble Anticancer Drugs, Nano Letters 2(9) (2002) 979-982.
[27] J. Luo, K. Xiao, Y. Li, J.S. Lee, L. Shi, Y.-H. Tan, L. Xing, R. Holland Cheng, G.-Y. Liu, K.S. Lam, Well-Defined, Size-Tunable, Multifunctional Micelles for Efficient Paclitaxel Delivery for Cancer Treatment, Bioconjugate chemistry 21(7) (2010) 1216-1224.
[28] X.-X. Zhu, M. Nichifor, Polymeric Materials Containing Bile Acids, Accounts of Chemical Research 35(7) (2002) 539-546.
[29] Y. Zhao, Facial amphiphiles in molecular recognition: From unusual aggregates to solvophobically driven foldamers, Current Opinion in Colloid & Interface Science 12(2) (2007) 92-97.
[30] K. Xiao, J. Luo, Y. Li, J.S. Lee, G. Fung, K.S. Lam, PEG-oligocholic acid telodendrimer micelles for the targeted delivery of doxorubicin to B-cell lymphoma, Journal of Controlled Release 155(2) (2011) 272-281.
[31] Y. Li, K. Xiao, J. Luo, W. Xiao, J.S. Lee, A.M. Gonik, J. Kato, T.A. Dong, K.S. Lam, Well-defined, reversible disulfide cross-linked micelles for on-demand paclitaxel delivery, Biomaterials 32(27) (2011) 6633-6645.
[32] Y. Li, K. Xiao, J. Luo, J. Lee, S. Pan, K.S. Lam, A novel size-tunable nanocarrier system for targeted anticancer drug delivery, Journal of Controlled Release 144(3) (2010) 314-323.
[33] K. Knop, R. Hoogenboom, D. Fischer, U.S. Schubert, Poly(ethylene glycol) in Drug Delivery: Pros and Cons as Well as Potential Alternatives, 49(36) (2010) 6288-6308.
[34] R.B. Greenwald, Y.H. Choe, J. McGuire, C.D. Conover, Effective drug delivery by PEGylated drug conjugates, Advanced Drug Delivery Reviews 55(2) (2003) 217-250.
[35] G. Pasut, F.M. Veronese, State of the art in PEGylation: The great versatility achieved after forty years of research, Journal of Controlled Release 161(2) (2012) 461-472.

[36] S.R. Croy, G.S. Kwon, Polymeric Micelles for Drug Delivery, Current pharmaceutical design 12(36) (2006) 4669-4684.
[37] Y. Huang, J. Lu, X. Gao, J. Li, W. Zhao, M. Sun, D.B. Stolz, R. Venkataramanan, L.C. Rohan, S. Li, PEG-derivatized embelin as a dual functional carrier for the delivery of paclitaxel, Bioconjugate chemistry 23(7) (2012) 1443-51.
[38] J. Lu, Y. Huang, W. Zhao, Y. Chen, J. Li, X. Gao, R. Venkataramanan, S. Li, Design and characterization of PEG-derivatized vitamin E as a nanomicellar formulation for delivery of paclitaxel, Molecular pharmaceutics 10(8) (2013) 2880-90.
[39] X. Zhang, J. Lu, Y. Huang, W. Zhao, Y. Chen, J. Li, X. Gao, R. Venkataramanan, M. Sun, D.B. Stolz, L. Zhang, S. Li, PEG-farnesylthiosalicylate conjugate as a nanomicellar carrier for delivery of paclitaxel, Bioconjugate chemistry 24(3) (2013) 464-72.
[40] D. Marciano, G. Ben-Baruch, M. Marom, Y. Egozi, R. Haklai, Y. Kloog, Farnesyl Derivatives of Rigid Carboxylic Acids - Inhibitors of ras-Dependent Cell Growth, Journal of Medicinal Chemistry 38(8) (1995) 1267-1272.
[41] Y. Chen, X. Zhang, J. Lu, Y. Huang, J. Li, S. Li, Targeted delivery of curcumin to tumors via PEG-derivatized FTS-based micellar system, The AAPS journal 16(3) (2014) 600-8.
[42] X. Zhang, Y. Huang, W. Zhao, Y. Chen, P. Zhang, J. Li, R. Venkataramanan, S. Li, PEG-farnesyl thiosalicylic acid telodendrimer micelles as an improved formulation for targeted delivery of paclitaxel, Molecular pharmaceutics 11(8) (2014) 2807-14.
[43] J. Sun, Y. Chen, K. Li, Y. Huang, X. Fu, X. Zhang, W. Zhao, Y. Wei, L. Xu, P. Zhang, R. Venkataramanan, S. Li, A prodrug micellar carrier assembled from polymers with pendant farnesyl thiosalicylic acid moieties for improved delivery of paclitaxel, Acta biomaterialia 43 (2016) 282-291.
[44] H.M. Aliabadi, A.J.E.o.o.d.d. Lavasanifar, Polymeric micelles for drug delivery, 3(1) (2006) 139-162.
[45] V.T. Huynh, P. de Souza, M.H.J.M. Stenzel, Polymeric micelles with pendant dicarboxylato chelating ligands prepared via a michael addition for cis-platinum drug delivery, 44(20) (2011) 7888-7900.
[46] Y. Mi, Y. Liu, S.-S.J.B. Feng, Formulation of docetaxel by folic acid-conjugated D-α-tocopheryl polyethylene glycol succinate 2000 (Vitamin E TPGS2k) micelles for targeted and synergistic chemotherapy, 32(16) (2011) 4058-4066.
[47] J. Li, F. Yu, Y. Chen, D.J.J.o.C.R. Oupický, Polymeric drugs: Advances in the development of pharmacologically active polymers, 219 (2015) 369-382.
[48] J.-Z. Du, X.-J. Du, C.-Q. Mao, J.J.J.o.t.A.C.S. Wang, Tailor-made dual pH-sensitive polymer–doxorubicin nanoparticles for efficient anticancer drug delivery, 133(44) (2011) 17560-17563.
[49] V. Delplace, P. Couvreur, J.J.P.C. Nicolas, Recent trends in the design of anticancer polymer prodrug nanocarriers, 5(5) (2014) 1529-1544.
[50] D. Smith, E.B. Pentzer, S.T.J.J.o.M.S. Nguyen, Part C: Polymer Reviews, Bioactive and therapeutic ROMP polymers, 47(3) (2007) 419-459.
[51] U. Hasegawa, A.J. Van Der Vlies, C. Wandrey, J.A.J.B. Hubbell, Preparation of well-defined ibuprofen prodrug micelles by RAFT polymerization, 14(9) (2013) 3314-3320.
[52] P. Trang, J.F. Wiggins, C.L. Daige, C. Cho, M. Omotola, D. Brown, J.B. Weidhaas, A.G. Bader, F.J. Slack, Systemic Delivery of Tumor Suppressor microRNA Mimics Using a Neutral Lipid Emulsion Inhibits Lung Tumors in Mice, Molecular Therapy 19(6) (2011) 1116-1122.

[53] R. Suzuki, E. Namai, Y. Oda, N. Nishiie, S. Otake, R. Koshima, K. Hirata, Y. Taira, N. Utoguchi, Y. Negishi, S. Nakagawa, K. Maruyama, Cancer gene therapy by IL-12 gene delivery using liposomal bubbles and tumoral ultrasound exposure, Journal of Controlled Release 142(2) (2010) 245-250.
[54] V. Tsouris, M.K. Joo, S.H. Kim, I.C. Kwon, Y.-Y. Won, Nano carriers that enable co-delivery of chemotherapy and RNAi agents for treatment of drug-resistant cancers, Biotechnology Advances 32(5) (2014) 1037-1050.
[55] X. Zhang, K. Liu, Y. Huang, J. Xu, J. Li, X. Ma, S. Li, Reduction-sensitive dual functional nanomicelles for improved delivery of paclitaxel, Bioconjug Chem 25(9) (2014) 1689-96.
[56] X. Zhang, Y. Huang, W. Zhao, H. Liu, R. Marquez, J. Lu, P. Zhang, Y. Zhang, J. Li, X. Gao, R. Venkataramanan, L. Xu, S. Li, Targeted delivery of anticancer agents via a dual function nanocarrier with an interfacial drug-interactive motif, Biomacromolecules 15(11) (2014) 4326-35.
[57] K. Kataoka, A. Harada, Y. Nagasaki, Block copolymer micelles for drug delivery: design, characterization and biological significance, Advanced Drug Delivery Reviews 47(1) (2001) 113-131.
[58] K. Miyata, R.J. Christie, K. Kataoka, Polymeric micelles for nano-scale drug delivery, Reactive and Functional Polymers 71(3) (2011) 227-234.
[59] G.S. Kwon, K. Kataoka, Block copolymer micelles as long-circulating drug vehicles, Advanced Drug Delivery Reviews 16(2–3) (1995) 295-309.
[60] K. Cho, X. Wang, S. Nie, Z.G. Chen, D.M. Shin, Therapeutic nanoparticles for drug delivery in cancer, Clinical cancer research : an official journal of the American Association for Cancer Research 14(5) (2008) 1310-6.
[61] K.S. Soppimath, T.M. Aminabhavi, A.R. Kulkarni, W.E. Rudzinski, Biodegradable polymeric nanoparticles as drug delivery devices, Journal of Controlled Release 70(1–2) (2001) 1-20.
[62] F.M. Veronese, G. Pasut, PEGylation, successful approach to drug delivery, Drug Discovery Today 10(21) (2005) 1451-1458.
[63] X. Zhang, Y. Huang, S. Li, Nanomicellar carriers for targeted delivery of anticancer agents, Therapeutic delivery 5(1) (2014) 53-68.
[64] J. Lu, W. Zhao, Y. Huang, H. Liu, R. Marquez, R.B. Gibbs, J. Li, R. Venkataramanan, L. Xu, S. Li, S. Li, Targeted delivery of Doxorubicin by folic acid-decorated dual functional nanocarrier, Molecular pharmaceutics 11(11) (2014) 4164-78.
[65] J. Lu, Y. Huang, W. Zhao, R.T. Marquez, X. Meng, J. Li, X. Gao, R. Venkataramanan, Z. Wang, S. Li, PEG-derivatized embelin as a nanomicellar carrier for delivery of paclitaxel to breast and prostate cancers, Biomaterials 34(5) (2013) 1591-600.
[66] Y. Zhang, Y. Huang, S. Li, Polymeric micelles: nanocarriers for cancer-targeted drug delivery, AAPS PharmSciTech 15(4) (2014) 862-71.
[67] N.M. Baker, C.J. Der, Cancer: Drug for an 'undruggable' protein, Nature 497(7451) (2013) 577-8.
[68] L. Chin, A. Tam, J. Pomerantz, M. Wong, J. Holash, N. Bardeesy, Q. Shen, R. O'Hagan, J. Pantginis, H. Zhou, J.W. Horner, 2nd, C. Cordon-Cardo, G.D. Yancopoulos, R.A. DePinho, Essential role for oncogenic Ras in tumour maintenance, Nature 400(6743) (1999) 468-72.
[69] D. Hanahan, R.A. Weinberg, The hallmarks of cancer, Cell 100(1) (2000) 57-70.
[70] C.W. Reuter, M.A. Morgan, L. Bergmann, Targeting the Ras signaling pathway: a rational, mechanism-based treatment for hematologic malignancies?, Blood 96(5) (2000) 1655-69.

[71] G.J. Riely, M.L. Johnson, C. Medina, N.A. Rizvi, V.A. Miller, M.G. Kris, M.C. Pietanza, C.G. Azzoli, L.M. Krug, W. Pao, M.S. Ginsberg, A phase II trial of Salirasib in patients with lung adenocarcinomas with KRAS mutations, Journal of thoracic oncology : official publication of the International Association for the Study of Lung Cancer 6(8) (2011) 1435-7.
[72] E. Bustinza-Linares, R. Kurzrock, A.M. Tsimberidou, Salirasib in the treatment of pancreatic cancer, Future oncology (London, England) 6(6) (2010) 885-91.
[73] T. Badar, J.E. Cortes, F. Ravandi, S. O'Brien, S. Verstovsek, G. Garcia-Manero, H. Kantarjian, G. Borthakur, Phase I study of S-trans, trans-farnesylthiosalicylic acid (salirasib), a novel oral RAS inhibitor in patients with refractory hematologic malignancies, Clinical lymphoma, myeloma & leukemia 15(7) (2015) 433-438.e2.
[74] J. Furuse, T. Kurata, N. Okano, Y. Fujisaka, D. Naruge, T. Shimizu, H. Kitamura, T. Iwasa, F. Nagashima, K. Nakagawa, An early clinical trial of Salirasib, an oral RAS inhibitor, in Japanese patients with relapsed/refractory solid tumors, Cancer chemotherapy and pharmacology 82(3) (2018) 511-519.
[75] L. Brulisauer, M.A. Gauthier, J.C. Leroux, Disulfide-containing parenteral delivery systems and their redox-biological fate, Journal of controlled release : official journal of the Controlled Release Society 195 (2014) 147-54.
[76] S. Chakravarthi, C.E. Jessop, N.J. Bulleid, The role of glutathione in disulphide bond formation and endoplasmic-reticulum-generated oxidative stress, EMBO Rep 7(3) (2006) 271-5.
[77] P. Kuppusamy, H. Li, G. Ilangovan, A.J. Cardounel, J.L. Zweier, K. Yamada, M.C. Krishna, J.B. Mitchell, Noninvasive imaging of tumor redox status and its modification by tissue glutathione levels, Cancer research 62(1) (2002) 307-12.
[78] G.K. Balendiran, R. Dabur, D. Fraser, The role of glutathione in cancer, Cell biochemistry and function 22(6) (2004) 343-52.
[79] F.Q. Schafer, G.R. Buettner, Redox environment of the cell as viewed through the redox state of the glutathione disulfide/glutathione couple, Free radical biology & medicine 30(11) (2001) 1191-212.
[80] L.A. Carpino, G.Y. Han, 9-Fluorenylmethoxycarbonyl amino-protecting group, The Journal of Organic Chemistry 37(22) (1972) 3404-3409.
[81] X. Gao, Y. Huang, A.M. Makhov, M. Epperly, J. Lu, S. Grab, P. Zhang, L. Rohan, X.Q. Xie, P. Wipf, J. Greenberger, S. Li, Nanoassembly of surfactants with interfacial drug-interactive motifs as tailor-designed drug carriers, Mol Pharm 10(1) (2013) 187-98.
[82] P. Zhang, Y. Huang, H. Liu, R.T. Marquez, J. Lu, W. Zhao, X. Zhang, X. Gao, J. Li, R. Venkataramanan, L. Xu, S. Li, A PEG-Fmoc conjugate as a nanocarrier for paclitaxel, Biomaterials 35(25) (2014) 7146-56.
[83] J. Lu, W. Zhao, H. Liu, R. Marquez, Y. Huang, Y. Zhang, J. Li, W. Xie, R. Venkataramanan, L. Xu, S. Li, An improved D-alpha-tocopherol-based nanocarrier for targeted delivery of doxorubicin with reversal of multidrug resistance, Journal of controlled release : official journal of the Controlled Release Society 196 (2014) 272-86.
[84] Y. Zhang, Y. Huang, W. Zhao, J. Lu, P. Zhang, X. Zhang, J. Li, X. Gao, R. Venkataramanan, S. Li, Fmoc-conjugated PEG-vitamin E2 micelles for tumor-targeted delivery of paclitaxel: enhanced drug-carrier interaction and loading capacity, The AAPS journal 16(6) (2014) 1282-91.
[85] P. Zhang, J. Lu, Y. Huang, W. Zhao, Y. Zhang, X. Zhang, J. Li, R. Venkataramanan, X. Gao, S. Li, Design and Evaluation of a PEGylated Lipopeptide Equipped with Drug-Interactive Motifs as an Improved Drug Carrier, AAPS J 16(1) (2014) 114-124.

[86] S. Cai, K. Vijayan, D. Cheng, E.M. Lima, D.E. Discher, Micelles of different morphologies--advantages of worm-like filomicelles of PEO-PCL in paclitaxel delivery, Pharmaceutical research 24(11) (2007) 2099-109.
[87] E.P. Holowka, S.K. Bhatia, Drug Delivery: Materials Design and Clinical Perspective, Springer2014.
[88] S. Hait, S. Moulik, Determination of critical micelle concentration (CMC) of nonionic surfactants by donor-acceptor interaction with Iodine and correlation of CMC with hydrophile-lipophile balance and other parameters of the surfactants, J Surfact Deterg 4(3) (2001) 303-309.
[89] X.Z. Shu, Y. Liu, F. Palumbo, G.D. Prestwich, Disulfide-crosslinked hyaluronan-gelatin hydrogel films: a covalent mimic of the extracellular matrix for in vitro cell growth, Biomaterials 24(21) (2003) 3825-3834.
[90] B. Ogretmen, Y.A. Hannun, Biologically active sphingolipids in cancer pathogenesis and treatment, Nature Reviews Cancer 4(8) (2004) 604-616.
[91] S.A. Morad, M.C. Cabot, Ceramide-orchestrated signalling in cancer cells, Nature reviews. Cancer 13(1) (2013) 51-65.
[92] Y.A. Hannun, Functions of Ceramide in Coordinating Cellular Responses to Stress, Science 274(5294) (1996) 1855-1859.
[93] S. Galadari, A. Rahman, S. Pallichankandy, F. Thayyullathil, Tumor suppressive functions of ceramide: evidence and mechanisms, Apoptosis : an international journal on programmed cell death 20(5) (2015) 689-711.
[94] R.T. Dobrowsky, C. Kamibayashi, M.C. Mumby, Y.A. Hannun, Ceramide activates heterotrimeric protein phosphatase 2A, The Journal of biological chemistry 268(21) (1993) 15523-30.
[95] C.E. Chalfant, Z. Szulc, P. Roddy, A. Bielawska, Y.A. Hannun, The structural requirements for ceramide activation of serine-threonine protein phosphatases, Journal of lipid research 45(3) (2004) 496-506.
[96] M. Heinrich, J. Neumeyer, M. Jakob, C. Hallas, V. Tchikov, S. Winoto-Morbach, M. Wickel, W. Schneider-Brachert, A. Trauzold, A. Hethke, S. Schutze, Cathepsin D links TNF-induced acid sphingomyelinase to Bid-mediated caspase-9 and -3 activation, Cell death and differentiation 11(5) (2004) 550-63.
[97] B.J. Pettus, C.E. Chalfant, Y.A. Hannun, Ceramide in apoptosis: an overview and current perspectives, Biochimica et Biophysica Acta (BBA) - Molecular and Cell Biology of Lipids 1585(2) (2002) 114-125.
[98] B.M. Barth, M.C. Cabot, M. Kester, Ceramide-based therapeutics for the treatment of cancer, Anti-cancer agents in medicinal chemistry 11(9) (2011) 911-9.
[99] F. Li, N. Zhang, Ceramide: Therapeutic Potential in Combination Therapy for Cancer Treatment, Current drug metabolism 17(1) (2015) 37-51.
[100] M. Selzner, A. Bielawska, M.A. Morse, H.A. Rudiger, D. Sindram, Y.A. Hannun, P.A. Clavien, Induction of apoptotic cell death and prevention of tumor growth by ceramide analogues in metastatic human colon cancer, Cancer research 61(3) (2001) 1233-40.
[101] T. Stover, M. Kester, Liposomal Delivery Enhances Short-Chain Ceramide-Induced Apoptosis of Breast Cancer Cells, Journal of Pharmacology and Experimental Therapeutics 307(2) (2003) 468-475.
[102] M. Kester, Y. Heakal, T. Fox, A. Sharma, G.P. Robertson, T.T. Morgan, E.I. Altinoglu, A. Tabakovic, M.R. Parette, S.M. Rouse, V. Ruiz-Velasco, J.H. Adair, Calcium phosphate

nanocomposite particles for in vitro imaging and encapsulated chemotherapeutic drug delivery to cancer cells, Nano letters 8(12) (2008) 4116-21.
[103] T.C. Stover, Y.S. Kim, T.L. Lowe, M. Kester, Thermoresponsive and biodegradable linear-dendritic nanoparticles for targeted and sustained release of a pro-apoptotic drug, Biomaterials 29(3) (2008) 359-69.
[104] S. Ganta, A. Singh, P. Kulkarni, A.W. Keeler, A. Piroyan, R.R. Sawant, N.R. Patel, B. Davis, C. Ferris, S. O'Neal, W. Zamboni, M.M. Amiji, T.P. Coleman, EGFR Targeted Theranostic Nanoemulsion for Image-Guided Ovarian Cancer Therapy, Pharmaceutical research 32(8) (2015) 2753-63.
[105] J.A. Shabbits, L.D. Mayer, Intracellular delivery of ceramide lipids via liposomes enhances apoptosis in vitro, Biochimica et Biophysica Acta (BBA) - Biomembranes 1612(1) (2003) 98-106.
[106] S.A. Saddoughi, P. Song, B. Ogretmen, Roles of bioactive sphingolipids in cancer biology and therapeutics, Sub-cellular biochemistry 49 (2008) 413-40.
[107] C.P. Reynolds, B.J. Maurer, R.N. Kolesnick, Ceramide synthesis and metabolism as a target for cancer therapy, Cancer letters 206(2) (2004) 169-180.
[108] A.H. Futerman, Y.A. Hannun, The complex life of simple sphingolipids, EMBO reports 5(8) (2004) 777-82.
[109] A. Senchenkov, D.A. Litvak, M.C. Cabot, Targeting ceramide metabolism--a strategy for overcoming drug resistance, Journal of the National Cancer Institute 93(5) (2001) 347-57.
[110] Y.-Y. Liu, T.Y. Han, J.Y. Yu, A. Bitterman, A. Le, A.E. Giuliano, M.C. Cabot, Oligonucleotides blocking glucosylceramide synthase expression selectively reverse drug resistance in cancer cells, Journal of lipid research 45(5) (2004) 933-940.
[111] Y.-y. Liu, T.-y. Han, A.E. Giuliano, M.C. CABOT, Ceramide glycosylation potentiates cellular multidrug resistance, The FASEB Journal 15(3) (2001) 719-730.
[112] R.J. Bleicher, M.C. Cabot, Glucosylceramide synthase and apoptosis, Biochimica et biophysica Acta (BBA)-Molecular and Cell Biology of Lipids 1585(2) (2002) 172-178.
[113] A. Abe, N.S. Radin, J.A. Shayman, Induction of glucosylceramide synthase by synthase inhibitors and ceramide, Biochimica et biophysica acta 1299(3) (1996) 333-41.
[114] H. Komori, S. Ichikawa, Y. Hirabayashi, M. Ito, Regulation of UDP-glucose:ceramide glucosyltransferase-1 by ceramide, FEBS letters 475(3) (2000) 247-250.
[115] Y.Y. Liu, J.Y. Yu, D. Yin, G.A. Patwardhan, V. Gupta, Y. Hirabayashi, W.M. Holleran, A.E. Giuliano, S.M. Jazwinski, V. Gouaze-Andersson, D.P. Consoli, M.C. Cabot, A role for ceramide in driving cancer cell resistance to doxorubicin, FASEB journal : official publication of the Federation of American Societies for Experimental Biology 22(7) (2008) 2541-51.
[116] P. Kovacs, M. Pinter, G. Csaba, Effect of glucosphingolipid synthesis inhibitor (PPMP and PDMP) treatment on Tetrahymena pyriformis: data on the evolution of the signaling system, Cell biochemistry and function 18(4) (2000) 269-80.
[117] L. Lee, A. Abe, J.A. Shayman, Improved inhibitors of glucosylceramide synthase, The Journal of biological chemistry 274(21) (1999) 14662-9.
[118] D.A. Litvak, A.J. Bilchik, M.C. Cabot, Modulators of ceramide metabolism sensitize colorectal cancer cells to chemotherapy: a novel treatment strategy, Journal of gastrointestinal surgery 7(1) (2003) 140-148.
[119] B.J. Maurer, L. Melton, C. Billups, M.C. Cabot, C.P. Reynolds, Synergistic cytotoxicity in solid tumor cell lines between N-(4-hydroxyphenyl) retinamide and modulators of ceramide metabolism, Journal of the National Cancer Institute 92(23) (2000) 1897-1909.

[120] J. Xu, X. Zhang, Y. Chen, Y. Huang, P. Wang, Y. Wei, X. Ma, S. Li, Improved Micellar Formulation for Enhanced Delivery for Paclitaxel, Molecular pharmaceutics 14(1) (2017) 31-41.
[121] J. Xu, J. Sun, P. Wang, X. Ma, S. Li, Pendant HDAC inhibitor SAHA derivatised polymer as a novel prodrug micellar carrier for anticancer drugs, Journal of drug targeting 26(5-6) (2018) 448-457.
[122] J. Xu, J. Sun, P. Wang, X. Ma, S. Li, Pendant HDAC inhibitor SAHA derivatised polymer as a novel prodrug micellar carrier for anticancer drugs, Journal of drug targeting (2017) 1-10.
[123] P. Zhang, J. Li, M. Ghazwani, W. Zhao, Y. Huang, X. Zhang, R. Venkataramanan, S. Li, Effective co-delivery of doxorubicin and dasatinib using a PEG-Fmoc nanocarrier for combination cancer chemotherapy, Biomaterials 67 (2015) 104-14.
[124] D. Hartmann, J. Lucks, S. Fuchs, S. Schiffmann, Y. Schreiber, N. Ferreiros, J. Merkens, R. Marschalek, G. Geisslinger, S. Grosch, Long chain ceramides and very long chain ceramides have opposite effects on human breast and colon cancer cell growth, The international journal of biochemistry & cell biology 44(4) (2012) 620-8.
[125] S. Schiffmann, J. Sandner, K. Birod, I. Wobst, C. Angioni, E. Ruckhäberle, M. Kaufmann, H. Ackermann, J. Lötsch, H. Schmidt, Ceramide synthases and ceramide levels are increased in breast cancer tissue, Carcinogenesis 30(5) (2009) 745-752.
[126] S. Panjarian, L. Kozhaya, S. Arayssi, M. Yehia, J. Bielawski, A. Bielawska, J. Usta, Y.A. Hannun, L.M. Obeid, G.S. Dbaibo, De novo N-palmitoylsphingosine synthesis is the major biochemical mechanism of ceramide accumulation following p53 up-regulation, Prostaglandins & other lipid mediators 86(1-4) (2008) 41-8.
[127] M. Eto, J. Bennouna, O.C. Hunter, P.A. Hershberger, T. Kanto, C.S. Johnson, M.T. Lotze, A.A. Amoscato, C16 ceramide accumulates following androgen ablation in LNCaP prostate cancer cells, The Prostate 57(1) (2003) 66-79.
[128] S. Schiffmann, S. Ziebell, J. Sandner, K. Birod, K. Deckmann, D. Hartmann, S. Rode, H. Schmidt, C. Angioni, G. Geisslinger, S. Grosch, Activation of ceramide synthase 6 by celecoxib leads to a selective induction of C16:0-ceramide, Biochemical pharmacology 80(11) (2010) 1632-40.
[129] J. Mesicek, H. Lee, T. Feldman, X. Jiang, A. Skobeleva, E.V. Berdyshev, A. Haimovitz-Friedman, Z. Fuks, R. Kolesnick, Ceramide synthases 2, 5, and 6 confer distinct roles in radiation-induced apoptosis in HeLa cells, Cellular signalling 22(9) (2010) 1300-7.
[130] S. Grösch, S. Schiffmann, G. Geisslinger, Chain length-specific properties of ceramides, Progress in lipid research 51(1) (2012) 50-62.
[131] J.-L. Roh, E.H. Kim, J.Y. Park, J.W. Kim, Inhibition of Glucosylceramide Synthase Sensitizes Head and Neck Cancer to Cisplatin, Molecular cancer therapeutics 14(8) (2015) 1907-1915.
[132] Y. Liu, K.-M. Xie, G.-Q. Yang, X.-M. Bai, Y.-P. Shi, H.-J. Mu, W.-Z. Qiao, B. Zhang, P. Xie, GCS induces multidrug resistance by regulating apoptosis-related genes in K562/AO2 cell line, Cancer chemotherapy and pharmacology 66(3) (2010) 433-439.
[133] B. Henry, C. Moller, M.T. Dimanche-Boitrel, E. Gulbins, K.A. Becker, Targeting the ceramide system in cancer, Cancer letters 332(2) (2013) 286-94.
[134] H.J. Abuhusain, A. Matin, Q. Qiao, H. Shen, N. Kain, B.W. Day, B.W. Stringer, B. Daniels, M.A. Laaksonen, C. Teo, K.L. McDonald, A.S. Don, A metabolic shift favoring sphingosine 1-phosphate at the expense of ceramide controls glioblastoma angiogenesis, The Journal of biological chemistry 288(52) (2013) 37355-64.

[135] A. Gomez-Munoz, P. Gangoiti, L. Arana, A. Ouro, I.G. Rivera, M. Ordonez, M. Trueba, New insights on the role of ceramide 1-phosphate in inflammation, Biochimica et biophysica acta 1831(6) (2013) 1060-6.
[136] M. Kartal Yandim, E. Apohan, Y. Baran, Therapeutic potential of targeting ceramide/glucosylceramide pathway in cancer, Cancer chemotherapy and pharmacology 71(1) (2013) 13-20.
[137] C. Avendaño, J.C. Menéndez, Chapter 8 - Epigenetic Therapy of Cancer, Medicinal Chemistry of Anticancer Drugs (Second Edition), Elsevier, Boston, 2015, pp. 325-358.
[138] S.L. Berger, T. Kouzarides, R. Shiekhattar, A. Shilatifard, An operational definition of epigenetics, Genes & development 23(7) (2009) 781-3.
[139] E.R. Gibney, C.M. Nolan, Epigenetics and gene expression, Heredity 105(1) (2010) 4-13.
[140] T. Kouzarides, Chromatin Modifications and Their Function, Cell 128(4) (2007) 693-705.
[141] M. Grunstein, Histone acetylation in chromatin structure and transcription, Nature 389(6649) (1997) 349-52.
[142] P.D. Gregory, K. Wagner, W. Horz, Histone acetylation and chromatin remodeling, Experimental cell research 265(2) (2001) 195-202.
[143] P. Zhu, E. Martin, J. Mengwasser, P. Schlag, K.P. Janssen, M. Gottlicher, Induction of HDAC2 expression upon loss of APC in colorectal tumorigenesis, Cancer cell 5(5) (2004) 455-63.
[144] K. Halkidou, L. Gaughan, S. Cook, H.Y. Leung, D.E. Neal, C.N. Robson, Upregulation and nuclear recruitment of HDAC1 in hormone refractory prostate cancer, The Prostate 59(2) (2004) 177-89.
[145] J. Song, J.H. Noh, J.H. Lee, J.W. Eun, Y.M. Ahn, S.Y. Kim, S.H. Lee, W.S. Park, N.J. Yoo, J.Y. Lee, S.W. Nam, Increased expression of histone deacetylase 2 is found in human gastric cancer, APMIS : acta pathologica, microbiologica, et immunologica Scandinavica 113(4) (2005) 264-8.
[146] P. Marks, R.A. Rifkind, V.M. Richon, R. Breslow, T. Miller, W.K. Kelly, Histone deacetylases and cancer: causes and therapies, Nature reviews. Cancer 1(3) (2001) 194-202.
[147] R.W. Johnstone, Histone-deacetylase inhibitors: novel drugs for the treatment of cancer, Nature reviews. Drug discovery 1(4) (2002) 287-99.
[148] K.J. Falkenberg, R.W. Johnstone, Histone deacetylases and their inhibitors in cancer, neurological diseases and immune disorders, Nature reviews. Drug discovery 13(9) (2014) 673-91.
[149] P.A. Marks, Discovery and development of SAHA as an anticancer agent, Oncogene 26(9) (2007) 1351-6.
[150] P.A. Marks, R. Breslow, Dimethyl sulfoxide to vorinostat: development of this histone deacetylase inhibitor as an anticancer drug, Nature biotechnology 25(1) (2007) 84-90.
[151] L.M. Butler, D.B. Agus, H.I. Scher, B. Higgins, A. Rose, C. Cordon-Cardo, H.T. Thaler, R.A. Rifkind, P.A. Marks, V.M. Richon, Suberoylanilide hydroxamic acid, an inhibitor of histone deacetylase, suppresses the growth of prostate cancer cells in vitro and in vivo, Cancer research 60(18) (2000) 5165-70.
[152] L.A. Cohen, S. Amin, P.A. Marks, R.A. Rifkind, D. Desai, V.M. Richon, Chemoprevention of carcinogen-induced mammary tumorigenesis by the hybrid polar cytodifferentiation agent, suberanilohydroxamic acid (SAHA), Anticancer research 19(6B) (1999) 4999-5005.

[153] L.Z. He, T. Tolentino, P. Grayson, S. Zhong, R.P. Warrell, Jr., R.A. Rifkind, P.A. Marks, V.M. Richon, P.P. Pandolfi, Histone deacetylase inhibitors induce remission in transgenic models of therapy-resistant acute promyelocytic leukemia, The Journal of clinical investigation 108(9) (2001) 1321-30.
[154] I.Y. Eyupoglu, E. Hahnen, R. Buslei, F.A. Siebzehnrubl, N.E. Savaskan, M. Luders, C. Trankle, W. Wick, M. Weller, R. Fahlbusch, I. Blumcke, Suberoylanilide hydroxamic acid (SAHA) has potent anti-glioma properties in vitro, ex vivo and in vivo, Journal of neurochemistry 93(4) (2005) 992-9.
[155] D. Desai, A. Das, L. Cohen, K. el-Bayoumy, S. Amin, Chemopreventive efficacy of suberoylanilide hydroxamic acid (SAHA) against 4-(methylnitrosamino)-1-(3-pyridyl)-1-butanone (NNK)-induced lung tumorigenesis in female A/J mice, Anticancer research 23(1A) (2003) 499-503.
[156] K.T. Thurn, S. Thomas, A. Moore, P.N. Munster, Rational therapeutic combinations with histone deacetylase inhibitors for the treatment of cancer, Future oncology (London, England) 7(2) (2011) 263-283.
[157] P.N. Munster, D. Marchion, S. Thomas, M. Egorin, S. Minton, G. Springett, J.H. Lee, G. Simon, A. Chiappori, D. Sullivan, A. Daud, Phase I trial of vorinostat and doxorubicin in solid tumours: histone deacetylase 2 expression as a predictive marker, British Journal of Cancer 101(7) (2009) 1044-1050.
[158] D.C. Marchion, E. Bicaku, J.G. Turner, A.I. Daud, D.M. Sullivan, P.N. Munster, Synergistic interaction between histone deacetylase and topoisomerase II inhibitors is mediated through topoisomerase IIbeta, Clinical cancer research : an official journal of the American Association for Cancer Research 11(23) (2005) 8467-75.
[159] D.C. Marchion, E. Bicaku, A.I. Daud, D.M. Sullivan, P.N. Munster, In vivo synergy between topoisomerase II and histone deacetylase inhibitors: predictive correlates, Molecular cancer therapeutics 4(12) (2005) 1993-2000.
[160] N.B. Arnold, N. Arkus, J. Gunn, M. Korc, The Histone Deacetylase Inhibitor Suberoylanilide Hydroxamic Acid Induces Growth Inhibition and Enhances Gemcitabine-Induced Cell Death in Pancreatic Cancer, Clinical Cancer Research 13(1) (2007) 18-26.
[161] S.C. Dowdy, S. Jiang, X.C. Zhou, X. Hou, F. Jin, K.C. Podratz, S.-W. Jiang, Histone deacetylase inhibitors and paclitaxel cause synergistic effects on apoptosis and microtubule stabilization in papillary serous endometrial cancer cells, Molecular Cancer Therapeutics 5(11) (2006) 2767-2776.
[162] H. Rikiishi, F. Shinohara, T. Sato, Y. Sato, M. Suzuki, S. Echigo, Chemosensitization of oral squamous cell carcinoma cells to cisplatin by histone deacetylase inhibitor, suberoylanilide hydroxamic acid, International journal of oncology 30(5) (2007) 1181-8.
[163] M.S. Kim, M. Blake, J.H. Baek, G. Kohlhagen, Y. Pommier, F. Carrier, Inhibition of histone deacetylase increases cytotoxicity to anticancer drugs targeting DNA, Cancer research 63(21) (2003) 7291-300.
[164] R. Nimmanapalli, L. Fuino, C. Stobaugh, V. Richon, K. Bhalla, Cotreatment with the histone deacetylase inhibitor suberoylanilide hydroxamic acid (SAHA) enhances imatinib-induced apoptosis of Bcr-Abl–positive human acute leukemia cells, Blood 101(8) (2003) 3236-3239.
[165] L. Fuino, P. Bali, S. Wittmann, S. Donapaty, F. Guo, H. Yamaguchi, H.G. Wang, P. Atadja, K. Bhalla, Histone deacetylase inhibitor LAQ824 down-regulates Her-2 and sensitizes human

breast cancer cells to trastuzumab, taxotere, gemcitabine, and epothilone B, Molecular cancer therapeutics 2(10) (2003) 971-84.
[166] E.E. Cameron, K.E. Bachman, S. Myohanen, J.G. Herman, S.B. Baylin, Synergy of demethylation and histone deacetylase inhibition in the re-expression of genes silenced in cancer, Nature genetics 21(1) (1999) 103-7.
[167] C.F. Thorn, C. Oshiro, S. Marsh, T. Hernandez-Boussard, H. McLeod, T.E. Klein, R.B. Altman, Doxorubicin pathways: pharmacodynamics and adverse effects, Pharmacogenetics and genomics 21(7) (2011) 440-6.
[168] C.S. Chen, Y.C. Wang, H.C. Yang, P.H. Huang, S.K. Kulp, C.C. Yang, Y.S. Lu, S. Matsuyama, C.Y. Chen, C.S. Chen, Histone deacetylase inhibitors sensitize prostate cancer cells to agents that produce DNA double-strand breaks by targeting Ku70 acetylation, Cancer research 67(11) (2007) 5318-27.
[169] P. Parhi, C. Mohanty, S.K. Sahoo, Nanotechnology-based combinational drug delivery: an emerging approach for cancer therapy, Drug Discovery Today 17(17) (2012) 1044-1052.
[170] J.H. Lee, A. Nan, Combination drug delivery approaches in metastatic breast cancer, Journal of drug delivery 2012 (2012).
[171] E.A. Mohamed, Y. Zhao, M.M. Meshali, C.M. Remsberg, T.M. Borg, A.M. Foda, J.K. Takemoto, C.L. Sayre, S.E. Martinez, N.M. Davies, M.L. Forrest, Vorinostat with sustained exposure and high solubility in poly(ethylene glycol)-b-poly(DL-lactic acid) micelle nanocarriers: characterization and effects on pharmacokinetics in rat serum and urine, Journal of pharmaceutical sciences 101(10) (2012) 3787-98.
[172] S.R. Croy, G.S. Kwon, Polymeric micelles for drug delivery, Current pharmaceutical design 12(36) (2006) 4669-84.
[173] Y.-M. Chung, M. El-Shazly, D.-W. Chuang, T.-L. Hwang, T. Asai, Y. Oshima, M.L. Ashour, Y.-C. Wu, F.-R. Chang, Suberoylanilide Hydroxamic Acid, a Histone Deacetylase Inhibitor, Induces the Production of Anti-inflammatory Cyclodepsipeptides from Beauveria felina, Journal of Natural Products 76(7) (2013) 1260-1266.
[174] Y. Hattori, Y. Nagaoka, M. Kubo, H. Yamasaku, Y. Ishii, H. Okita, H. Nakano, S. Uesato, Y. Maitani, Antitumor effect of liposomal histone deacetylase inhibitor-lipid conjugates in vitro, Chemical & pharmaceutical bulletin 59(11) (2011) 1386-92.
[175] F. Kamangar, G.M. Dores, W.F. Anderson, Patterns of Cancer Incidence, Mortality, and Prevalence Across Five Continents: Defining Priorities to Reduce Cancer Disparities in Different Geographic Regions of the World, Journal of Clinical Oncology 24(14) (2006) 2137-2150.
[176] A.J. Minn, G.P. Gupta, P.M. Siegel, P.D. Bos, W. Shu, D.D. Giri, A. Viale, A.B. Olshen, W.L. Gerald, J. Massagué, Genes that mediate breast cancer metastasis to lung, Nature 436 (2005) 518.
[177] B. Weigelt, J.L. Peterse, L.J. van't Veer, Breast cancer metastasis: markers and models, Nature Reviews Cancer 5 (2005) 591.
[178] W.D. Foulkes, I.E. Smith, J.S. Reis-Filho, Triple-Negative Breast Cancer, New England Journal of Medicine 363(20) (2010) 1938-1948.
[179] R. Dent, M. Trudeau, K.I. Pritchard, W.M. Hanna, H.K. Kahn, C.A. Sawka, L.A. Lickley, E. Rawlinson, P. Sun, S.A. Narod, Triple-Negative Breast Cancer: Clinical Features and Patterns of Recurrence, Clinical Cancer Research 13(15) (2007) 4429-4434.
[180] D.P. Bartel, MicroRNAs: Genomics, Biogenesis, Mechanism, and Function, Cell 116(2) (2004) 281-297.

[181] E. Huntzinger, E. Izaurralde, Gene silencing by microRNAs: contributions of translational repression and mRNA decay, Nature Reviews Genetics 12 (2011) 99.
[182] A.G. Bader, D. Brown, M. Winkler, The Promise of MicroRNA Replacement Therapy, Cancer research 70(18) (2010) 7027-7030.
[183] H. Hermeking, The miR-34 family in cancer and apoptosis, Cell death and differentiation 17 (2009) 193.
[184] C. Liu, K. Kelnar, B. Liu, X. Chen, T. Calhoun-Davis, H. Li, L. Patrawala, H. Yan, C. Jeter, S. Honorio, J.F. Wiggins, A.G. Bader, R. Fagin, D. Brown, D.G. Tang, The microRNA miR-34a inhibits prostate cancer stem cells and metastasis by directly repressing CD44, Nature Medicine 17 (2011) 211.
[185] B.D. Adams, C. Parsons, F.J. Slack, The tumor-suppressive and potential therapeutic functions of miR-34a in epithelial carcinomas, Expert opinion on therapeutic targets 20(6) (2016) 737-753.
[186] A. Bouchie, First microRNA mimic enters clinic, Nature biotechnology 31 (2013) 577.
[187] Q.-X. Chen, W.-P. Wang, S. Zeng, S. Urayama, A.-M. Yu, A general approach to high-yield biosynthesis of chimeric RNAs bearing various types of functional small RNAs for broad applications, Nucleic acids research 43(7) (2015) 3857-3869.
[188] W.P. Wang, P.Y. Ho, Q.X. Chen, B. Addepalli, P.A. Limbach, M.M. Li, W.J. Wu, J.L. Jilek, J.X. Qiu, H.J. Zhang, T. Li, T. Wun, R.D. White, K.S. Lam, A.M. Yu, Bioengineering Novel Chimeric microRNA-34a for Prodrug Cancer Therapy: High-Yield Expression and Purification, and Structural and Functional Characterization, The Journal of pharmacology and experimental therapeutics 354(2) (2015) 131-41.
[189] N. Nayerossadat, T. Maedeh, P.A. Ali, Viral and nonviral delivery systems for gene delivery, Advanced biomedical research 1 (2012) 27-27.
[190] D.W. Pack, A.S. Hoffman, S. Pun, P.S. Stayton, Design and development of polymers for gene delivery, Nature Reviews Drug Discovery 4 (2005) 581.
[191] M.A. Mintzer, E.E. Simanek, Nonviral vectors for gene delivery, Chemical reviews 109(2) (2009) 259-302.
[192] M. Khan, Z.Y. Ong, N. Wiradharma, A.B.E. Attia, Y.-Y. Yang, Advanced Materials for Co-Delivery of Drugs and Genes in Cancer Therapy, Advanced Healthcare Materials 1(4) (2012) 373-392.
[193] F. Kratz, Albumin as a drug carrier: Design of prodrugs, drug conjugates and nanoparticles, Journal of Controlled Release 132(3) (2008) 171-183.
[194] J. Sun, R. Sheng, T. Luo, Z. Wang, H. Li, A.J.J.o.M.C.B. Cao, Synthesis of diblock/statistical cationic glycopolymers with pendant galactose and lysine moieties: Gene delivery application and intracellular behaviors, Journal of Materials Chemistry B 4(27) (2016) 4696-4706.
[195] E. Wagner, M. Zenke, M. Cotten, H. Beug, M.L. Birnstiel, Transferrin-polycation conjugates as carriers for DNA uptake into cells, Proceedings of the National Academy of Sciences 87(9) (1990) 3410-3414.
[196] Y. Zhao, W. Wang, S. Guo, Y. Wang, L. Miao, Y. Xiong, L. Huang, PolyMetformin combines carrier and anticancer activities for in vivo siRNA delivery, Nature Communications 7 (2016) 11822.
[197] L. Huang, S. Li, Liposomal gene delivery: A complex package, Nature biotechnology 15 (1997) 620.

[198] P.H.M. Hoet, B. Nemery, Polyamines in the lung: polyamine uptake and polyamine-linked pathological or toxicological conditions, American Journal of Physiology-Lung Cellular and Molecular Physiology 278(3) (2000) L417-L433.
[199] P.Y. Ho, Z. Duan, N. Batra, J.L. Jilek, M.-J. Tu, J.-X. Qiu, Z. Hu, T. Wun, P.N. Lara, R.W. DeVere White, H.-W. Chen, A.-M. Yu, Bioengineered ncRNAs selectively change cellular miRNome profiles for cancer therapy, Journal of Pharmacology and Experimental Therapeutics (2018).
[200] Q.X. Chen, W.P. Wang, S. Zeng, S. Urayama, A.M. Yu, A general approach to high-yield biosynthesis of chimeric RNAs bearing various types of functional small RNAs for broad applications, Nucleic acids research 43(7) (2015) 3857-69.
[201] J. Xu, J. Sun, P. Wang, X. Ma, S. Li, Pendant HDAC inhibitor SAHA derivatised polymer as a novel prodrug micellar carrier for anticancer drugs, Journal of Drug Targeting 26(5-6) (2018) 448-457.
[202] J. Xu, W. Zhao, J. Sun, Y. Huang, P. Wang, R. Venkataramanan, D. Yang, X. Ma, A. Rana, S. Li, Novel glucosylceramide synthase inhibitor based prodrug copolymer micelles for delivery of anticancer agents, Journal of Controlled Release 288 (2018) 212-226.
[203] Y. Chen, R. Xia, Y. Huang, W. Zhao, J. Li, X. Zhang, P. Wang, R. Venkataramanan, J. Fan, W. Xie, X. Ma, B. Lu, S. Li, An immunostimulatory dual-functional nanocarrier that improves cancer immunochemotherapy, Nature Communications 7 (2016) 13443.
[204] L. Li, L. Yuan, J. Luo, J. Gao, J. Guo, X. Xie, MiR-34a inhibits proliferation and migration of breast cancer through down-regulation of Bcl-2 and SIRT1, Clinical and Experimental Medicine 13(2) (2013) 109-117.
[205] P. Bu, K.-Y. Chen, Joyce H. Chen, L. Wang, J. Walters, Yong J. Shin, Julian P. Goerger, J. Sun, M. Witherspoon, N. Rakhilin, J. Li, H. Yang, J. Milsom, S. Lee, W. Zipfel, Moonsoo M. Jin, Zeynep H. Gümüş, Steven M. Lipkin, X. Shen, A microRNA miR-34a-Regulated Bimodal Switch Targets Notch in Colon Cancer Stem Cells, Cell Stem Cell 12(5) (2013) 602-615.
[206] A.S. Graham, R.C. Hatton, Creatine: A Review of Efficacy and Safety, Journal of the American Pharmaceutical Association 39(6) (1999) 803-810.
[207] R. Cooper, F. Naclerio, J. Allgrove, A. Jimenez, Creatine supplementation with specific view to exercise/sports performance: an update, Journal of the International Society of Sports Nutrition 9(1) (2012) 33-33.
[208] M. Wyss, R. Kaddurah-Daouk, Creatine and Creatinine Metabolism, Physiological Reviews 80(3) (2000) 1107-1213.
[209] E. Van Rooij, S. Kauppinen, Development of microRNA therapeutics is coming of age, EMBO molecular medicine 6(7) (2014) 851-864.
[210] J. Bramsen, J. Kjems, Development of Therapeutic-Grade Small Interfering RNAs by Chemical Engineering, Frontiers in Genetics 3(154) (2012).
[211] L. Kang, Z. Gao, W. Huang, M. Jin, Q. Wang, Nanocarrier-mediated co-delivery of chemotherapeutic drugs and gene agents for cancer treatment, Acta Pharmaceutica Sinica B 5(3) (2015) 169-175.
[212] B.J. Rackstraw, A.L. Martin, S. Stolnik, C.J. Roberts, M.C. Garnett, M.C. Davies, S.J.B. Tendler, Microscopic Investigations into PEG−Cationic Polymer-Induced DNA Condensation, Langmuir 17(11) (2001) 3185-3193.
[213] C.J. Bishop, K.L. Kozielski, J.J. Green, Exploring the role of polymer structure on intracellular nucleic acid delivery via polymeric nanoparticles, Journal of controlled release : official journal of the Controlled Release Society 219 (2015) 488-499.

[214] M.M. Amiji, Polymeric gene delivery : principles and applications, CRC2005.
[215] M.S. Draz, B.A. Fang, P. Zhang, Z. Hu, S. Gu, K.C. Weng, J.W. Gray, F.F. Chen, Nanoparticle-mediated systemic delivery of siRNA for treatment of cancers and viral infections, Theranostics 4(9) (2014) 872-892.
[216] Q. Mu, G. Jiang, L. Chen, H. Zhou, D. Fourches, A. Tropsha, B. Yan, Chemical Basis of Interactions Between Engineered Nanoparticles and Biological Systems, Chemical Reviews 114(15) (2014) 7740-7781.
[217] C.F. Matta, N. Castillo, R.J. Boyd, Extended Weak Bonding Interactions in DNA: π-Stacking (Base−Base), Base−Backbone, and Backbone−Backbone Interactions, The Journal of Physical Chemistry B 110(1) (2006) 563-578.
[218] P.A. Wender, W.C. Galliher, E.A. Goun, L.R. Jones, T.H. Pillow, The design of guanidinium-rich transporters and their internalization mechanisms, Advanced Drug Delivery Reviews 60(4-5) (2008) 452-72.
[219] E.G. Stanzl, B.M. Trantow, J.R. Vargas, P.A. Wender, Fifteen years of cell-penetrating, guanidinium-rich molecular transporters: basic science, research tools, and clinical applications, Accounts of chemical research 46(12) (2013) 2944-54.
[220] K. Patne, R. Rakesh, V. Arya, U.B. Chanana, R. Sethy, P.B. Swer, R. Muthuswami, BRG1 and SMARCAL1 transcriptionally co-regulate DROSHA, DGCR8 and DICER in response to doxorubicin-induced DNA damage, Biochimica et Biophysica Acta (BBA) - Gene Regulatory Mechanisms 1860(9) (2017) 936-951.
[221] Y. Ma, L. Aymeric, C. Locher, S.R. Mattarollo, N.F. Delahaye, P. Pereira, L. Boucontet, L. Apetoh, F. Ghiringhelli, N. Casares, J.J. Lasarte, G. Matsuzaki, K. Ikuta, B. Ryffel, K. Benlagha, A. Tesnière, N. Ibrahim, J. Déchanet-Merville, N. Chaput, M.J. Smyth, G. Kroemer, L. Zitvogel, Contribution of IL-17–producing γδ T cells to the efficacy of anticancer chemotherapy, The Journal of Experimental Medicine 208(3) (2011) 491-503.
[222] G.L. Zwicke, G.A. Mansoori, C.J. Jeffery, Utilizing the folate receptor for active targeting of cancer nanotherapeutics, Nano reviews 3 (2012) 10.3402/nano.v3i0.18496.
[223] T.R. Daniels, E. Bernabeu, J.A. Rodríguez, S. Patel, M. Kozman, D.A. Chiappetta, E. Holler, J.Y. Ljubimova, G. Helguera, M.L. Penichet, The transferrin receptor and the targeted delivery of therapeutic agents against cancer, Biochimica et biophysica acta 1820(3) (2012) 291-317.
[224] F. Wang, Y. Li, Y. Shen, A. Wang, S. Wang, T. Xie, The functions and applications of RGD in tumor therapy and tissue engineering, International journal of molecular sciences 14(7) (2013) 13447-13462.
[225] H. Cabral, Y. Matsumoto, K. Mizuno, Q. Chen, M. Murakami, M. Kimura, Y. Terada, M.R. Kano, K. Miyazono, M. Uesaka, N. Nishiyama, K. Kataoka, Accumulation of sub-100 nm polymeric micelles in poorly permeable tumours depends on size, Nature Nanotechnology 6 (2011) 815.
[226] R.A. Morgan, Human tumor xenografts: the good, the bad, and the ugly, Molecular therapy : the journal of the American Society of Gene Therapy 20(5) (2012) 882-884.
[227] A. Richmond, Y. Su, Mouse xenograft models vs GEM models for human cancer therapeutics, Disease models & mechanisms 1(2-3) (2008) 78-82.